SALT NANOPARTICLES AS CANCER THERAPEUTICS

by

SHUYUE ZHAN

(Under the Direction of Jin Xie)

ABSTRACT

Alkali halide nanoparticles, derived from elements in Group IA and Group VIIA of the Periodic Table, have garnered interest for their potential applications in various biomedical fields. Particularly, sodium chloride nanoparticles (SCNPs) challenge the conventional belief that salt nanoparticles exhibit identical behavior to their constituent salts. The main project is based on the hypothesis that SCNPs can disrupt the osmotic balance across the plasma membrane of cancer cells. Ion homeostasis is essential for maintaining the integrity of the plasma membrane and sustaining normal cell functions. Disruption of homeostasis could disrupt the potential balance and interrupt essential cellular processes. Instead of using organic ionophores, we are exploring SCNPs as a new strategy to transport ions across the plasma membrane and ultimately cause cancer cell death. While the plasma membrane is not permeable to ions, we hypothesize that SCNPs can enter the cell by endocytosis and degrade inside the cell, releasing large quantities of ions into cancer cells therein. Our extensive *in vitro* studies strongly support this hypothesis. Moreover, our results showed that SCNPs are more toxic to cancer cells than to normal cells. This is because cancer cells have higher intracellular sodium levels, making them more susceptible to SCNPs-induced ion disruption. We tested SCNPs *in vivo* in tumor models established with MB49 and other bladder cancer cell lines. Our data confirmed that SCNPs can

effectively suppress tumor growth without causing additional systemic toxicity. In addition, we observed that cancer cells exposed to SCNPs released immunogenic cell death (ICD) signals, including HMGB1, ATP, and CRT. Preliminary studies suggest that combination therapy with SCNPs and anti-PD-1 antibodies can induce an anti-cancer immune response that contributes to inhibited tumor growth and metastasis. We have also observed evidence supporting the potential use of SCNPs as radiosensitizers. Taken together, SCNPs represent a novel and promising cancer therapeutic strategy.

INDEX WORDS: salt nanoparticles, sodium chloride nanoparticles, immunogenic cell death, radiosensitizers, cancer therapeutics

SALT NANOPARTICLES AS CANCER THERAPEUTICS

by

SHUYUE ZHAN

BS, Nanjing Normal University, China, 2018

A Dissertation Submitted to the Graduate Faculty of The University of Georgia in Partial Fulfillment of the Requirements for the Degree

DOCTOR OF PHILOSOPHY

ATHENS, GEORGIA

2023

SALT NANOPARTICLES AS CANCER THERAPEUTICS

by

SHUYUE ZHAN

Major Professor:	Jin Xie
Committee:	Leidong Mao
	Jeffrey L Urbauer

Electronic Version Approved:

Ron Walcott
Vice Provost for Graduate Education and Dean of the Graduate School
The University of Georgia
May 2023

DEDICATION

“You’re on your own, Kid.”

ACKNOWLEDGEMENTS

I am filled with gratitude and emotion as I reflect on the completion of my Ph.D. thesis. Without the unwavering support from those who believed in me, I would not have made it this far.

My parents, Fangliang Zhan, and Yehong Wang, and my little sister, Shuyu Zhan, have been the light that guided me through the darkest times. Their unconditional love, encouragement, and faith in me have been the fuel that kept me going, even when the path seemed insurmountable. They are my pillars of strength; words cannot convey the profound gratitude hold in my heart.

My supervisor, Dr. Jin Xie, has been the wind that lifted me to new heights. His wisdom and expertise were invaluable to me in my pursuit of knowledge, and his dedication and passion for the subjects were a source of inspiration and motivation for me as a research scientist. As well as the professors I have met in my life, have never despised me due to my ignorance. I am eternally thankful for their guidance throughout this journey.

My husband, Ruijie Jiang, has been the anchor that provides me steadiness in times of uncertainty and self-doubt. His optimism rescued me from the dark, bottomless, yarning abyss and inspired me to be the best that I can be. I love you.

My loved ones, their name was engraved in the bottom of my heart. Thanks for being there and sharing happiness and sadness with me.

Myself. Thanks for standing by me every step of the way, never giving up on me even when I fell down, and embracing me with forgiveness. Life could be harder after graduation, but I know I can face it.

TABLE OF CONTENTS

Page

LIST OF TABLES

Page

LIST OF FIGURES

Page

CHAPTER 1

ALKALI HALIDE NANOPARTICLES AND THEIR BIO-APPLICATIONS

Introduction

The alkali halides are the family of inorganic compounds containing elements from Group IA and Group VIIA of the Periodic Table of Elements. Five alkali metals and four halogens form a total of 20 compounds[1]. Due to their simplicity and optical transparency, these bulk crystal compounds have a variety of applications as optical windows, color-centered lasers, and scintillators. Therefore, many studies have focused on the development of growth methods for the improvement and investigation of the optical and structural quality of alkali halide crystals. With the evolution of nanotechnology, nano-sized alkali halide materials have been synthesized, expanding their applications to more areas, especially in biomedical fields [2, 3]. Here, I summarized several alkali halide nanoparticles that have been successfully synthesized by our group and their potential applications.

Sodium-based nanoparticles

Electrolytes, including sodium, potassium, and chloride, perform essential biological functions in the human body. These electrolytes, which are primarily absorbed through the digestive tract and excreted through sweat and urine[4], contribute to cell volume control, membrane potential regulation, and osmotic pressure balance. Sodium, the most abundant cation in the extracellular fluid (up to 146 mM), plays a critical role in determining the osmotic pressure

gradient between cells and their environment[5]. However, ion transport across cell membranes is tightly regulated by specific ion channels and transporters, such as sodium-potassium adenosine triphosphatase (Na^+-K^+-ATPase), which maintains high extracellular sodium and intracellular potassium levels[6]. The asymmetric ion distribution and selective ionic permeability generate a membrane potential (-40 to -80 mV) that drives ion mobility[7]. A significant disruption of ion homeostasis could affect osmolarity, plasma membrane potential, and essential cellular processes, leading to cell death.

Novel sodium chloride nanoparticles (SCNPs) were synthesized by a two-phase microemulsion technique. Sodium acetate as the sodium precursor was first dissolved in ethanol, followed by the addition of hexane and the surfactant oleylamine. Acetyl chloride is then added dropwise to the mixture, and after washing with isopropanol and drying by rotary evaporation, SCNPs are obtained. Since SCNPs are sensitive to humidity, they must be stored in a low-humidity environment, such as a desiccator. To prevent rapid degradation of SCNPs after redispersion in a medium or buffer, a layer of PEGylated phospholipid, DSPE-PEG2000 amine, is applied to the surface of the nanoparticles to prolong their functional lifetime.

In vitro studies have demonstrated that SCNPs can disrupt the osmotic balance across the plasma membrane of cancer cells[8]. Maintaining ion homeostasis is critical for maintaining plasma membrane integrity and normal cellular functions. Disruption of this balance can interfere with essential cellular processes. SCNPs, as an alternative to organic ionophores, can transport ions across the plasma membrane by entering cells via endocytosis and degrading intracellularly, releasing large amounts of ions into cancer cells.

We also found that cancer cells exposed to SCNPs release immunogenic cell death (ICD) signals, including HMGB1, ATP, and CRT. Preliminary studies suggest that combining SCNPs

with anti-PD-1 antibodies may induce an anti-cancer immune response, resulting in inhibited tumor growth and metastasis. We will discuss this in detail in chapter 2.

Potassium-based nanoparticles

Unlike sodium, potassium is the primary intracellular cation with concentrations of 140-150 mM. While having minimal effect on osmotic pressure, potassium primarily regulates cell membrane potential. The four major classes of potassium channels-voltage-gated, calcium-activated, inward rectifier, and two-pore domain potassium channels-along with the Na^+/K^+ pump, provide specific potassium permeability between the intracellular and extracellular spaces. This results in an asymmetric distribution and electrochemical gradient of potassium ions[9]. Under resting conditions, potassium mainly moves across the membrane and out of the cell, creating a negative membrane potential or resting potential. In excitable neurons, potassium is involved in controlling nerve impulses or action potentials, which generate electrical signals. An imbalance of potassium and deregulation of potassium channels can significantly affect neuronal and other biological processes, including cell proliferation, migration, and apoptosis, thereby affecting tumor progression[10].

Potassium-based nanoparticles have been explored, including potassium chloride nanoparticles, which were synthesized similarly to sodium chloride using potassium acetate and acetyl chloride as precursors in a mixed solvent of hexane and ethanol at room temperature. Another example is potassium iodide nanoparticles prepared by adding potassium oleate to 1-octadecene and mixing at 290 ℃ until completely dissolved. Oleylamine is added as a mild reducing agent to convert I_2 to I^-, followed by the addition of iodine and stirring overnight at

room temperature. KI nanoparticles were washed three times with ethanol and dried in an oven[11].

A common property of electrolyte nanoparticles is their rapid degradation in aqueous solutions due to their high water solubility. To extend their half-life, KI nanoparticles were coated with a layer of biocompatible and biodegradable poly(maleic anhydride-alt-1-octadecene) (PMAO). The hydrophobic alkyl chain of PMAO intercalates with the main chains of the surfactant oleate/oleylamine, and the anhydride rings exposed to the outside are opened under basic conditions and linked by the amino group of the PEG-amine crosslinker. The PMAO coating imparts a negatively charged surface to the KI nanoparticles and enhances their electrostatic stabilization[12].

KI nanoparticles have shown potential as radiosensitizers to improve radiotherapy outcomes. Radiotherapy, an important component of cancer treatment, is administered to more than half of all cancer patients[13]. High-energy radiation, such as X-rays and γ-rays, is delivered to the tumor site, causing DNA damage and directly killing cancer cells. However, some cancer cells can evade destruction due to radioresistance, and higher doses of radiation can damage normal cells[14, 15]. Balancing tumor eradication with tissue protection is challenging but critical. Radiosensitizers, which render tumor cells more susceptible to radiation at safer doses, have been developed to address this issue. Materials containing high-Z elements such as gold, bismuth, and hafnium have been evaluated for enhanced X-ray absorption and free radical generation[16]. However, clinical translation is hampered by their high cost and a poor clearance from the body. Another option is iodine-based materials, which are nearly colorless, non-toxic, and less expensive[17]. Iodinated contrast agents used in medical imaging have been proven to

increase radiation-induced cancer cell death[18]. KI nanoparticles are designed to address iodine delivery and targeting issues.

Studies have reported that the Na^+/I^- symporter (NIS), which mediates iodine uptake for hormone synthesis[19], is expressed in approximately 70% of human invasive breast cancers, including triple-negative cases[20]. Iodide ions are slowly released from KI nanoparticles at the tumor site and actively transported into the breast cancer cell by the NIS symporter. Inside the cancer cells, I^- promotes radical generation under radiation irradiation, leading to lipid peroxidation and extensive DNA damage, further improving the radiotherapy for breast cancer.

Cesium-based nanoparticles

X-rays (wavelengths from 0.01 to 10 nm) and gamma rays (γ rays, wavelengths shorter than 0.01 nm) are both types of high-energy ionizing radiation capable of penetrating barriers and interacting with electrons within atoms of dense materials. This allows non-destructive information retrieval from the object. Accurate identification, detection, and quantification of X-rays and γ-rays ensure data accuracy. These rays can be detected directly by ionizing radiation detectors or indirectly by scintillators and photodetectors. Scintillators convert high-energy radiation into ultraviolet-visible (UV-Vis) light, which is then detected by photodetectors and converted into electrical signals. Key scintillator parameters include light yield (photons/MeV), which affects efficiency, sensitivity, and energy resolution[21], and effective atomic number (Zeff), which is related to radiation absorption efficiency or attenuation coefficient[22]. High-Z scintillators with high light yield are desirable. Thallium-doped cesium iodide (CsI:Tl), with the constituent elements Cs (Z=55) and I (Z=53), has a significantly higher light yield than most

inorganic scintillators[23]. Currently, commercially available X-ray and γ-ray scintillators are dominated by CsI:Tl and NaI:Tl[22, 24].

Nanotechnology is expanding scintillator applications, particularly in medicine. Nanomaterial-based scintillators possess unique photophysical properties, generating multiple electron-positron pairs from a single photon and improving the efficiency of the photoelectric effect[25]. CsI nanoparticles were synthesized by a simple redox reaction. CsI nanoparticles were synthesized by a simple redox reaction. Cesium carbonate and oleic acid were dissolved in 1-octadecene and heated to 150 ℃, then oleylamine, 1,2-hexadecanediol, and NaI were added to the mixture, followed by the addition of I_2[26].

Alkali metal halide scintillators, including CsI(Na) nanoparticles, are generally unstable and fragile in humid environments, requiring desiccated storage conditions. To prevent rapid degradation, a layer of MgO is added to the nanoparticle surface via seed-mediated growth. Further coating with DSPE-PEG-COOH and DSPE-PEG-folate (3:1 molar ratio) via thin film hydration adds specific targeting functional groups, resulting in CIS@M-F nanoparticles.

When conjugated to a photosensitizer (PS), scintillators function as radiation converters in photodynamic cancer therapy. Traditional photodynamic therapy (PDT) uses light to activate PS in oxygen-rich tissue, generating cytotoxic reactive oxygen species (ROS). However, the limited tissue penetration of light (< 1 cm) limits the use of PDT in deep-seated tumors. X-PDT, or radiodynamic therapy (RDT), employs X-ray excitation sources for deeper tissue penetration. Scintillators convert ionizing radiation into light and emit luminescence upon X-ray activation to trigger PS, such as 5-aminolevulinic acid (5-ALA), which generates singlet oxygen and kills cancer cells[27, 28]. 5-ALA is a clinically approved photosensitizer that converts to protoporphyrin IX (PpIX) and accumulates in cancer cell mitochondria. The emission of

CIS@M-F matches the absorption of PpIX, allowing CIS@M-F to induce X-ray luminescence for PpIX activation, causing mitochondrial damage and enhancing RT-induced DNA damage through high-Z effects. CIS@M-F administration with 5-ALA combines the strengths of PDT and RT, establishing a promising X-PDT option.

Lithium-based nanoparticles

Lithium is the first alkali metal in the group IA of the periodic table of elements with an atomic number of 3. The lithium salt is commonly used as a mood stabilizer for the treatment of psychiatric disorders such as bipolar and depressive disorders[29]. Several hypotheses have been proposed to elucidate the pharmacological mechanisms of lithium. The first mechanism discovered is that lithium ions inhibit inositol monophosphate (IMP), which plays a role in inositol phosphate metabolism, leading to inositol and phosphatidylinositol depletion. Subsequently, direct and indirect inhibition of glycogen synthase kinase-3 (GSK-3) by lithium gained support and gradually became the dominant explanation. In addition, other signaling pathways, including cAMP regulation, NMDA receptor activation, and calcium absorption blockade, have been investigated[30]. In particular, active GSK3 strongly promotes inflammation, and the anti-inflammatory effects of lithium result from GSK3 inhibition[31]. The association between lithium and inflammation is mediated through GSK-3β[32]. One possibility is that lithium inhibits GSK-3β by downregulating transcription factors such as nuclear factor (NF)-κB or signal transducer and activator of transcription (STAT), and subsequently decreases the expression of inflammatory mediators and enzymes, including cyclooxygenase-2 (COX-2), nitric oxide synthase (NOS), interleukin-1β (IL-1β), and tumor necrosis factor-α (TNF-α)[33].

Osteoarthritis (OA) is a progressive, chronic degenerative joint disease with increased risk due to factors such as aging, obesity, joint injury, and articular cartilage degradation[34]. Although the basic biological mechanism of OA remains unclear, inflammation, including active synovitis and systemic inflammation, influences the pathogenesis of OA[35]. Currently, there is no cure for OA, making the development of novel treatments crucial to slowing disease progression. Lithium salts, with their anti-inflammatory properties, have been shown to counteract cartilage degradation in OA by inhibiting NF-κB, p38, and STAT3 pathways[36]. However, the effective concentration required (5-10 mM) exceeds the serum toxicity threshold of lithium (1.5 mM), and lithium administered intra-articularly is rapidly cleared from the joint space[37].

A lithium-based delivery nanoplatforms was developed for controlled lithium release, resulting in effective OA therapy. LiF was synthesized by a co-precipitation method and then coated with a silica layer to delay the rapid degradation of the nanoparticles in water[38]. Briefly, lithium nitrate was dissolved in a mixed solvent of ethylene glycol (EG)/polyethylene glycol (PEG, Mw = 300) at a ratio of 1:1, followed by dropwise addition of ammonium fluoride in EG solution under gentle magnetic stirring at room temperature. Then, 100 nm cubic LiF nanoparticles were obtained. Li_2CO_3 and Li_3PhO_4 nanoparticles have also been developed to expand the lithium-based nanoparticle options. For Li_2CO_3, ammonium carbonate of 0.04M was dissolved in 20 mL EG and lithium hydroxide of 0.08M was dissolved in the same volume of D.I water, respectively. The lithium hydroxide solution was added to the ammonium carbonate solution with strong stirring at room temperature for 24 hours. The products were washed with ethanol and centrifuged three times, dried at 60℃ overnight. For Li_3PhO_4, cetyltrimethylammonium bromide (CTAB) as a surfactant was dissolved in 20 mL DI water,

followed by the addition of lithium hydroxide with phosphoric acid in 20 mL DI water. The reaction was carried out under vigorous stirring at room temperature. Li_3PhO_4 was obtained after 12 h.

$LiF@SiO_2$ nanoparticles (SLFNPs) have been shown to inhibit proinflammatory cytokine-induced catabolism and protect the cartilage matrix from degradation. Compared to LiCl salt, SLFNPs significantly reduced the expression of OA-associated catabolic biomarkers such as MMP-13, MMP-3, IL-6, COX-2, ADAMTS-5, and iNOS in chondrocytes due to the controlled release of lithium by the silica coating. When combined with hyaluronic acid (HA), which prolongs the retention time of the nanoparticles, SLFNPs exhibited enhanced anti-catabolic effects and cartilage protection, reducing lesion areas in a rat OA model. This approach with LiF nanoparticles explores a new direction in OA therapy, taking advantage of nanotechnology[39].

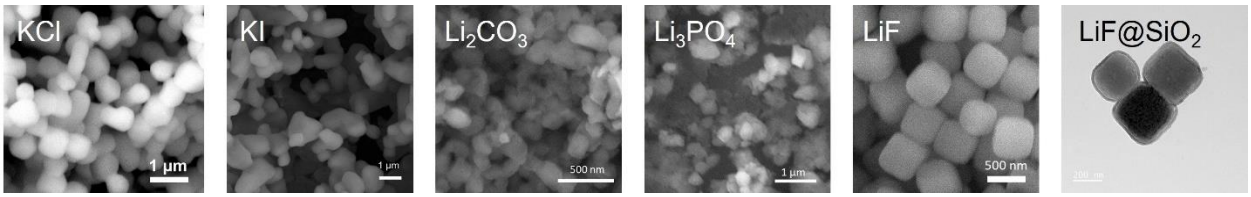

Figure 1.1. Representative SEM images of KCl, KI, Li2CO3, Li3PO4, LiF nanoparticles, TEM image of LiF@SiO2 nanoparticles.

Summary

With the advent of nanotechnology, nano-sized alkali halide materials have been synthesized using a variety of techniques and have been found to have significant potential applications in various fields, particularly in the biomedical field. Sodium chloride nanoparticles have been found to disrupt the osmotic balance in cancer cells and release immunogenic cell death signals. Potassium-based nanoparticles have been used as radiosensitizers in radiotherapy,

while cesium-based nanoparticles have shown promise as X-ray and γ-ray scintillators. Lithium-based nanoparticles have been developed for the treatment of osteoarthritis, taking advantage of the metal's anti-inflammatory properties. A common challenge for these nanoparticles is their rapid degradation in aqueous solutions, necessitating surface coatings or modifications to improve stability and functionality. Nanotechnology has expanded the potential applications of alkali halide nanoparticles with increased efficiency, improved targeting, and controlled release of therapeutic agents, offering advantages in areas such as cancer treatment. In the following, we will focus on sodium chloride nanoparticles and explore their potential as cancer therapeutics.

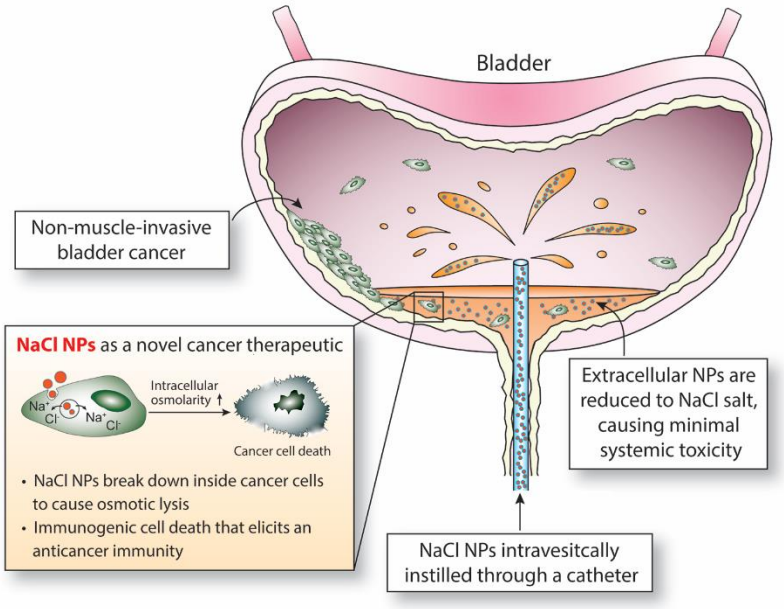

Figure 1.2. Proposed working mechanism of SCNPs in orthotopic tumor model.

CHAPTER 2

SODIUM CHLORIDE NANOPARTICLES AS URINARY BLADDER CANCER THERAPEUTICS

Introduction

Urinary bladder cancer ranked as the sixth most prevalent cancer type and the tenth leading cause of cancer-related death in the United States in 2020, according to the American Cancer Society's annual statistics[40]. Approximately 81,400 new cases of bladder cancer and 17,980 deaths are expected, with men disproportionately affected as it is the fourth most common cancer among them. Urothelial carcinoma, which originates primarily from the urothelium of the bladder, is the most common form of bladder cancer. Bladder cancer is broadly classified into non-muscle invasive bladder cancer (NMIBC) and muscle-invasive bladder cancer (MIBC) based on tumor invasion of the muscularis propria. Approximately 75% of newly diagnosed cases are NMIBC, while the remaining 25% are MIBC or metastatic disease, the latter being the most severe scenario[41]. Surgical transurethral resection of bladder tumors (TURBT) is the first step in standard bladder cancer treatment, followed by adjuvant intravesical chemotherapy or immunotherapy to eliminate existing or residual tumors[42]. Local-regional therapy is particularly effective for bladder cancer because it targets superficial cases and maximizes therapeutic exposure, resulting in improved anticancer effects[43]. Sodium chloride nanoparticles can be designed as a localized bladder cancer treatment to minimize systemic toxicity, thereby reducing patient discomfort and suffering[44].

The novelty and uniqueness of sodium chloride nanoparticles was presented in Chapter 1. In short, ion homeostasis is critical for maintaining cellular integrity and ensuring proper cell function[45]. The balance between ion influx and efflux is tightly regulated by ion channels and transporters. While several strategies have been developed to target ion homeostasis as potential anticancer agents[46], including channel blockers and ionophores, the sodium chloride nanoparticle strategy may offer additional advantages in the context of cancer therapy.

Immunogenic cell death (ICD) is a unique form of regulated cell death that promotes an anti-tumor immune response and contributes to the success of several cancer therapies such as cisplatin and mitoxantrone (MTX)[47]. Characterized by the release of endogenous immunostimulatory molecules known as Damage Associated Molecular Patterns (DAMPs), ICD stimulates the immune system by facilitating the recognition of dying tumor cells. Key DAMPs involved in ICD include calreticulin (CRT), adenosine triphosphate (ATP), and high mobility group box 1 (HMGB-1)[48]. These molecules are recognized by pattern recognition receptors (PRRs) on antigen presenting cells (APCs) such as dendritic cells (DCs). Interaction with their respective PRRs, including CD91 and SR-A for CRT, RAGE and TLR4 for HMGB-1, and P2RX7/P2RY2 for ATP, promotes DC migration, maturation, and antigen cross-presentation to T cells[14]. This process ultimately leads to the generation of T cell-mediated adaptive immunity against tumors. An ideal ICD inducer should efficiently induce apoptosis or necrosis, resulting in the expression of multiple DAMPs. In recent years, researchers have explored nanoparticle platforms to stimulate ICD against tumor growth for cancer immunotherapy, showing promising results in enhancing the efficacy of conventional treatments[49]. By harnessing the potential of ICD, novel therapies can improve cancer outcomes and pave the way for more effective and

targeted treatments. **Recently, we found that sodium chloride nanoparticles can not only kill cancer cells but also induce ICD, rendering it a competitive cancer therapeutic.**

In this study, we presented a novel approach using phospholipid-coated sodium chloride nanoparticles (PSCNPs) as a potential treatment for bladder cancer. We synthesized and characterized SCNPs of various sizes and coated them with a layer of DSPE-PEG(2000) Amine, resulting in PSCNPs that can be stably dispersed in aqueous solutions. We investigated the degradation, endocytosis, and effects of PSCNPs on cellular ion homeostasis, as well as their effects on cell viability and cell death mechanisms. Furthermore, we investigated the ability of PSCNPs to induce ICD and their impact on the tumor microenvironment (TME) and major organs. Finally, we evaluated the therapeutic efficacy of PSCNPs in subcutaneous tumor models, both as a single treatment and in combination with αPD1. Our results suggest that PSCNPs hold promise as a novel and effective treatment for bladder cancer, with the potential to boost immunity and transform the tumor microenvironment without causing systemic toxicity.

Synthesis and characterization of SCNPs

We synthesized SCNPs of different sizes using a modified recipe. Briefly, we dissolved sodium acetate and oleylamine in ethanol and dropwise added acetyl chloride in hexane into the solution. This resulted in the formation of nanoparticles at room temperature (**Figure 2.1 a**). The product was collected by centrifugation and redispersed in hexane.

As determined by transmission electron microscopy (TEM) (**Figure 2.1 b**), the obtained nanoparticles were cube-shaped. In a typical reaction, 250 nm nanoparticles (246 ± 49 nm) were synthesized (**Figure 2.1 h**). Nanoparticles of other sizes can be synthesized by varying reaction conditions (**Figure S2.1**). Energy dispersive X-ray spectroscopy (EDS) confirmed the existence

of sodium and chloride within the nanoparticles, with a molar ratio of the two elements being close to 1:1 (**Figure 2.1 e**). Compared with earlier synthesis methods, molybdenum which may cause cytotoxicity has been eliminated. X-ray powder diffraction (XRD) also confirmed that the particles are nanocrystals made of NaCl (**Figure 2.1 i**).

Next, we coated the nanoparticles with a layer of DSPE-PEG(2000)-Amine using the thin-film hydration method. Fourier-transform infrared (FTIR) spectroscopy found a strong peak at 1100 cm^{-1} (**Figure 2.1 l**) with PSCNPs, which is attributed to the C-O-C stretching arising from the PEG chain, confirming the successful coating. The resulting phospholipid coated SCNPs (PSCNPs) can be stably dispersed in aeneous solutions. The morphology of the NaCl core remained almost unchanged over the surface modification (**Figure 2.1 f**). Dynamic light scattering (DLS) indicated that PSCNPs have a hydrodynamic size of 298 nm (**Figure 2.1 j**); the increased size relative to SCNPs was attributed to the phospholipid coating. The nanoparticles bear a slightly positive surface charge (20 mV, **Figure 2.1 k**), which is attributed to the surface amine groups.

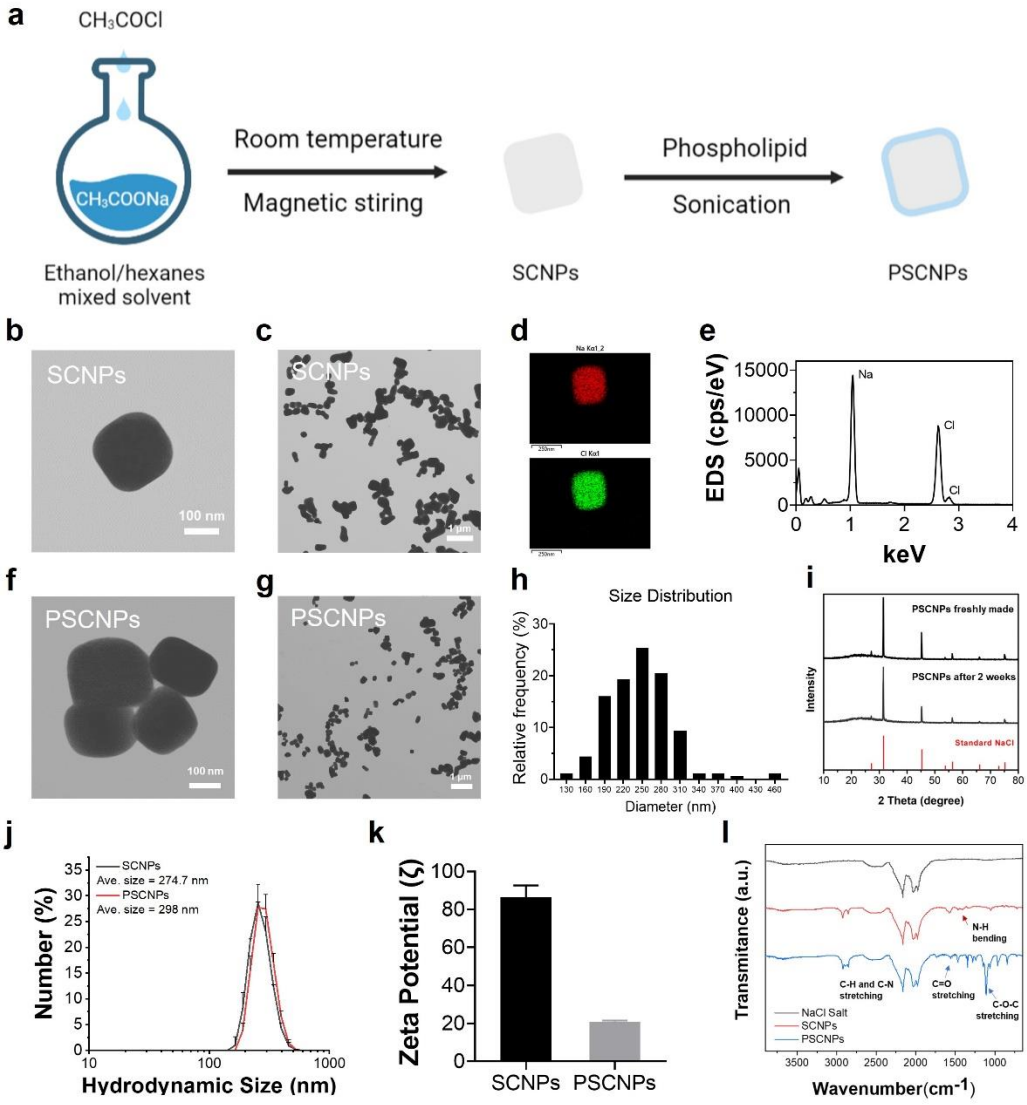

Figure 2.1. Nanoparticles synthesis and characterizations. a) Synthesis flow scheme. b) Representative TEM image of SCNPs, single particle. c) TEM image of SCNPs, broad view. d) Elemental mapping of SCNPs. e) EDS spectra of SCNPs. f) TEM image of PSCNPs, single particle. g) TEM image of PSCNPs, broad view. h) Size distribution of PSCNPs, count and statistics from TEM images by image J. i) XRD spectra of PSCNPs, NaCl salt reference. j) Size distribution analysis by dynamic light scattering (DLS). The hydrodynamic size of SCNPs in isopropanol was 274.7 nm. After coating, it was slightly increased to 298 nm. k) Surface charge of SCNPs and PSCNPs in D.I. water. l) FT-IR spectra of NaCl salt, as-synthesized SCNPs, and PSCNPs.

Impact of nanoparticles on cellular ion homeostasis

We incubated PSCNPs in water and took samples at different times for TEM analysis. Consistent with the previous study, we found that the NaCl cores slowly degraded in water, and almost completely dissolved after 24 hours (**Figure 2.2 a**). This result is in agreement with sodium release, which showed that a half-life around 5-6 h. Note that PSCNPs showed a comparable release rate at both neutral and acidic pH (**Figure 2.2 b**).

We then studied the interaction between PSCNPs and cells. We studied this with dye-labeled PSCNPs and BBN963 cells, a murine bladder cancer cell line. Flow cytometry confirmed the uptake of PSCNPs by the BBN963 cells (**Figure 2.2 c**). The uptake was inhibited by sodium azide, a broad-spectrum metabolic inhibitor, indicating that the nanoparticle entry was mediated by energy-depended endocytosis. Co-incubation with chlorpromazine and dynasore also suppressed cell uptake, whereas nystatin showed marginal inhibitive effects.

Next, we investigated the impact of PSCNPs on intracellular ion homeostasis. This was examined with SBFI-AM and MQAE, two membrane permeable dyes that are selectively responsive to intracellular sodium and chloride, respectively. Note that while the intensity of SBFI-AM increases at a high sodium concentration, the signal of MQAE is negatively correlated with the chloride level. Both SBFI-AM and MQAE results indicate that there is a time-dependent increase of sodium (**Figure 2.2 d**) and chloride levels (**Figure 2.2 e**) upon cell incubation with SCNPs. Meanwhile, dynasore was able to inhibit sodium and chloride level increasement. These results suggest that PSCNPs enter cells through the dynamin-dependent endocytosis pathway, and release sodium and chloride therein, leading to increased concentrations of the two ions.

Intriguingly, we found that intracellular calcium also increased over incubation with PSCNPs (**Figure 2.2 f**).

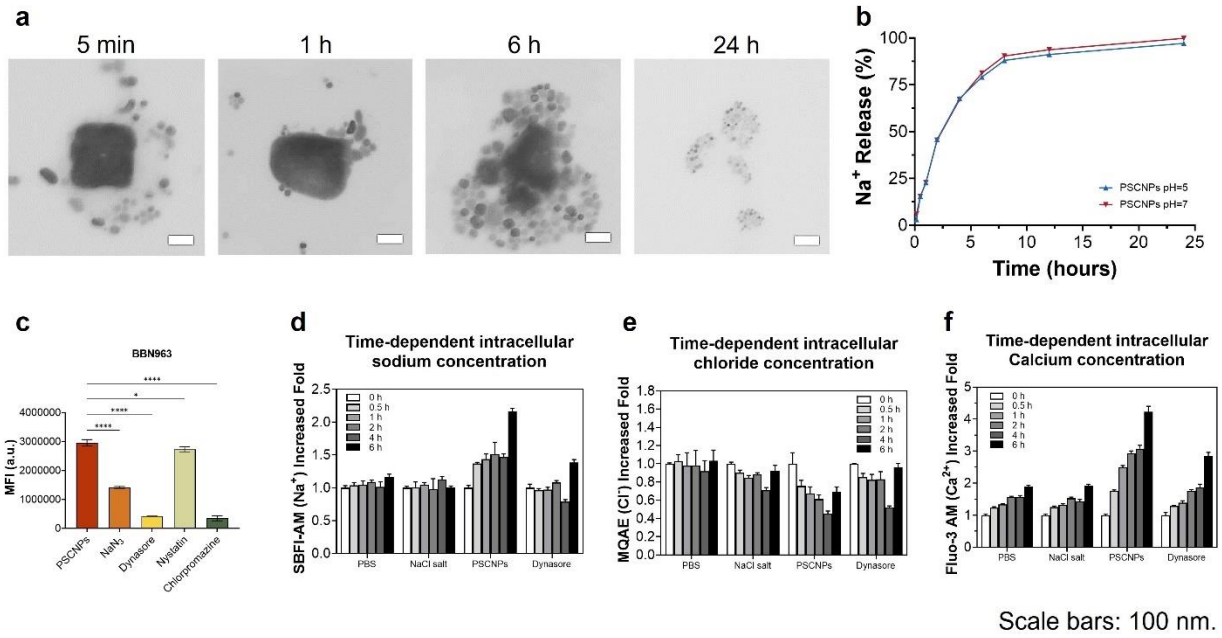

Figure 2.2. Nanoparticles degradation, endocytosis, and their impact on cellular ion homeostasis. a) TEM images showing the degradation process of PSCNPs in water over 24 h. Scale bar: 100 nm b) Release profiles of Na^+ from PSCNPs. Examined in sodium-free ammonium acetate buffer at different pH. c) Cell uptake analyzed by flow cytometry. BBN963 treated with RB-PSCNPs and co-incubated with endocytosis inhibitors including sodium azide, dynasore, nystatin, and chlorpromazine. *, $p < 0.05$; **, $p < 0.01$; ***, $p < 0.001$; ****, $p < 0.0001$. d) Histogram of intracellular SBFI-AM fluorescence signal changes relative to 0 h. e) Histogram of intracellular MQAE fluorescence signal changes relative to 0 h. Note, the MQAE signal is reversely correlated with Cl^- concentration. f) Histogram of intracellular fluo3-AM fluorescence signal changes relative to 0 h.

Impact of nanoparticles on cell viability and mechanism

We incubated PSCNPs with bladder cancer cells (**Figure 2.3 a**), including BBN963, UPPL1541, UMUC2, T24, MB49. We observed similar levels of cytotoxicity, with IC50 values

ranging from 194.5 to 289.4 μg/mL. Incubation with sodium pump inhibitor ouabain or chloride channels inhibitor niflumic acid significantly mitigated the nanoparticle toxicity (**Figure 2.3 h**). Meanwhile, NaCl salt up to 1000 μg/mL showed no harm to cells. Aged nanoparticles also showed significantly reduced or marginal toxicity to the cells (**Figure 2.3 c**). These results suggest that the toxicity of PSCNPs arises from their ability to deliver NaCl into cells.

To understand the mechanism behind the cell death, we pre-treated bladder cells with z-VAD-fmk or glycine, which are inhibitors for apoptosis and necrosis, respectively. Both z-VAD-fmk or glycine were able to partially mitigate PSCNPs-induced cell viability decrease (**Figure 2.3 f**), and the combination of the two agents could more efficiently restore viability drop (**Figure 2.3 g**). These results indicate that both apoptosis and necrosis were involved in PSCNPs induced cell killing. Meanwhile, 3-methyladenine (3-MA), an autophagy inhibitor, and ferrostatin-1, a ferroptosis inhibitor, failed to reverse the toxicity of PSCNPs (**Figure 2.3 e,f**).

We also evaluated the cytotoxicity of PSCNPs with other cells, including immune cells like macrophages (RAW264.7) and bone marrow dendritic cells (BMDCs), as well as primary cells like human primary prostate epithelial cells (HPrECs) and primary bladder epithelial cells (BdECs) (**Figure 2.3 a**). Similar to what was observed in previous studies, we found that these cells are much more tolerable to PSCNPs than bladder cancer cells. One factor of the difference could be differed endocytic activity between cancerous and normal cells. Indeed, flow cytometry studies showed that bladder cancer cells in general were associated with a much higher level of nanoparticle uptake than normal epithelial cells (**Figure 2.3 b**); this is attributed to an increased endocytosis activity of cancer cells relative to normal cells. Indeed, adding DMSO, which increases cell endocytosis, makes BBN cells even more susceptible to PSCNPs (**Figure 2.3 i**).

However, difference in endocytosis does not explain the relative resistance of macrophages and BMDCs, which are phagocytic cells and take up PSCNPs at a comparable or superior level to cancer cells. This is because a second factor, which is the difference in baseline sodium level, also plays a role. Specifically, the baseline sodium levels of cancer cells are 2-3 fold higher than not only normal epithelial cells but also macrophages and BMDCs (**Figure 2.3 d)**. When BBN cells were treated with monensin, a sodium ionophore that transports sodium into cells, the cells became much more sensitive to PSCNPs (**Figure 2.3 h**).

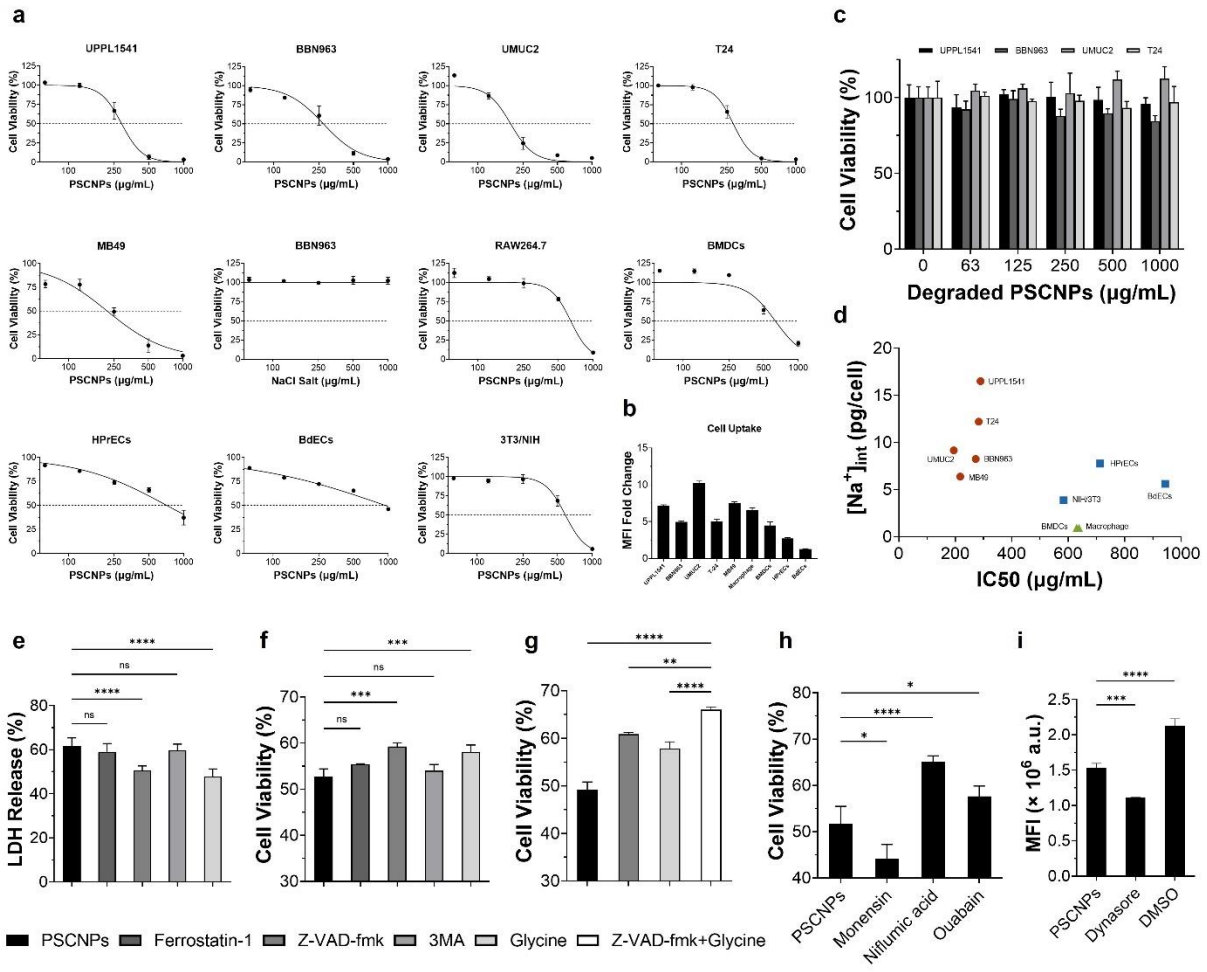

Figure 2.3. Impact of nanoparticles on cell viability and mechanism. a) Cytotoxicity of PSCNPs against a panel of cell lines, including bladder cancer cells, immune cells, and primary cells, measured by MTT assays. IC_{50} values were determined by log(inhibitor) vs. normalized response -- Variable slope in

GraphPad Prism. b) Cell uptake of PSCNPs with a panel of cell lines, results acquired and analyzed by flow cytometry. c) Cytotoxicity of degraded PSCNPs against four types of bladder cancer cells. d) The correlation between IC_{50} and the intracellular sodium concentration of each cell line. e) LDH release from PSCNPs treated BBN963 cancer cells and co-incubated with cell death pathway inhibitors, including ferrostatin-1 for ferroptosis, Z-VAD-fmk for apoptosis, 3MA for autophagy, glycine for necrosis. LDH was assessed by LDH Assay Kit-WST. f) Cell viability was evaluated by MTT assays to study the cell death patterns induced by PSCNPs. BBN963 cancer cells were pre-incubated with cell death pathway inhibitors for 1 h. g) BBN963 pre-treated with Z-VAD-fmk, glycine alone, or combination for 1 h, then test PSCNPs' impact on cell viability. h) Cell viability was evaluated by MTT assay. Before the addition of PSCNPs, BBN963 was pre-treated with sodium ionophore, monensin, ion channel inhibitors, niflumic acid, and ouabain respectively for 1 h. i) Flow cytometry analysis of cell uptake. BBN963 co-incubated with PSCNPs, dynasore, an endocytosis inhibitor, and DMSO, an endocytosis agonist was added 1 h before NP treatment. *, $p < 0.05$; **, $p < 0.01$; ***, $p < 0.001$; ****, $p < 0.0001$.

Nanoparticle-induced immunogenic cell death (ICD)

In addition to killing cancer cells, PSCNPs also promoted the secretion of ATP (**Figure 2.4 a**). This is associated with the ability of PSCNPs to cause cell necrosis, and as a result, a breached plasma membrane. Indeed, pre-treated with glycine or lipid antioxidants inhibited ATP secretion (**Figure 2.4 b**). Meanwhile, the secretion of HMGB1 (**Figure 2.4 d**) and the surface presentation of CRT was also elevated in cells treated with PSCNPs (**Figure 2.4 c**). We speculate these events are with the ability of PSCNPs to induce ER stress, possibly linked to the nanoparticle-induced oxidative stress increase or osmolarity increase.

These ICD markers are presumably damage-associated molecular patterns (DAMPs) that could bind receptors on the antigen presenting cells such as dendritic cells, activate them, and in term enhance innate and adaptive immunities. To investigate, we treated cancer cells with

PSCNPs and co-cultured the resulting cells with BMDCs. We first measured surface antigen presenting molecules, including both major histocompatibility complex (MHC) class I or II, as well as maturation markers, including CD205, CD80, and CD86. Flow cytometry results showed an increased population of $CD205^+$ (**Figure 2.4 f**), $MHCII^+$ (**Figure 2.4 g**), $CD86^+$ and $CD80^+$ (**Figure 2.4 h**) BMDCs, indicating the activation of BMDCs by PSCNPs treated cancer cells. We next measured inflammatory cytokines such as IL-12, IL-1, IL-6, and TNF-α in the supernatant of the co-culture. We found that PSCNPs treatment stimulated those cytokines secretion from BMDCs. Meanwhile, the secretion of IL-10, an anti-inflammatory cytokine, decreased over the PSCNPs treatment (**Figure 2.4 i**). Furthermore, we studied DC migration through a transwell experiment. We found that treatment of BBN963 cells with PSCNPs led to increased migration of DCs toward the cancer cells (**Figure 2.4 e**); this result is consistent with the surface and cytokine profile changes, confirming that PSCNPs prompted DC maturation and migration.

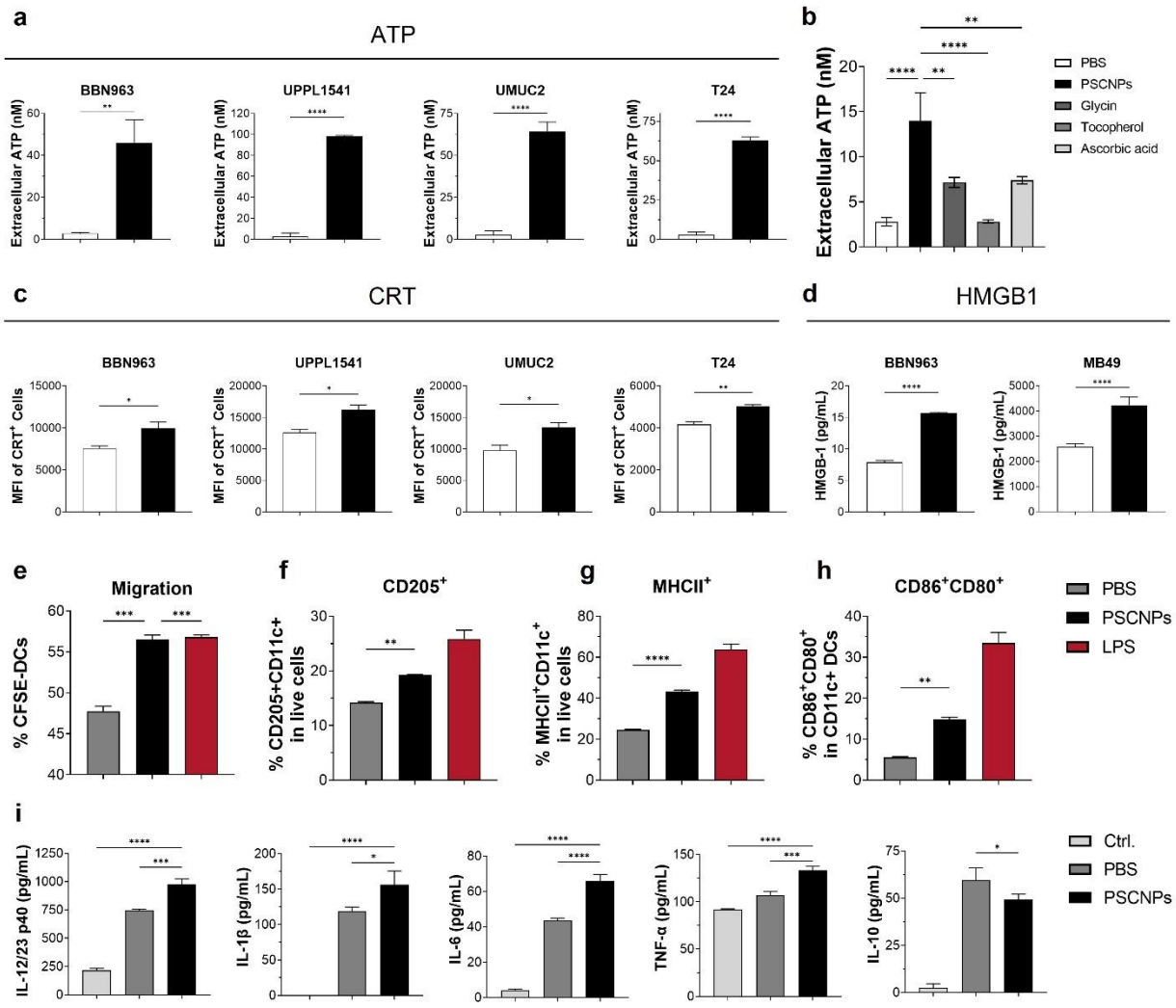

Figure 2.4. Nanoparticle-induced ICD. a) ATP release from a panel of bladder cancer cells. Cells were treated with 250 μg/mL PSCNPs for 2 h, then supernatants were collected for extracellular ATP content analysis by ATPlite-1step kit. b) Extracellular ATP release from PSCNPs-treated BBN963 inhibited by glycine, tocopherol, and ascorbic acid. c) CRT expression on a panel of bladder cancer cells that were treated with PSCNPs for 24 h. MFI was analyzed by flow cytometry. d) HMGB1 release from BBN963 and MB49 cells after PSCNPs treatment at 48 h. e) Percentage of CFSE-labeled DCs migrated to the lower chamber of the transwell plate. f) Histogram of $CD205^{+}CD11c^{+}$ population DCs. g) Histogram of $MHCII^{+}CD11c^{+}$ population of DCs. h) Histogram of $CD86^{+}CD80^{+}$ population DCs. i) Cytokines released

from DCs that co-incubated with NPs-treated BBN963 cancer cells. All cytokines were measured by R&D duoset ELISA kit. *, $p < 0.05$; **, $p < 0.01$; ***, $p < 0.001$; ****, $p < 0.0001$.

Impact of nanoparticles on TME and major organs

We then investigated the impact of PSCNPs on tumor microenvironment in syngeneic tumor model established with BBN963 cells. When the tumor size reached 50-100 mm^3, we intratumorally (i.t.) injected PSCNPs (30 μL, 3.25 mg, in PBS) on Day 0, 3, and 6 (**Figure 2.5 a**). After 7 days, we harvested tumors, spleens, and tumor-draining lymph nodes (TDLNs) for flow cytometric analysis. For controls, carrier only (PBS) and degraded PSCNPs were administered. Relative to carrier and degraded NPs only, treatment with PSCNPs led to an elevated population of mature DCs ($CD11c^+MHC\text{-}II^+$) in tumors (**Figure 2.5 b**). The $CD86^+$ DC population, in particular, was significantly increased in the PSCNPs group. We also observed increased frequencies of MHC-II^+ and $CD86^+$ DCs in TDLNs (**Figure 2.5 c**), indicating increased numbers of DCs migrating into the organ.

Next, we examined lymphocytes in tumors. PSCNPs led to an increased infiltration of cytotoxic T cells ($CD45^+CD3^+CD8^+$). Effector CTLs (IFN-γ^+ $CD45^+CD3^+CD8^+$) in particular, were significantly increased in the PSCNPs group relative to the PBS and degraded NP groups (**Figure 2.5 d**). Meanwhile, the frequency of Tregs ($CD45^+CD25^+CD4^+$) was decreased.

In addition, we tested combination of PSCNPs and αPD1, the latter of which was i.p. administered. We found that the frequencies of mature DCs in tumors were increased in the PSCNPs-αPD1 combination group relative to either PSCNPs alone or αPD1 alone (**Figure 2.5 b**). The frequencies of CTLs and effector CTLs were increased in the combination group relative to the αPD1 group (**Figure 2.5 d**). The CTL/Treg ratio was also higher with the combination

than with αPD1 alone. These results indicate that combining PSCNPs with αPD1 render the tumor microenvironment more pro-inflammatory.

We also observed increased frequencies of CTLs in the spleen (**Figure 2.5 f**). To examine whether the treatment cause systemic toxicity, we harvested organs including and examined the sample tissues. Histopathology found no morphology changes nor signs of toxicity in these organs (**Figure S2.4**).

Overall, our studies showed that PSCNPs alone or its combination with αPD1 can transform TME to boost immunities, without causing systemic toxicity.

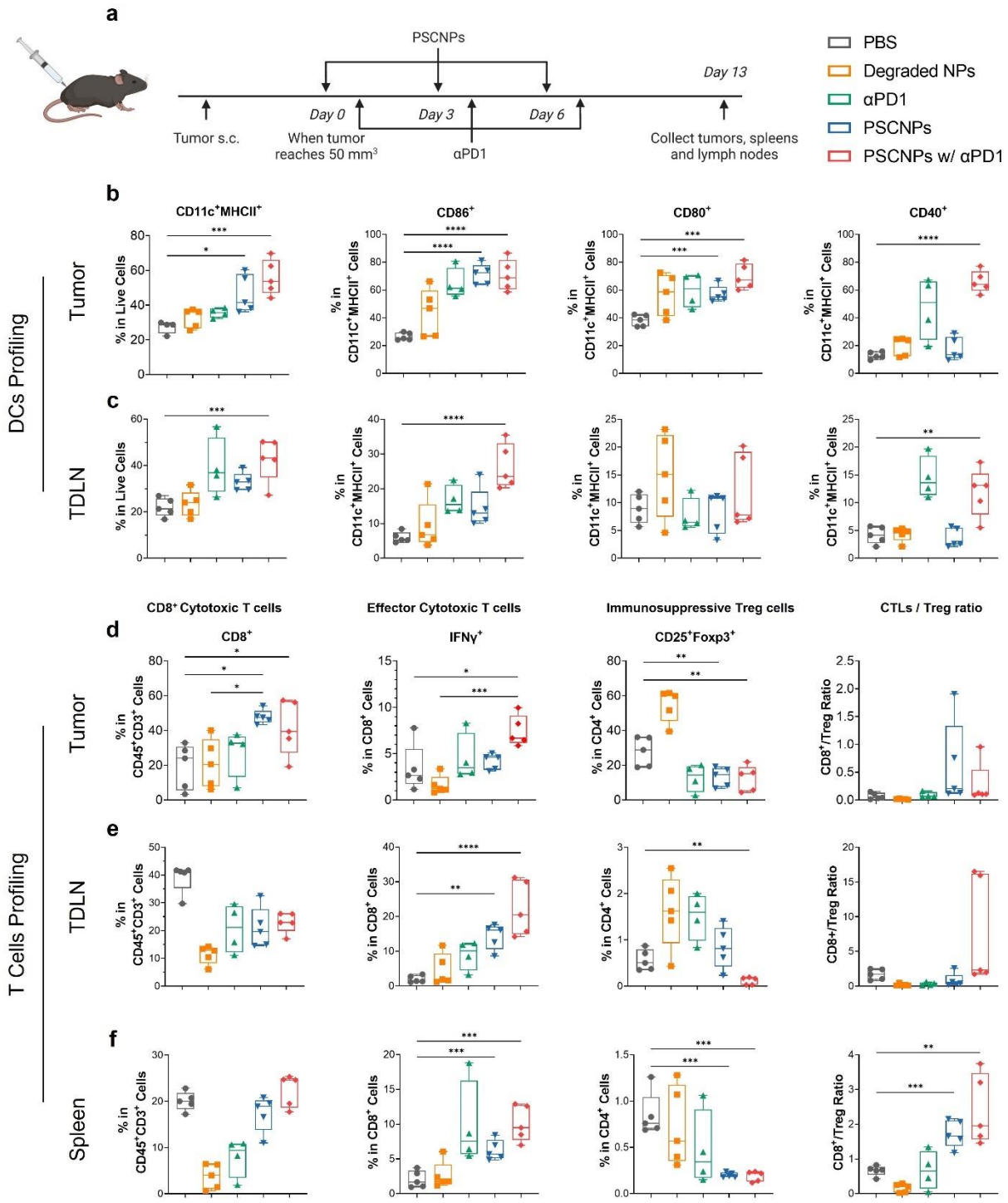

Figure 2.5. Impact of nanoparticles on TME and major organs. a) Scheme of in vivo experimental design and treatment groups. b) DCs profiling in tumor on day 7. Markers including MHCII, CD86, CD80, and CD40 were analyzed by flow cytometry. c) DCs profiling in TDLN on day 7. d) T cells profiling in tumor

on day 7. Markers including CD8, IFNγ, CD4, CD25, and Foxp3 were analyzed by flow cytometry. e) T cells profiling in TDLN. f) T cells profiling in the spleen. *, $p < 0.05$; **, $p < 0.01$; ***, $p < 0.001$; ****, $p < 0.0001$.

Test PSCNPs in subcutaneous tumor models

We next evaluated the therapeutic efficacy of PSCNPs in the MB49 model. We i.t. administered there doses of PSCNPs (30 μL, 3.25 mg, in PBS) every two days (**Figure 2.6 a**). For comparison, we also tested saline at the same NaCl concentration and degraded PSCNPs. Moreover, αPD1 alone and PSCNPs plus αPD1 were also tested. While degraded PSCNPs showed virtually no benefits, PSCNPs significantly inhibited tumor growth and extended animal survival (**Figure 2.6 b**). Histology found a significantly reduced cancer cell density and a decreased Ki-67 positive standing signal in the PSCNPs group (**Figure 2.6 f**). Further improvement was observed with the PSCNPs and αPD1 combination. Specifically, the tumor growth inhibition ratio (TGI, %) was 89.3%, and 64% for the PSCNPs w/ α-PD1, and the PSCNPs on day 31 respectively. Forty percent of the animals in the combination group remained tumor free on Day 90 (**Figure 2.6 c**). Meanwhile, no body weight loss and no acute toxicity to the major organs were observed throughout the study (**Figure 2.6 d**). For comparison, we also tested mitomycin c, which has been used in the clinic for bladder cancer management. While mitomycin c was effective in the first month, relapse ensued causing all animals in the group to die by Day 35 (**Figure S2.5**).

On Day 90, we administered live MB49 cells to the contralateral side of the survival animals. All of the animals were able to reject tumor establishment (**Figure S2.7**). To confirm whether immune response contributed to tumor suppression, we depleted $CD4^+$ or $CD8^+$ T cells and then began treatment with PSCNPs. While depletion of either type of T cells dampen the

treatment efficacy, $CD8^+$ T cell depletion more significantly worsen the outcome (**Figure 2.6 a**), indicating an important role CTLs played in the treatment.

We next tested PSCNPs and PSCNPs plus αPD1 in BBN963 tumor-bearing mice. Similarly, we observed no therapeutic benefits with saline and degraded PSNCPs, but significant tumor suppression with PSNCPs. The combination therapy led to even more effective tumor suppression (**Figure 2.6 g**).

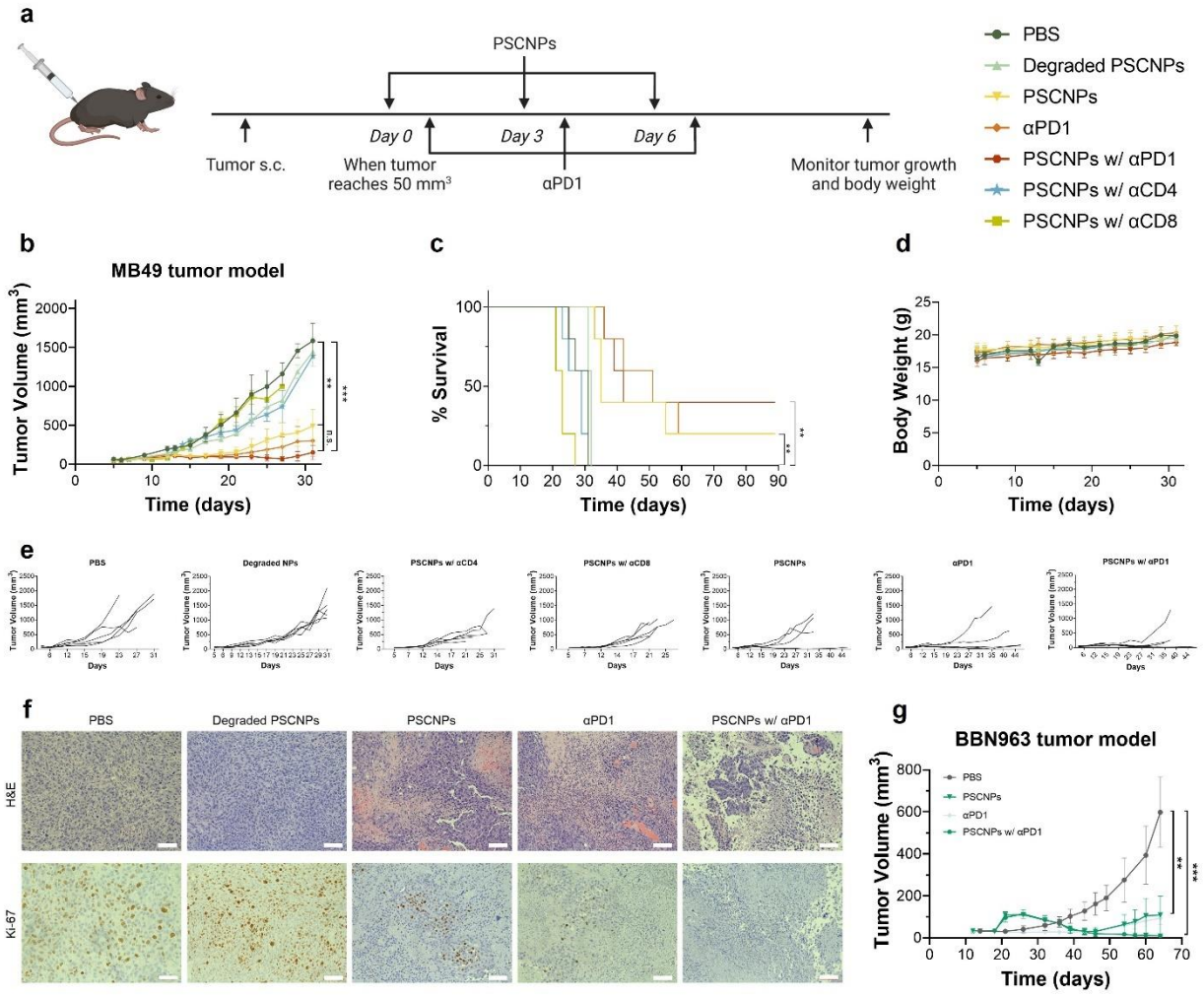

Figure 2.6. Test PSCNPs in subcutaneous tumor models. a) A schematic illustration of therapy study design and treatment groups. MB49 tumor model was established on C57BL/6 mice. b) MB49 tumor growth curve. c) Survival curve for MB49 tumor model. d) Mice body weight for MB49 tumor model. e)

Individual mice growth curve. f) H&E and Ki-67 staining of tumors. Scale bar: 100 μm. g) BBN963 tumor growth curve.

Summary

In this study, phospholipid-coated sodium chloride nanoparticles (PSCNPs) were synthesized and characterized, exhibiting controlled degradation and effective endocytosis by cancer cells. PSCNPs disrupted intracellular ion homeostasis, inducing cell death via apoptosis and necrosis, and promoted immunogenic cell death, leading to the activation and migration of dendritic cells. The PSCNPs selectively targeted bladder cancer cells, exhibiting low toxicity in normal and immune cells. *In vivo* experiments demonstrated that PSCNPs, alone or in combination with αPD1 checkpoint inhibitor, transformed the tumor microenvironment to boost immunity without causing systemic toxicity. And the combination of PSCNPs with αPD1 significantly enhanced the antitumor immune response, inhibiting tumor growth and prolonging survival in murine bladder cancer models. These findings highlight the potential of PSCNPs as a novel therapeutic strategy for bladder cancer treatment.

CHAPTER 3

EXPLORING SODIUM CHLORIDE NANOPARTICLES AS RADIOSENSITIZERS

Introduction

Our previous studies have shown that sodium chloride nanoparticles (SCNPs) can enter cells by endocytosis and release the sodium and chloride they contain. By effectively acting as ion carriers, we have shown that SCNPs can disrupt the osmotic balance and cause cancer cell death. However, the exact mechanism of cell death remains elusive. The ionic balance of cells is delicate and essential for cell survival, volume, and functions. It is speculated that the sodium and chloride fluctuations caused by SCNPs may spread to affect the levels of other ions in cells. Meanwhile, our previous study found that SCNPs also have a major impact on the redox balance of cells. However, the mechanism behind the increase in ROS is not entirely clear.

Intertumoral SCNPs have been shown to be effective as ablation therapy. However, we rarely saw complete tumor cures in animal studies. It is interesting to explore the combination of SCNPs with other conventional therapies. In particular, we believe that SCNPs can be used to sensitize cancer cells to radiation therapy. Radiation therapy ionizes molecules in cells, especially water, producing radicals such as hydroxyl radicals and superoxide. These ROS damage biomolecules, including DNA. It is hypothesized that SCNPs, with their ability to promote ROS, may work in conjugation with IR to enhance cancer cell killing.

In particular, we are interested in exploring SCNPs as a radiosensitizer for head and neck squamous cell carcinoma (HNSCC). HNSCC is the seventh most common malignancy,

accounting for nearly 4% of all cancers in the United States[50], and its incidence is expected to increase by 30% by 2030[51]. More than 60% of patients with HNSCC are diagnosed at a locally advanced stage, with a high risk of recurrence and poor prognosis[52]. Surgical resection is conventionally preferred but has poor outcomes in advanced HNSCC. Radiotherapy (RT) can be used either as an adjunct to surgery or as a definitive treatment for patients with unresectable HNSCC[53]. However, RT often causes toxicity to the teeth, gums, and salivary glands, and can severely affect patients' swallowing and speech[54, 55]. Chemo agents such as platinum agents or EGFR monoclonal antibodies can be used to enhance the efficacy of radiotherapy[53]. However, the combination increases the risk of systemic toxicities, including grade 3/4 neuropathy and nephrotoxicity[56, 57]. Furthermore, intrinsic or acquired resistance to radiotherapy or chemotherapy is common, especially in HPV-negative cases[58, 59]. Importantly, the overall 5-year survival rate for advanced HNSCC has barely improved over the past three decades. New treatment modalities are needed to improve efficacy without causing additional local and systemic toxicity to patients. We anticipate that SCNPs may address this need.

To improve cancer cell selectivity, we will explore the possibility of adding a tumor targeting ligand, specifically folate, to nanoparticles. The cognate receptors for folate, most notably the folate receptor, is a membrane-anchored protein that binds folates with high affinity and mediates folate transport into cells[60]. Folate receptor expression is detected in about half of HNSCC patients[61]. Meanwhile, its expression in normal tissues remains low[62], making folate an attractive HNSCC targeting ligand[63].

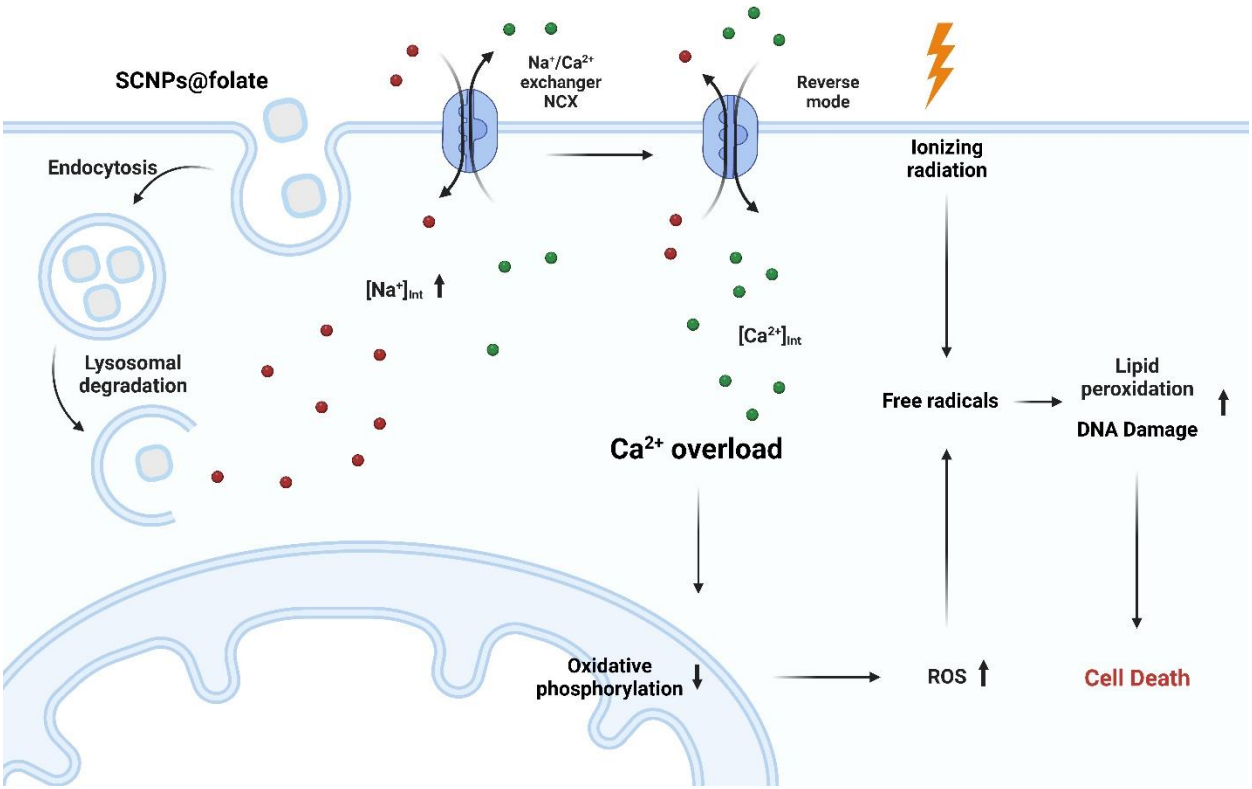

Figure 3.1. SCNPs@folate work in conjugation with IR to enhance cancer cell killing.

Nanoparticle synthesis and enhanced cell uptake

We synthesized sodium chloride nanoparticles (SCNPs) using a recipe modified from our previous protocol. Briefly, sodium acetate and oleylamine were dissolved in ethanol, and acetyl chloride in hexane was dropwise added into the mixture. The resulting nanoparticles were collected by centrifugation at room temperature. To improve the stability and tumor-homing effect of SCNPs, we imparted a layer of phospholipid on the surface using the thin-film hydration method. The phospholipids used were DSPE-PEG (2000) Amine and DSPE-PEG(2000) Folate mixed at a 9:1 ratio, with folate serving as a targeting ligand.

We investigated the cellular uptake of SCNPs@folate in two HNSCC cell lines, human SCC1 cells, and murine MOC1 cells. Both cell lines exhibit positive expression of the folate

receptor. We conducted an incubation experiment with Rhodamine-B-labeled SCNPs@folate and analyzed the internalization of the nanoparticles by fluorescence microscopy. As a control group, we also evaluated the cellular uptake of SCNPs nanoparticles coated only with DSPE-PEG (2000) Amine, termed SCNPs@PEG. While SCNPs@PEG showed successful internalization in both cell lines (**Figure 3.2 a, e**), possibly due to its positive surface charge, SCNPs@folate showed a higher level of uptake in both cell lines, which we attribute to the interaction between folate and the folate receptor (**Figure 3.2 a, e**). Sodium azide, a general endocytosis inhibitor, was able to suppress the cellular uptake of SCNPs@folate, suggesting that nanoparticle internalization was via endocytosis. Furthermore, we co-incubated nanoparticles with dynasore and chlorpromazine, which are inhibitors of dynamin GTPase activity and clathrin-coated pit formation, respectively. Both inhibitors were found to effectively reduce the cellular uptake of the nanoparticles. Meanwhile, nystatin, a lipid raft inhibitor, showed no significant effect on the cellular uptake of the nanoparticles.

We next assessed the effects of SCNPs@folate on intracellular sodium and chloride levels. We investigated this using SBFI-AM and MQAE, fluorogenic dyes that specifically label intracellular sodium and chloride, respectively. Note that the SBFI-AM fluorescence intensity is positively correlated with intracellular sodium concentration, whereas MQAE fluorescence intensity is inversely proportional to intracellular chloride concentration. Following incubation of SCC1 cells with SCNPs@folate, the SBFI-AM fluorescence intensity increased within the first two hours, indicating an increase in intracellular sodium concentration (**Figure 3.2 b**). This was attributed to the degradation of the nanoparticles within the cells, resulting in the release of sodium. Notably, we observed a decrease in SBFI-AM fluorescence intensity after 4 hours, which we attributed to some cells undergoing necrosis in the early hours of incubation with

SCNPs, as we had previously observed. Conversely, we found a significant decrease in MQAE fluorescence intensity during the first two hours (**Figure 3.2 c**), suggesting an increase in chloride levels. As controls, we also tested PBS and saline, both of which showed little effect on sodium or chloride levels. We repeated this study in MOC1 cells, and observed similar trends in intracellular sodium and chloride concentrations (**Figure 3.2 f, g**).

We then investigated the impact of SCNPs@folate on intracellular calcium levels or $[Ca^{2+}]i$ by using Fluo-3 AM, an intracellular calcium fluorophore. In both SCC1 and MOC1 cells, we observed a significant and time-dependent increase in Fluo-3 AM fluorescence intensity at early time points, followed by a decrease at 4 or 6 hours (**Figure 3.2 d, h**). The similarity between the SBFI-AM and Fluo-3 AM results leads us to believe that there is a close relationship between changes in sodium and calcium levels. In particular, we postulate that the increase in calcium was modulated by the sodium-calcium exchanger or NCX. Normally, the NCX imports sodium while exporting intracellular calcium; however, at high intracellular sodium concentrations, it operates in the reverse mode, importing calcium while exporting sodium[64]. We hypothesize that an increase in $[Na^{+}]i$ caused by SCNPs@folate will induce the NCX to import calcium, thereby driving up $[Ca^{2+}]i$. To test this hypothesis, we co-incubated cells with CGP37157, an NCX inhibitor. Our results indicated that the inhibitor significantly inhibited significantly inhibited the $[Ca^{2+}]i$ increase (**Figure 3.2 d, h**). Even greater inhibition was observed with SN-6, an inhibitor of the reverse mode of NCX.

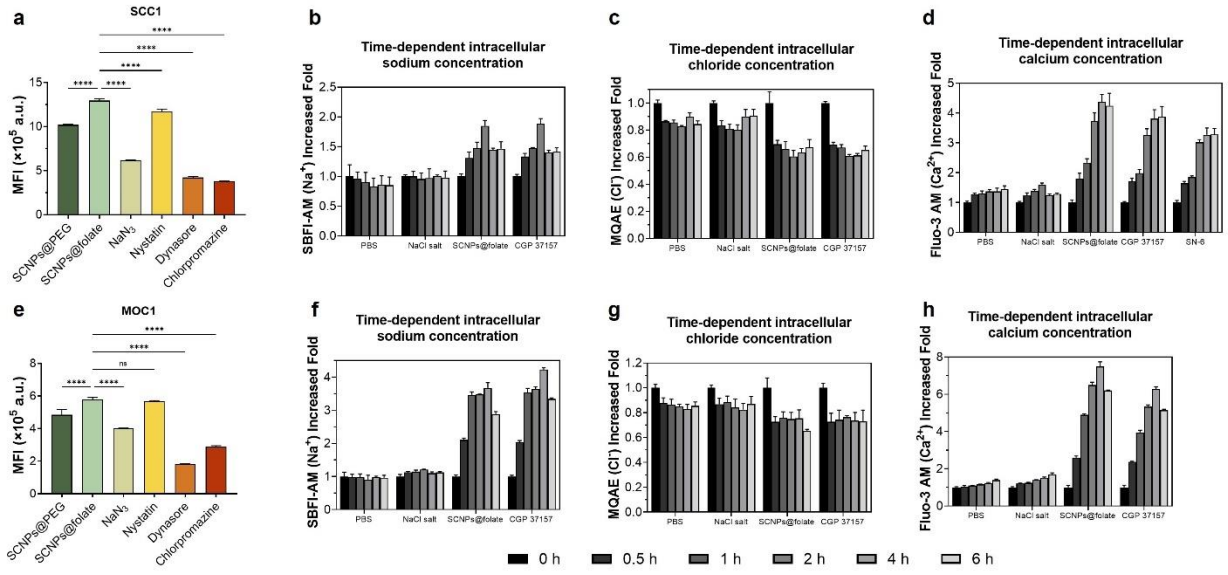

Figure 3.2. SCNPs@folate enhanced cell uptake. a, e) Cell uptake analyzed by flow cytometry. SCC1 cells or MOC1 cells were treated with RB-SCNPs@folate and co-incubated with endocytosis inhibitors including sodium azide, dynasore, nystatin, and chlorpromazine. b, f) Histogram of intracellular SBFI-AM fluorescence signal changes relative to 0 h. c, g) Histogram of intracellular MQAE fluorescence signal changes relative to 0 h. Note, the MQAE signal is reversely correlated with Cl^- concentration. d, h) Histogram of intracellular fluo3-AM fluorescence signal changes relative to 0 h. *, $p < 0.05$; **, $p < 0.01$; ***, $p < 0.001$; ****, $p < 0.0001$.

In vitro radiation sensitizing effects

An increase in intracellular calcium can cause decreased mitochondrial activity, leading to increased levels of cellular reactive oxygen species (ROS)[65]. It is hypothesized that SCNPs@folate, by inducing calcium influx, has the potential to augment cellular oxidative stress. To evaluate this hypothesis, we incubated SCC1 with SCNPs@folate and measured changes in the levels of cellular superoxide ($\bullet O_2^-$) and hydroxyl radical (•OH) levels using dihydroethidium (DHE) and aminophenyl fluorescein (APF) as radical sensors, respectively. The results showed that both DHE (**Figure 3.3 a**) and APF (**Figure 3.3 b**) fluorescence were

significantly increased, indicating a significant increase in radical levels. Similar increases in radical levels were also observed in MOC1 (**Figure 3.3 f, g**) and MOC2 cells (**Figure 3.3 k, l**).

Furthermore, we investigated the effects of irradiation alone or in combination with SCNPs@folate on cellular ROS. Irradiation alone caused a moderate increase in the levels of both $\bullet O_2^-$ and •OH in all three cell lines. When combined with SCNPs@folate, both radical levels increased significantly (**Figure 3.3 a, b**). To further understand the effects on oxidative stress, we assessed the activity of superoxide dismutase (SOD) and the level of glutathione (GSH) in SCC1 and MOC1 cells. SOD is used by cells to catalyze the dismutation of harmful superoxide radicals to hydrogen peroxide[66]. GSH is an important scavenger of ROS and a key regulator of cellular oxidative homeostasis[67]. Our results showed that the combination of SCNPs@folate and irradiation resulted in higher levels of SOD activity compared to either treatment alone (**Figure 3.3 c**). We attributed the SOD activity increase to a cell survival response to elevated ROS. In addition, we observed a significant reduction in the ratio of reduced (GSH) to oxidized (GSSG) GSH (**Figure 3.3 d, e**) in cells treated with the combination of SCNPs@folate and IR. Taken together, our results suggest that SCNPs@folate in combination with IR can synergistically increase cellular oxidative stress[68].

Increased oxidative stress would cause damage to cellular components, including DNA and lipids[69]. To investigate this, we performed γ-H2AX staining and lipid peroxidation assays, including the TBARS and C11BODIPY assays. We found that SCNPs@folate alone caused significant double-strand breaks (**Figure 3.3 o**), which was attributed to the increase in ROS levels induced by SCNPs@folate and the subsequent oxidative damage. The combination of SCNPs@folate and IR further increased DNA damage (**Figure 3.3 q**). Similarly, SCNPs@folate or the combination of SCNPs@folate and IR resulted in significant lipid peroxidation as

evidenced by increased levels of malondialdehyde (MDA) (**Figure 3.3 m**) and C11BODIPY fluorescence (**Figure 3.3 n**). It should be noted that IR alone was not effective in inducing lipid peroxidation.

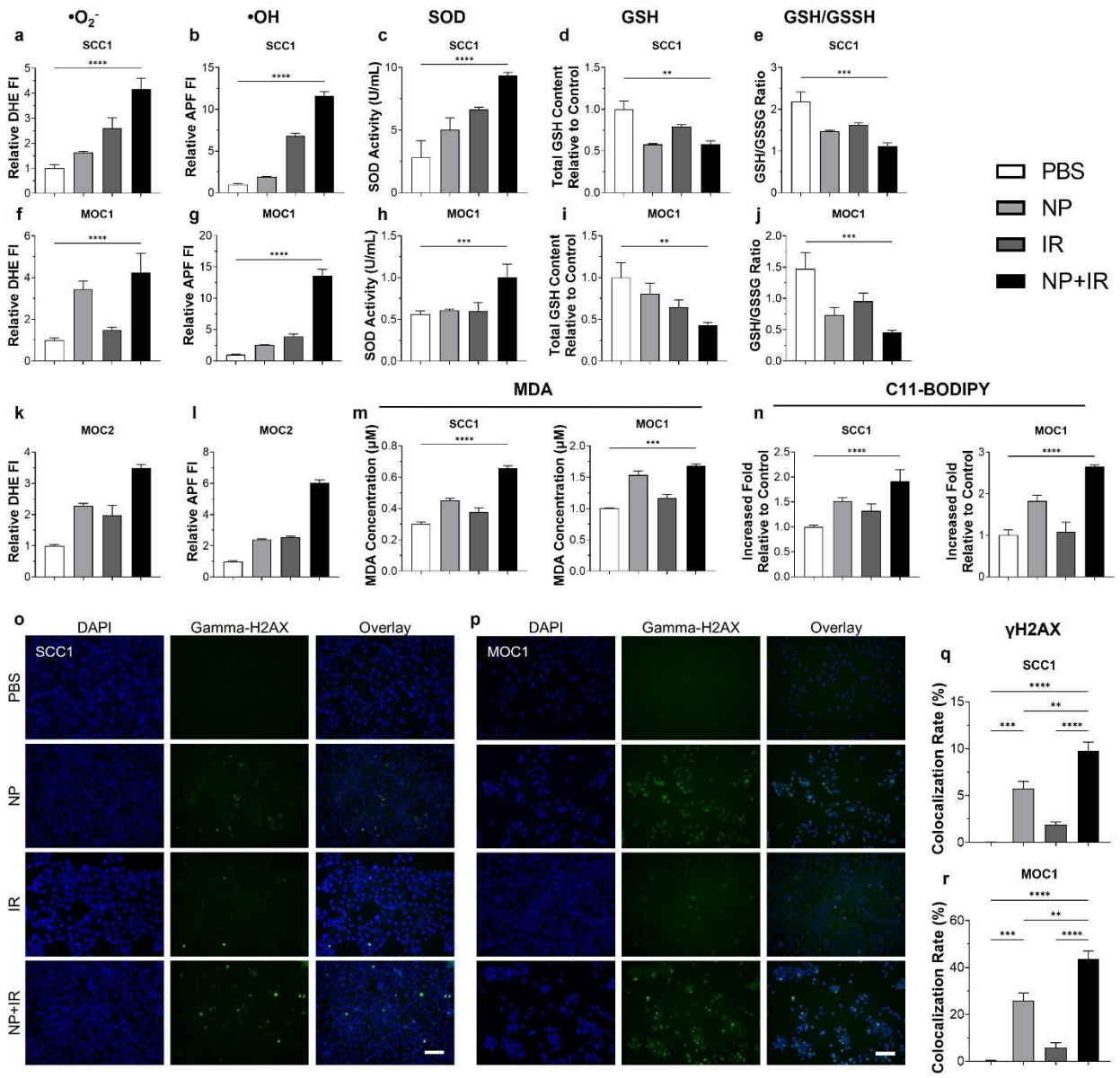

Figure 3.3. *In vitro* radiation sensitizing effects of SCNPs@folate. Cellular oxidative stress was induced by SCNPs@folate and IR treatment (5 Gy), as evidenced by a, f, k) Elevated cellular superoxide levels on SCC1, MOC1, and MOC2 cells, measured by DHE assay. Relative to the PBS group. b, g, l) Cellular hydroxyl levels on SCC1, MOC1, and MOC2 cells, measured by APF assay. Relative to the PBS

group. c, h) SOD activities on SCC1, MOC1 cells, measured by superoxide dismutase assay kit. d, i) Total GSH content on SCC1, MOC1 cells. e, j) GSH to GSSH ratio. Lipid peroxidation induced by SCNPs@folate and IR was evidenced by m) MDA levels. n) C11-BODIPY fluorescence changes. *, $p < 0.05$; **, $p < 0.01$; ***, $p < 0.001$; ****, $p < 0.0001$.

In vitro cytotoxicity as radiosensitizers

The ability of SCNPs@folate to increase oxidative stress and DNA and lipid damage leads to the speculation that the nanoparticles may be used as radiosensitizers. To investigate this, we treated SCC1 and MOC1 cells with SCNPs@folate and then exposed the cells to IR (5 Gy). We measured cell viability using the MTT assay and compared the results with cells treated with SCNPs@folate alone or IR alone. We found that IR alone had little to moderate effect on cell viability, the combination of SCNPs@folate and IR resulted in significantly enhanced cell death (**Figure 3.4 a**). We calculated the synergy factor using CDI= AB/A×B, where A, B represent the individual treatment efficiency to control group respectively. Our results showed that the SF was less than 1 for both cell lines (0.93 for SCC1 and 0.79 for MOC1), indicating a clear synergy between SCNPs@folate and IR. For comparison, we also tested SCNPs@PEG and found that it had lower stand-alone toxicity and radiosensitizing effects than SCNPs@folate.

The radiosensitizing effects were attributed, at least in part, to the increase in calcium levels induced by SCNPs@folate. This is evidenced by the observation that diltiazem, an NCX inhibitor, can moderately reduce cell death caused induced by the SCNPs@folate-IR combination (**Figure 3.4 d**). We also measured cell survival using the LDH assay and we found that diltiazem can similarly reduce cell death caused by the combination in both SCC1 and MOC1 cells (**Figure 3.4 e**).

Finally, we evaluated the radiosensitizing effects of SCNPs@folate by the clonogenic assay using SCC1 cells. At 5 Gy, the survival fraction at 14 days was 33.2. This number was reduced to 22.4 when SCNPs@folate was applied at 25 μg/mL and to 8.7 when SCNPs@folate was 50 μg/mL. Taken together, these results confirm that SCNPs@folate can work in synergy with IR to enhance cancer cell killing.

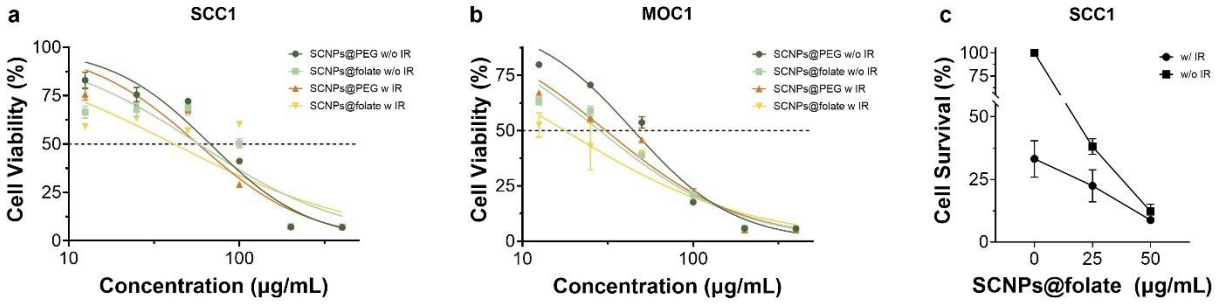

Table: IC50

IC50	SCNPs@PEG w/o IR	SCNPs@folate w/o IR	SCNPs@PEG w/ IR	SCNPs@folate w/ IR
SCC1	67.48	57.85	57.19	41.46
MOC1	44.69	28.39	30.77	17.69

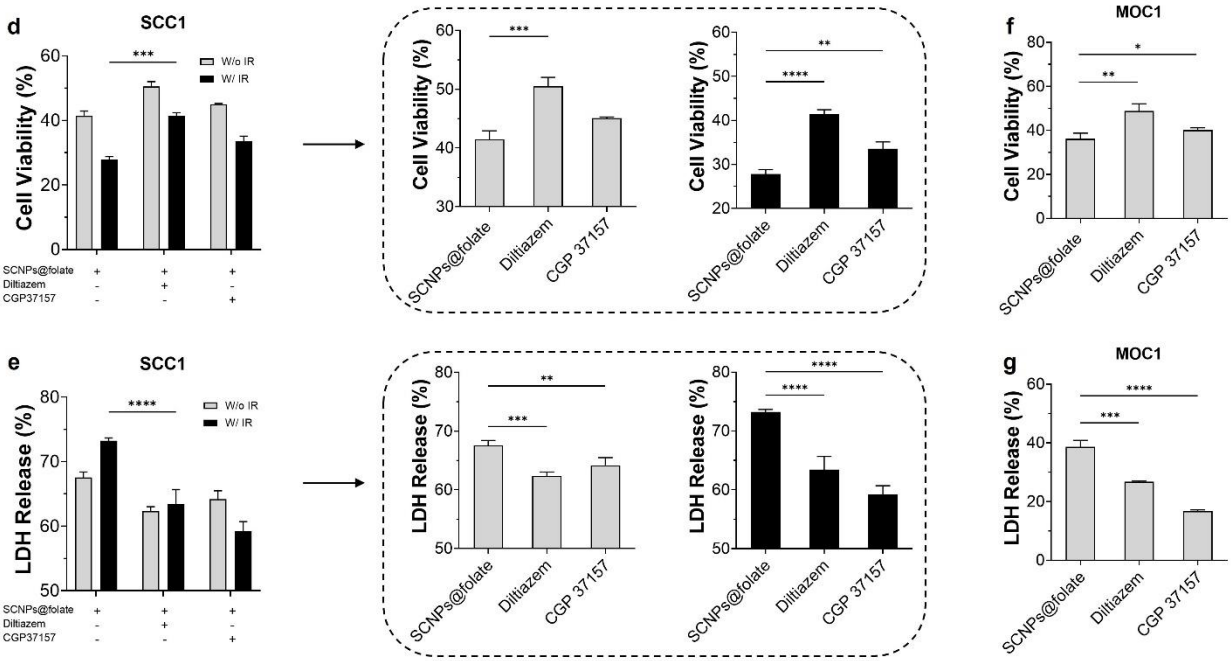

Figure 3.4. *In vitro* cytotoxicity as radiosensitizers. a, b) SCNPs@folate cytotoxicity to SCC1 and MOC1 were measured by MTT assay at 24 h. c) Clonogenic assay, tested with SCNPs@folate and 5 Gy IR. d, f) Cell viability changes of SCNPs@folate-treated SCC1 or MOC1 co-incubated with sodium-calcium

exchanger (NCX) inhibitors. e, g) LDH release from SCC1 or MOC1 treated with SCNPs@folate. NCX inhibitors were added to study the impact on the LDH release. The table in the middle summarized IC_{50} of different SCNPs treatments. *, $p < 0.05$; **, $p < 0.01$; ***, $p < 0.001$; ****, $p < 0.0001$.

In vivo therapy study

We then evaluated the radiosensitizing effects of SCNPs@folate in vivo. We tested this in a subcutaneous tumor model established with MOC1 cells on C57BL/6 mice (n=5). When the tumor size reached 50 mm^3, we injected SCNPs@folate (30 μL, 3.25 mg/mL, in PBS) intratumorally (i.t.) into the animals, followed by irradiation at 4 hours (**Figure 3.5 a**). A total of three treatments were given two days apart. For comparison, PBS, IR alone, and SCNPs@folate alone were also tested. Relative to the PBS control, both SCNPs@folate and IR moderately suppressed tumor growth. With the combination of the two, we observed a remarkable tumor suppression of 81.5% on Day 52 (**Figure 3.5 b**). After 80 days, 60% of the animals in the combination group remained alive and tumor-free (**Figure 3.5 c**). Meanwhile, we observed no acute toxicity of the combination treatment and no effect on the animals' body weight (**Figure 3.5 d**).

In a separate study, we euthanized animals receiving the four treatment groups on Day 52 and performed post-mortem histopathology (**Figure 3.5 f**). Hematoxylin/eosin (H&E) staining revealed reduced cell density and areas of cellular damage in animals treated with the SCNPs@folate-IR combination. Ki67 staining showed a significantly reduced positive staining in the combination group relative to animals receiving either SCNPs@folate alone or IR alone, confirming the efficacy of the approach. Meanwhile, no signs of toxicity were found in the major organs (**Figure S3.1**).

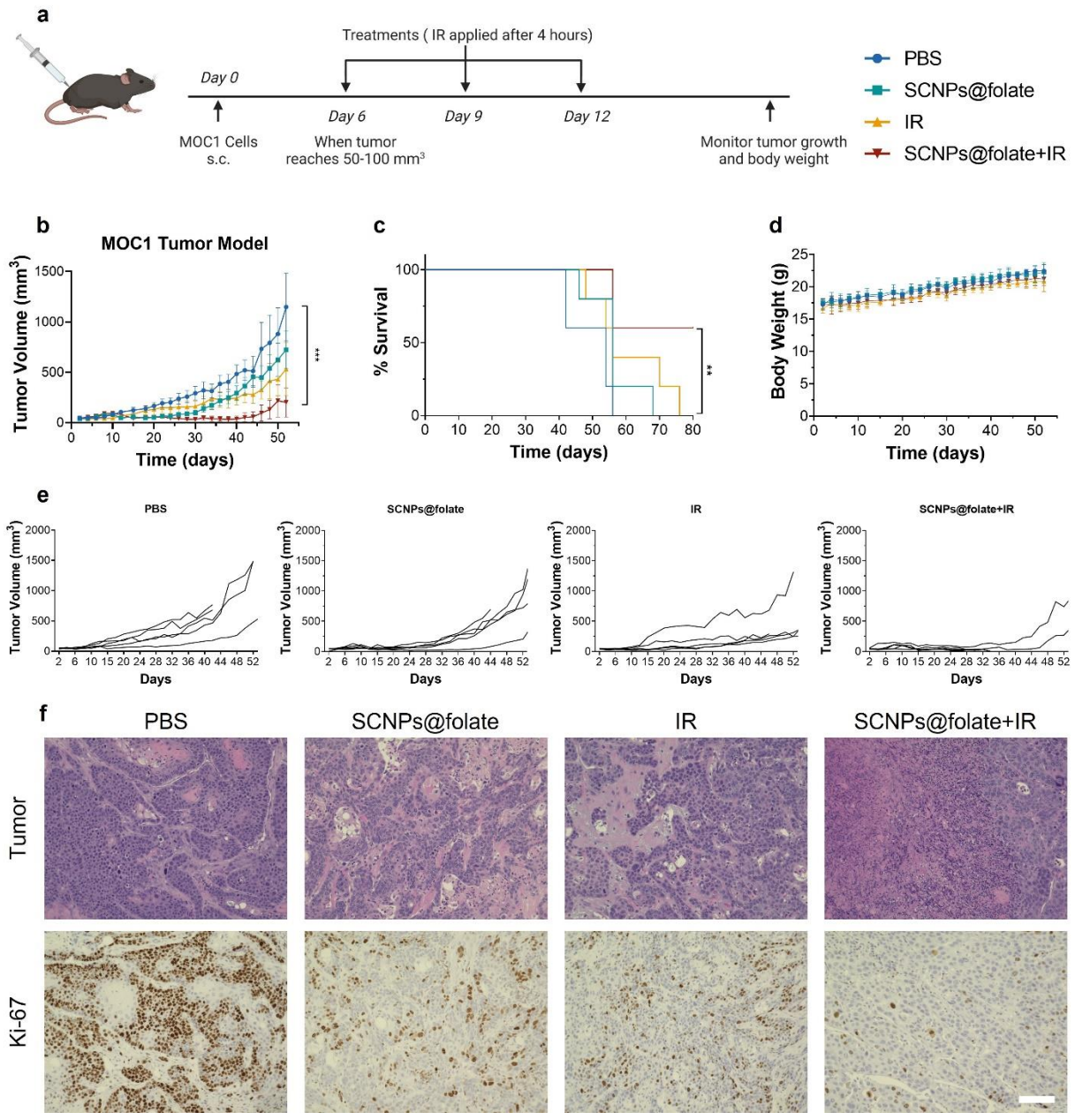

Figure 3.5. *In vivo* therapy study. a) Scheme of in vivo therapy flow design and treatment groups. MOC1 tumor model was established. b) MOC1 tumor growth curves. c) Survival curves. d) Mice's body weight. e) Individual tumor growth curves. f) H&E and Ki-67 staining of tumors. *, $p < 0.05$; **, $p < 0.01$; ***, $p < 0.001$; ****, $p < 0.0001$.

Summary

In this study, we synthesized and characterized folate-conjugated sodium chloride nanoparticles (SCNPs@folate) and explored their potential as radiation sensitizers in HNSCC. Our results showed that the nanoparticles exhibited proficient cellular uptake and increased intracellular levels of sodium and chloride. Interestingly, the increase in sodium levels also causes calcium influx through the NCX, triggering an increase in ROS. We found that the ROS-promoting effect works in tandem with IR, leading to GSH depletion, resulting in DNA and lipid damage, and ultimately cell death. Our in vitro results showed that there is a synergistic effect between SCNPs@folate and IR. In vivo studies showed that intratumorally injection of SCNPs@folate combined with irradiation resulted in a significant improvement in tumor growth inhibition compared to IR alone and a higher percentage of tumor-free mice. Taken together, our studies suggest a great potential of SCNPs@folate as a radiosensitizer in HNSCC.

CHAPTER 4

IRON OXIDE NANOPARTICLES ENHANCE RADIOTHERAPY BY INDUCING THE SECRETION OF ATP AND HMGB1 FROM MACROPHAGES

Introduction

As mentioned in Chapter 2, immunogenic cell death (ICD) is a form of cell death that triggers an immune response by releasing damage-associated molecular patterns (DAMPs) from dying cells[70]. The release of DAMPs such as ATP and HMGB1 from dying cells promotes the maturation and activation of dendritic cells (DCs), which are critical in initiating an adaptive immune response against the dying cells[71]. DCs express purinergic receptors and TLR4 that recognize ATP and HMGB1, respectively[72]. Binding of these DAMPs to their respective receptors triggers DC maturation and activation, leading to antigen presentation to T cells and initiation of a robust immune response[73]. Insufficient secretion of ATP and HMGB1 from dying cells is one reason why some cancer treatments such as irradiation therapy[74] and chemotherapy can sometimes fail to elicit a robust immune response. Strategies aimed at increasing the secretion of DAMPs from dying cells have been investigated to improve cancer treatment. One such strategy is combining chemotherapy with photodynamic therapy to enhance ICD[75]. Another approach involves the use of immunomodulatory agents such as toll-like receptor agonists[76].

Macrophages are a type of immune cell that plays a critical role in host defense against infection and cancer. Macrophages are responsible for engulfing and phagocytosing foreign

particles and microorganisms[77]. After taking the particles, macrophages may secrete cytokines and chemokines that recruit and activate other immune cells including dendritic cells and T cells to the site of infection or inflammation. Recent studies show that exposure to inorganic nanoparticles can direct the polarization of macrophages[78] and affect the functions of macrophages[79]. For instance, iron oxide nanoparticles lead to the production of reactive oxygen species (ROS) and the release of proinflammatory cytokines such as TNF-α[80]. Exposure to inorganic nanoparticles can also affect the secretion of ATP and HMGB1 from macrophages[81]. How this would affect the activation of DCs, and the adaptive immune response however has rarely been studied.

In this study, we investigated whether loading macrophages with metal oxide nanoparticles would affect their secretion of DAMPs, including ATP and HMGB1, which in turn impact tumor microenvironment. In particular, we asked whether nanoparticle-loaded macrophages can enhance the immune response triggered by irradiation. We studied three nanoparticles made of iron oxide, zinc oxide, and aluminum oxide. These nanoparticles have been widely investigated for bio-applications and were reported to be immune modulators. Our hypothesis is that nanoparticles can boost macrophages' secretion of ATP and HMGB1, which supplement those secreted from cancer cells over irradiation thus enhancing anti-tumor immune response.

Nanoparticles characterization and effect on macrophages

We tested four commercially available inorganic nanoparticles, including Iron (III) oxide NPs (Fe2O3, abbr. ION), Aluminum oxide NPs (Al2O3, abbr. AON), and Zinc oxide NPs (ZnO,

abbr. ZON) for their impact on macrophages. We started by characterizing the size (**Figure 4.1 e, f, g**), morphology (**Figure 4.1 a, b, c**), and zeta potential (**Figure 4.1 h**) of the nanoparticles.

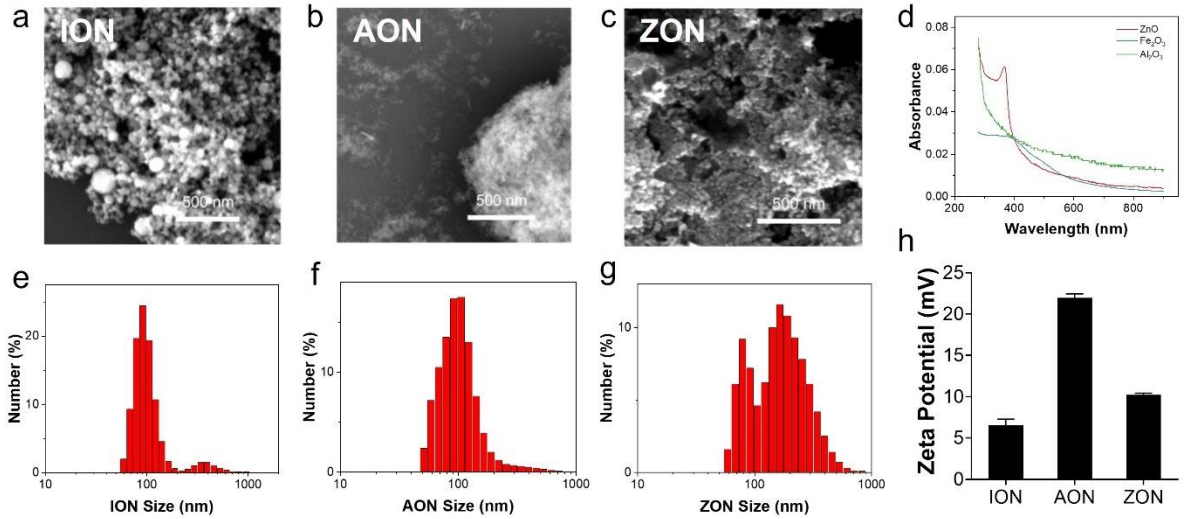

Figure 4.1. Nanoparticles characterization. SEM of (a) ION, (b) AON, (c) ZON. DLS of (e) ION, (f) AON, (g) ZON. d) UV-vis spectra. h) Zeta potential of ION, AON, ZON.

We then tested the nanoparticles in vitro with RAW 264.7 cells (**Figure 4.2 l**). While all three nanoparticles showed minimal toxicity below 1.0 μg/mL (based on metal concentrations), there was a marked drop of cell viability when the concentration of ZON was above 2.0 μg/mL (**Figure 4.2 a**). We next tested the impact of the nanoparticles on cell functions. In particular, we measured ATP and HMGB1 release from nanoparticle-treated RAW 264.7 cells. All three nanoparticles promoted the secretion of ATP and HMGB1 (**Figure 4.2 b, e**). However, ZON induced ATP secretion at 5 μg/mL but the secretion dropped markedly once the concentration was above 10 μg/mL (**Figure 4.2 d**). Similarly, AON showed a relatively narrow effective concentration range for promoting HMGB1 (**Figure 4.2 e**). Nonetheless, based on ATP and HMGB1 secretion, we determined the optimal concentrations for the nanoparticles, which are 40

μg/mL for IONs, 5 μg/mL for ZON, and 80 μg for AONs. Note that surface exposure of CRT, another classical ICD marker, was not elevated at these particle concentrations (**Figure S4.1 a**).

Next, we examined the impact of the nanoparticles on macrophage polarization at the selected concentrations. All three nanoparticles promoted the expression of M1[82] markers including CD86[83] and iNOS[84] (**Figure 4.2 i, j**). Interestingly, AON and ZON also induced CD206[85], a M2 marker[86] (**Figure 4.2 k**), whereas ION showed no such impact. Meanwhile, all three nanoparticles had little impact on TNF-α and IL-10 (**Figure S4.1 b, c**), which are pro- and anti-inflammatory cytokines, respectively.

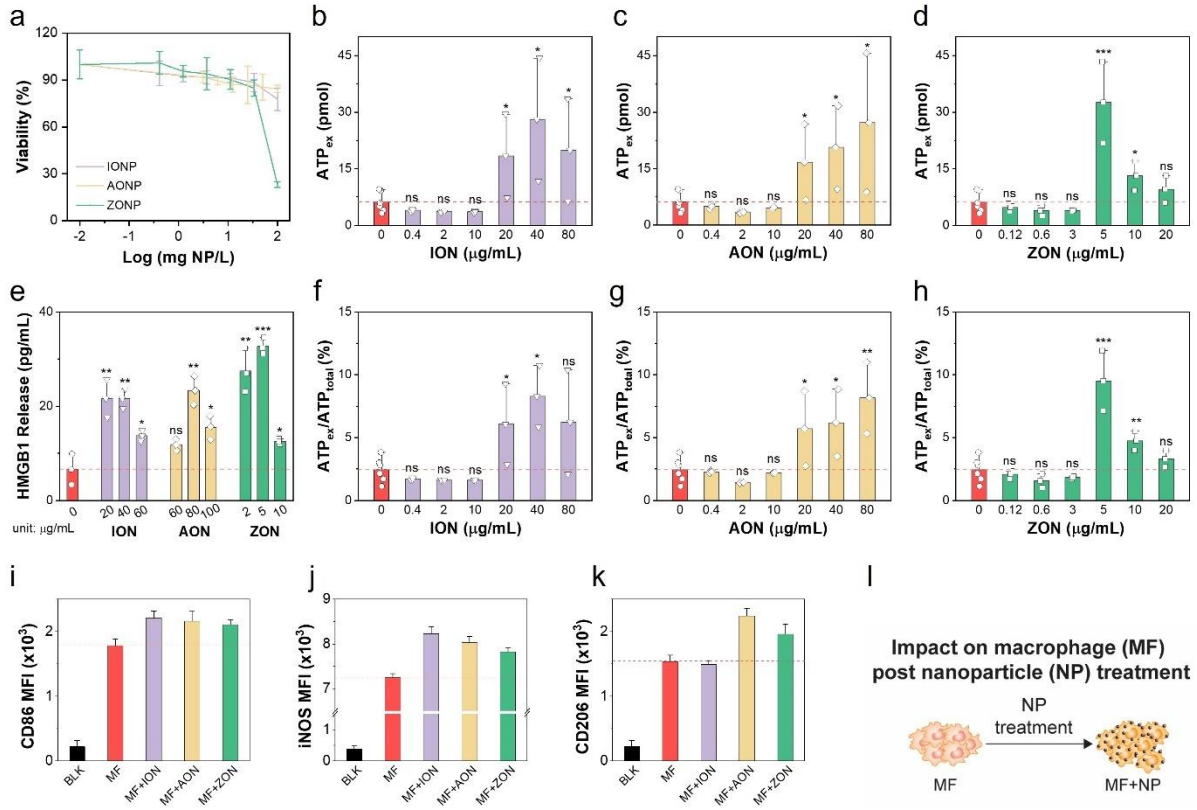

Figure 4.2. Impact of NPs on macrophages. a) Cytotoxicity of different nanoparticles (NPs) on RAW264.7 cells. Measured by MTT assay via 24 h incubation. Iron oxide NP (ION), aluminum oxide NP (AON) and zinc oxide NP (ZON) were selected and incubated with RAW264.7 cells for 2 h followed by medium replacement, another 24 h incubation, and assessment of b-d) ATP release by luminescence-

based ATP assay and e) HMGB1 release by ELISA. Specifically, b-d) extracellular ATP by pmol and f-h) the ratio of extracellular ATP to total ATP by %. Impacts on macrophages post 2 h treatment of NPs were evaluated using flow cytometry by the expressions of i) CD86, k) CD206, j) iNOS (Inducible nitric oxide synthase). l) Illustration of NP-laden macrophages. *, $p < 0.05$; **, $p < 0.01$; ***, $p < 0.001$; ****, $p < 0.0001$.

The potential impacts on cancer cells and dendritic cells

We then investigated whether macrophages under the influence of the nanoparticles affect cancer cell growth. We studied this using a transwell assay, where we loaded nanoparticle-loaded RAW264.7 cells into the insert and seeded 4T1 cells to the bottom chamber. Annexin V-FITC/PI staining found no signs of increased cell apoptosis or necrosis (**Figure 4.3 b**). This result suggests that soluble secretions from nanoparticle-loaded macrophages do not directly kill cancer cell death (**Figure 4.3 a**).

We also investigated the impact of macrophage secretions on surface CRT of cancer cells, another ICD marker. We tested this with both 4T1 cells with or without pre-irradiation by X-rays (5 Gy). We found that presence of macrophages promoted CRT presentation on cancer cell surface. However, there was no different between macrophages and nanoparticle-loaded nanoparticles. In other words, ION, AON or ZON do not enhance the ability of macrophages to induce surface exposure of CRT on cancer cells (**Figure 4.3 c**).

We anticipated that ATP and HMGB1 secreted from macrophages can supplement with those secreted from dying cancer cells, thus improving DC activation, maturation, and migration. We tested this with B16-OVA cells, RAW264.7 cells, and bone marrow derived dendritic cells (BMDCs). Briefly, we first incubated RAW264.7 cells with either ION, ZON, or AON nanoparticles; we then collected the supernatant, and added it to the incubation medium of

BMDCs. We found that ION-, but not AON- or ZON-loaded macrophages, induced DC maturation, marked by an increased expression of CD80 (**Figure 4.3 f**) and CD86 (**Figure 4.3 e**). MHCII expression was also induced, indicating increased antigen presentation (**Figure 4.3 d**).

We also evaluated DC migration and maturation with irradiated (5 Gy) B16-OVA cells. Similarly, we found that incubating macrophages with ION significantly enhanced the recruitment of DCs (**Figure 4.3 k**), induced the expression CD80 (**Figure 4.3 j**), CD86 (**Figure 4.3 i**), and MHCII (**Figure 4.3 h**) of DCs. The population of SIINFEKL-H-2Kb (**Figure 4.3 g**) was increased, suggesting that ION promoted DC maturation and antigen presentation. Based on these results, we selected ION for further experiments.

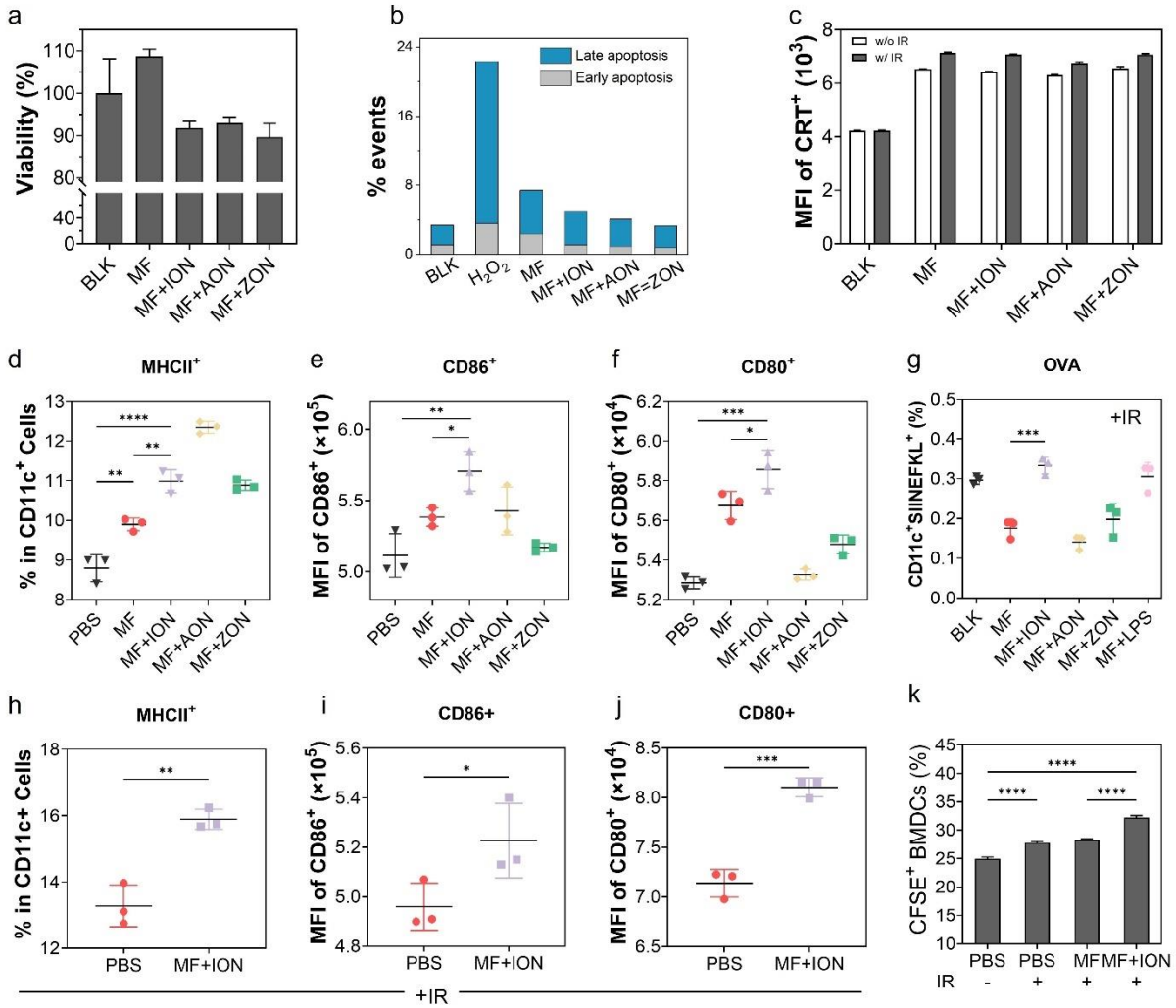

Figure 4.3. The potential impacts on cancer cells and dendritic cells. a) Assessment of cancer cell viability post 24 h co-incubation with MF/MF+NP using MTT assay. b) The apoptosis using Annexin V-FITC/PI. c) Surface expression of CRT on cancer cells post 30 min co-incubation with the conditioned medium supernatants from MF/MF-NP. MFI results were obtained through flow cytometry. BMDCs were incubated with supernatants collected from NPs-treated macrophages and added into the upper chamber of the transwell plate, while 4T1 breast cancer cells were seeded in the lower chamber, naïve, or irradiated (5 Gy). Assessment of DCs maturation and activation markers d) MHCII, e) CD86, f) CD80, and antigen presentation g) OVA. The expression of h) MHCII, i) CD86 j) CD80) was enhanced on DCs when incubated with secreted soluble signal molecules by MF+NP compared to RT only group. k) CFSE-label BMDCs migration. *, $p < 0.05$; **, $p < 0.01$; ***, $p < 0.001$; ****, $p < 0.0001$.

Impact of ION-laden macrophages on tumor microenvironment *in vivo*

We then investigated the impact of ION-laden macrophages on tumor microenvironment in vivo. We tested this in B16OVA-bearing mice. To trigger antigen release, RT was applied to tumors prior to the injection of ION-laden macrophages. After one week, we euthanized the animals and harvested tumors for analysis. We found that abundance of both DCs (**Figure 4.4 a**), and $MHCII^+$ DCs (**Figure 4.4 b**) were markedly increased in animals treated with ION-laden macrophages. We also observed an increased population of M1 macrophages (**Figure 4.4 c**) and a diminished population of M2 macrophages (**Figure 4.4 d**) in tumors. The M1/M2 ratio was increased with ION-laden macrophages plus IR relative to IR alone.

Meanwhile, the ION-laden macrophages also boosted the adaptive immunity. Specifically, we found an increased tumor infiltration of cytotoxic T cells ($CD3^+CD8^+$) (**Figure 4.4 e**). Relative to macrophages alone, ION-laden macrophages also showed an increased population of activated T cells ($CD69^+$ CTLs) (**Figure 4.4 f**). Moreover, while injection of

macrophages had no significant impact on CD4 T cell infiltration (**Figure 4.4 g**), it significantly reduced the amount of regulator T cells (Tregs, FoxP3^{+}CD4^{+}) in tumor (**Figure 4.4 h**). CTL/Treg ratio increased in animals administered with ION-laden macrophages (**Figure 4.4 i**).

We also harvested spleen from all treatment groups and analyzed response of splenocytes ex vivo when exposed to OVA. Relative to the irradiation alone group, we found increased populations of both CD4^{+} (**Figure 4.4 j**) and CD8^{+} T (**Figure 4.4 k**) cells in animals treated with irradiation plus ION-macrophages. In particular, IFNγ^{+} CTLs were drastically increased (**Figure 4.4 l**), indicating boosted antigen-specific immune response. Overall, our animals showed that ION-laden macrophages can transform the tumor microenvironment to boost tumor-specific cellular immunity.

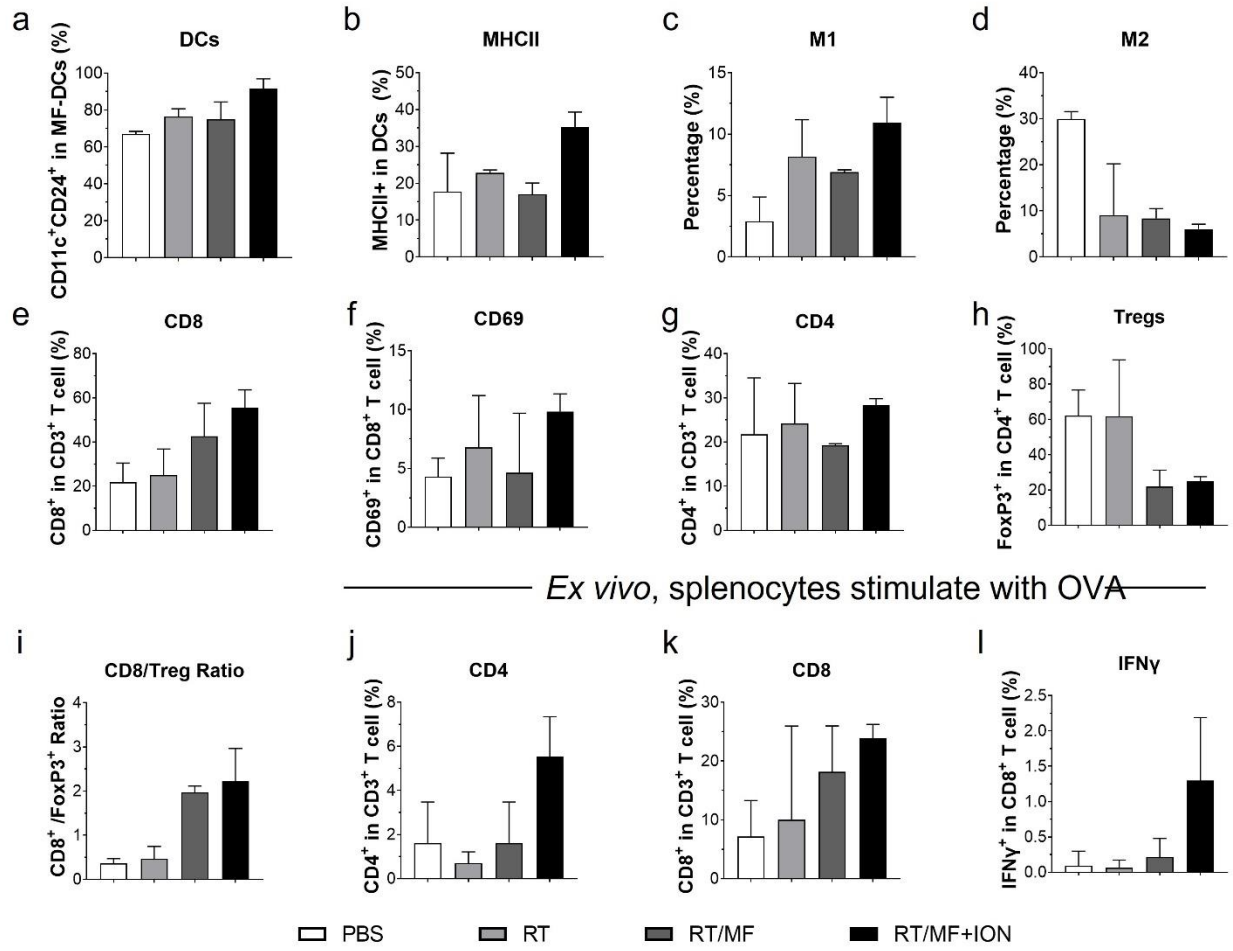

Figure 4.4. Impact of ION-laden macrophages on TME *in vivo*. a, b) DCs profiling on day 7. Markers including MHCII, CD11c were analyzed by flow cytometry. c, d) M1 and M2 macrophage population was evaluated. T cells profiling. Markers including e) CD8, f) CD69, g) CD4, and h) Foxp3 were analyzed by flow cytometry. i) $CD8^+$ to Treg ratio. Ex vivo splenocytes stimulated by OVA. Markers including j) CD4, k) CD8, l) IFN-γ were evaluated. *, $p < 0.05$; **, $p < 0.01$; ***, $p < 0.001$; ****, $p < 0.0001$.

In vivo animal study

We then evaluated the potential therapeutic effect of ION-loaded macrophages. We tested this in CT26 tumor-bearing Balb/c mice. To trigger antigen release, tumors received 5 Gy irradiation prior to i.t. administration of ION-loaded macrophages. Relative to irradiation alone or irradiation plus untreated macrophages, irradiation plus ION-loaded macrophages significantly improved tumor suppression (**Figure 4.5 e**). Meanwhile, treatment with AON (**Figure 4.5 f**) or ZON (**Figure 4.5 g**) showed little therapy benefits.

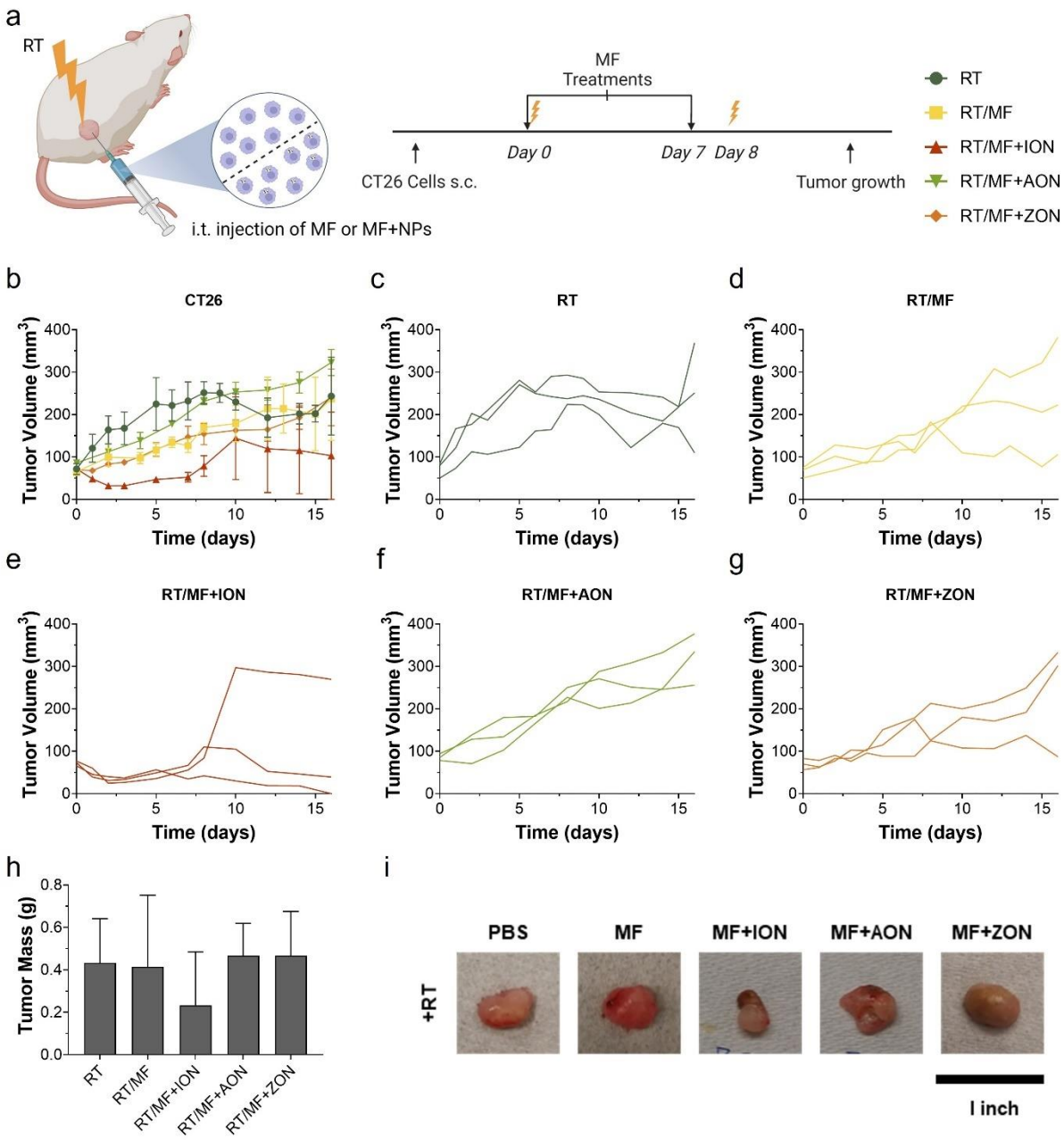

Figure 4.5. CT26 tumor model with RT. a) Animal study experimental design and treatment groups. b) CT26 tumor growth curve. c-g) Individual tumor growth curve. h) Tumor mass. i) Representative images of tumors.

We next examined whether directly injecting ION into tumors can also improve tumor suppression. We postulate that i.t. administered ION can be taken up by macrophages, which

similarly transforms TME (**Figure 4.6 a**). We tested in this B16 tumor bearing C57BL/6 mice. Indeed, we found that i.t. administered ION are largely accumulated in macrophages. When evaluating efficacy, we applied irradiation to tumors one hour prior to ION injection and gave a total of treatments at a two-day interval. While IONs alone showed marginal tumor suppression (TGI of 31% on Day 25) IONs plus irradiation significantly inhibited tumor growth (TGI 95% on Day 25) (**Figure 4.6 b**). Relative to RT alone, IONs plus irradiation showed improved tumor inhibition and survival (**Figure 4.6 c**). No obvious body weight loss was observed in all groups (**Figure 4.6 d**).

After animal euthanasia, we harvested tumors and major organs for histopathology analysis. Tumors from the ION plus irradiation group showed significantly reduced cell density (**Figure 4.6 f**) and decreased Ki-67 staining (**Figure 4.6 g**), confirming improved tumor suppression. Meanwhile, H&E staining found no signs of toxicity in major organs, suggesting minimal systemic toxicity (**Figure 4.7**).

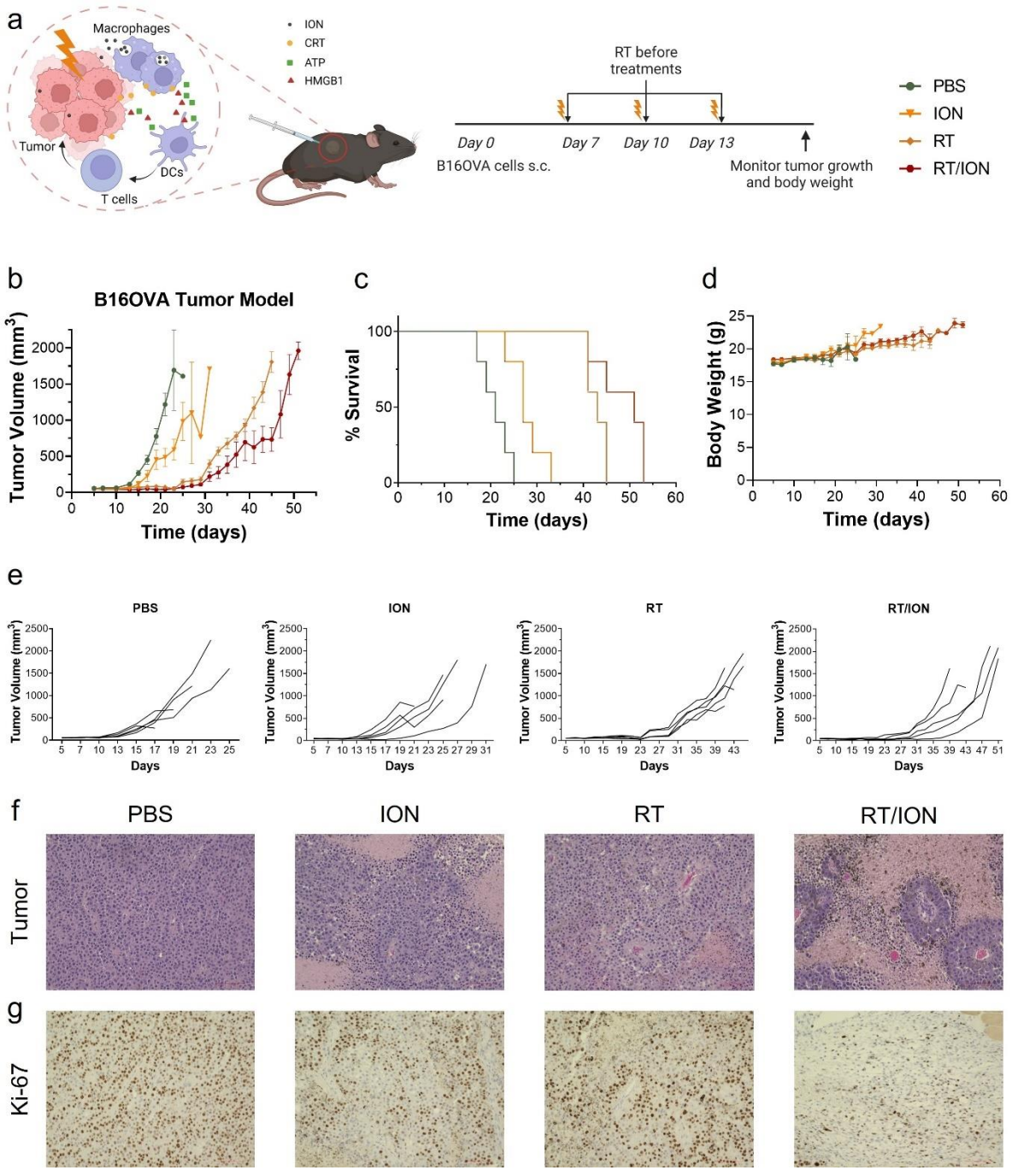

Figure 4.6. B16OVA tumor model. a) Animal study experimental design and treatment groups. b) B16OVA tumor growth curve. c) Mice survival curve. d) Mice body weight. e) Individual tumor growth curve. f) H&E staining of tumors. g) Ki-67 staining of tumors.

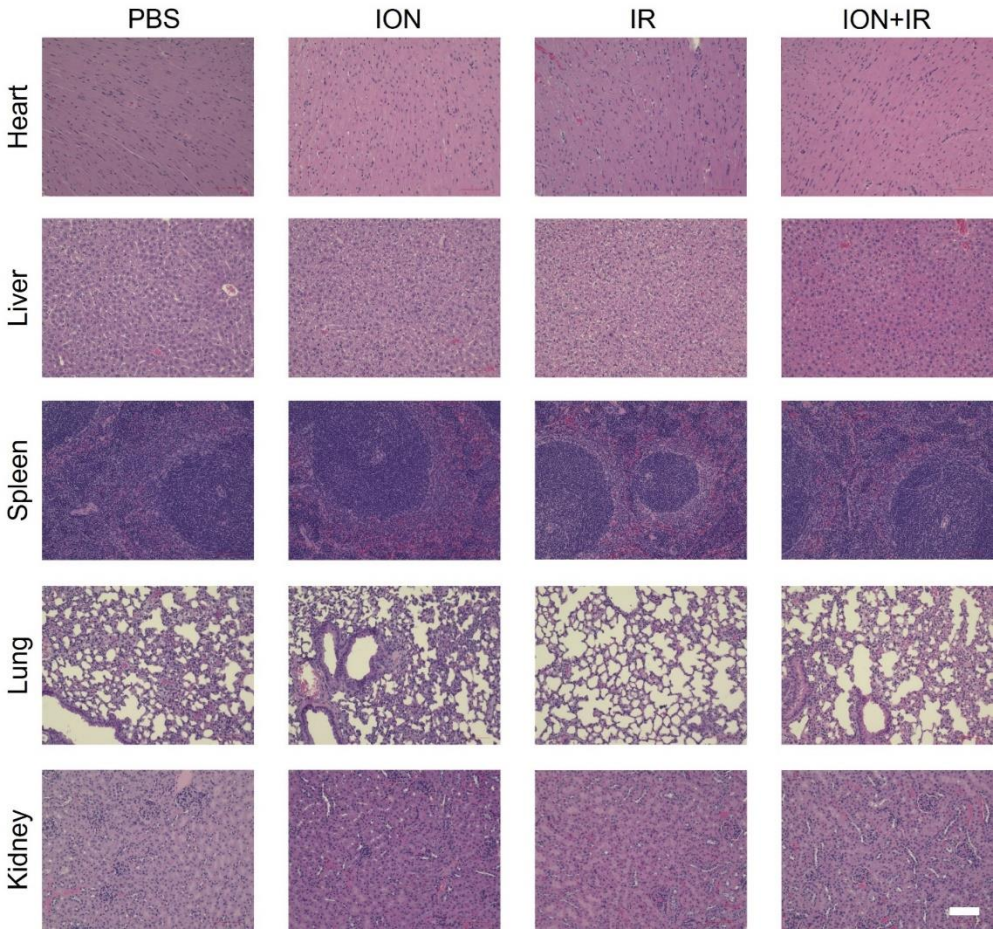

Figure 4.7. H&E staining of organs.

Summary

In this study, we compared three inorganic nanoparticles in their ability to induce secretion of ATP and HMGB1 from macrophages. We found that all three nanoparticles can promote ATP and HMGB1 secretion. However, when tested *in vivo*, only ION-loaded macrophages significantly improved IR-induced tumor suppression. The exact reason remains elusive and could be multifold. One is that ION promoted M1 polarization of macrophages whereas ZON and AON promoted both M1 and M2 polarization. The other is that ION were able to stimulate ATP and HMGB1 secretion at a relatively wider concentration range. As a

comparison, AON and ZON seem to work most effectively at a particular concentration. ZON in particular, showed relatively high level of toxicity, which may complicate or negatively affect their ability to modulate macrophage functions.

Others have studied how iron oxide nanoparticles interact macrophages and influence their functions. The focus is largely on cytokines and chemokines. Here we showed that ATP and HMGB1 are secreted from macrophages over incubation with ION, and the DAMPs can engage with DCs to boost immunity. It is worth pointing that in previous studies, ION were added at different concentrations, which may affect the secretion profiles.

In the current study, we showed that such the ATP/HMGB1 induction effects can be exploited to improve radiotherapy. It is postulated that the same effects may be used to improve chemotherapy, especially for drugs that are unable to incur ICD on their own (**Figure S4.2**). Note that nanoparticle-loaded macrophages alone were not efficient at tumor suppression. The treatment benefits were only observed when the macrophages were used in combination with IR. It is also possible that IR is needed to induce surface exposure of CRT, which is another essential hallmark of ICD. DAMPs released from macrophages can supplement but not replace those released from dying cancer cells to incur or amplify immune responses.

We also showed that administering ION rather than ION-loaded macrophages can enhance radiotherapy. Others have reported on the radiosensitizing effects of ION. These were attributed to the high-Z effects of ION or their ability to induce ferroptosis. In our studies, we found that the majority of i.t. injected ION were accumulated in macrophages rather than cancer cells, and the nanoparticles were not effective at killing cancer cells at the tested dose. We administered ION after IR rather than before IR, so high-Z effects also played a minimal role. Hence the results supported the benefits of macrophage modulatory effects in treatment. More

studied are warranted to examine whether similar effects play a role in other inorganic nanoparticle based radiosensitizers.

REFERENCE

[1] S. Baldochi and I. Ranieri, "Alkali halide crystals: growth," *Encyclopedia of Materials: Science and Technology*, pp. 74-78, 2001.

[2] V. Vaněček, K. Děcká, E. Mihóková, V. Čuba, R. Král, and M. Nikl, "Advanced Halide Scintillators: From the Bulk to Nano," *Advanced Photonics Research,* vol. 3, no. 8, p. 2200011, 2022.

[3] B. Schmitt, M. Fuchs, E. Hell, W. Knüpfer, P. Hackenschmied, and A. Winnacker, "Structured alkali halides for medical applications," *Nuclear Instruments and Methods in Physics Research Section B: Beam Interactions with Materials and Atoms,* vol. 191, no. 1-4, pp. 800-804, 2002.

[4] N. Schiefermeier-Mach *et al.*, "Electrolyte intake and major food sources of sodium, potassium, calcium and magnesium among a population in Western Austria," *Nutrients,* vol. 12, no. 7, p. 1956, 2020.

[5] J. Terry, "The major electrolytes: sodium, potassium, and chloride," *Journal of Infusion Nursing,* vol. 17, no. 5, pp. 240-247, 1994.

[6] X. Huang and L. Y. Jan, "Targeting potassium channels in cancer," *Journal of Cell Biology,* vol. 206, no. 2, pp. 151-162, 2014.

[7] S. P. Yu, "Regulation and critical role of potassium homeostasis in apoptosis," *Progress in neurobiology,* vol. 70, no. 4, pp. 363-386, 2003.

[8] W. Jiang *et al.*, "NaCl nanoparticles as a cancer therapeutic," *Advanced Materials,* vol. 31, no. 46, p. 1904058, 2019.

[9] H. Wulff, N. A. Castle, and L. A. Pardo, "Voltage-gated potassium channels as therapeutic targets," *Nature reviews Drug discovery,* vol. 8, no. 12, pp. 982-1001, 2009.

[10] L. A. Pardo and W. Stühmer, "The roles of K+ channels in cancer," *Nature Reviews Cancer,* vol. 14, no. 1, pp. 39-48, 2014.

[11] B. L. Cline *et al.*, "Potassium Iodide Nanoparticles Enhance Radiotherapy against Breast Cancer by Exploiting the Sodium-Iodide Symporter," *ACS nano,* vol. 15, no. 11, pp. 17401-17411, 2021.

[12] S. Mazumder, R. Dey, M. Mitra, S. Mukherjee, and G. Das, "Biofunctionalized quantum dots in biology and medicine," *Journal of Nanomaterials,* vol. 2009, 2009.

[13] U. M. Cytlak, D. P. Dyer, J. Honeychurch, K. J. Williams, M. A. Travis, and T. M. Illidge, "Immunomodulation by radiotherapy in tumour control and normal tissue toxicity," *Nature Reviews Immunology,* vol. 22, no. 2, pp. 124-138, 2022.

[14] J. F. Hainfeld, F. A. Dilmanian, D. N. Slatkin, and H. M. Smilowitz, "Radiotherapy enhancement with gold nanoparticles," *Journal of pharmacy and pharmacology,* vol. 60, no. 8, pp. 977-985, 2008.

[15] S. S. Ahmad, S. Duke, R. Jena, M. V. Williams, and N. G. Burnet, "Advances in radiotherapy," *Bmj,* vol. 345, 2012.

[16] N. Goswami, Z. Luo, X. Yuan, D. T. Leong, and J. Xie, "Engineering gold-based radiosensitizers for cancer radiotherapy," *Materials Horizons,* vol. 4, no. 5, pp. 817-831, 2017.

[17] Z. Zhu *et al.*, "Redox-sensitive iodinated polymersomes carrying histone deacetylase inhibitor as a dual-functional nano-radiosensitizer for enhanced radiotherapy of breast cancer," *Drug Delivery,* vol. 28, no. 1, pp. 2301-2309, 2021.

[18] J. F. Hainfeld, S. M. Ridwan, Y. Stanishevskiy, R. Panchal, D. N. Slatkin, and H. M. Smilowitz, "Iodine nanoparticles enhance radiotherapy of intracerebral human glioma in mice and increase efficacy of chemotherapy," *Scientific Reports,* vol. 9, no. 1, p. 4505, 2019.

[19] C. Portulano, M. Paroder-Belenitsky, and N. Carrasco, "The Na+/I− symporter (NIS): mechanism and medical impact," *Endocrine reviews,* vol. 35, no. 1, pp. 106-149, 2014.

[20] M. G. Kelkar, K. Senthilkumar, S. Jadhav, S. Gupta, B.-C. Ahn, and A. De, "Enhancement of human sodium iodide symporter gene therapy for breast cancer by HDAC inhibitor mediated transcriptional modulation," *Scientific reports,* vol. 6, no. 1, p. 19341, 2016.

[21] F. Maddalena *et al.*, "Inorganic, organic, and perovskite halides with nanotechnology for high–light yield X-and γ-ray scintillators," *Crystals,* vol. 9, no. 2, p. 88, 2019.

[22] T. J. Hajagos, C. Liu, N. J. Cherepy, and Q. Pei, "High-Z sensitized plastic scintillators: a review," *Advanced Materials,* vol. 30, no. 27, p. 1706956, 2018.

[23] D. S. McGregor, "Materials for gamma-ray spectrometers: Inorganic scintillators," *Annual Review of Materials Research,* vol. 48, pp. 245-277, 2018.

[24] H. Wei and J. Huang, "Halide lead perovskites for ionizing radiation detection," *Nature communications,* vol. 10, no. 1, p. 1066, 2019.

[25] S. Min, H. Kang, B. Seo, J. Cheong, C. Roh, and S. Hong, "A Review of Nanomaterial Based Scintillators," *Energies,* vol. 14, no. 22, p. 7701, 2021.

[26] F. Jiang *et al.*, "Radiodynamic therapy with CsI (na)@ MgO nanoparticles and 5-aminolevulinic acid," *Journal of Nanobiotechnology,* vol. 20, no. 1, pp. 1-15, 2022.

[27] S. Clement *et al.*, "Mechanisms for tuning engineered nanomaterials to enhance radiation therapy of cancer," *Advanced Science,* vol. 7, no. 24, p. 2003584, 2020.

[28] X. Yang *et al.*, "Nanomaterials for radiotherapeutics-based multimodal synergistic cancer therapy," *Nano Research,* vol. 13, pp. 2579-2594, 2020.

[29] A. F. Carvalho, J. Firth, and E. Vieta, "Bipolar disorder," *New England Journal of Medicine,* vol. 383, no. 1, pp. 58-66, 2020.

[30] E. Y. Plotnikov *et al.*, "Lithium salts—Simple but magic," *Biochemistry (Moscow),* vol. 79, pp. 740-749, 2014.

[31] E. Beurel and R. Jope, "Inflammation and lithium: clues to mechanisms contributing to suicide-linked traits," *Translational psychiatry,* vol. 4, no. 12, pp. e488-e488, 2014.

[32] M. E. Snitow, R. S. Bhansali, and P. S. Klein, "Lithium and therapeutic targeting of GSK-3," *Cells,* vol. 10, no. 2, p. 255, 2021.

[33] A. Nassar and A. N. Azab, "Effects of lithium on inflammation," *ACS chemical neuroscience,* vol. 5, no. 6, pp. 451-458, 2014.

[34] Y.-T. Gu *et al.*, "Research progress on osteoarthritis treatment mechanisms," *Biomedicine & Pharmacotherapy,* vol. 93, pp. 1246-1252, 2017.

[35] B. Abramoff and F. E. Caldera, "Osteoarthritis: pathology, diagnosis, and treatment options," *Medical Clinics,* vol. 104, no. 2, pp. 293-311, 2020.

[36] T. Minashima, Y. Zhang, Y. Lee, and T. Kirsch, "Lithium protects against cartilage degradation in osteoarthritis," *Arthritis & rheumatology,* vol. 66, no. 5, pp. 1228-1236, 2014.

[37] C. H. Evans, V. B. Kraus, and L. A. Setton, "Progress in intra-articular therapy," *Nature Reviews Rheumatology,* vol. 10, no. 1, pp. 11-22, 2014.

[38] T. Todd *et al.*, "LiF@ SiO 2 nanocapsules for controlled lithium release and osteoarthritis treatment," *Nano Research,* vol. 11, pp. 5751-5760, 2018.

[39] G.-Z. Jin, "Current nanoparticle-based technologies for osteoarthritis therapy," *Nanomaterials,* vol. 10, no. 12, p. 2368, 2020.

[40] R. L. Siegel, K. D. Miller, H. E. Fuchs, and A. Jemal, "Cancer statistics, 2022," *CA: a cancer journal for clinicians,* vol. 72, no. 1, pp. 7-33, 2022.

[41] O. Sanli *et al.*, "Bladder cancer," *Nature reviews Disease primers,* vol. 3, no. 1, pp. 1-19, 2017.

[42] Z. Shen, T. Shen, M. G. Wientjes, M. A. O'Donnell, and J. L.-S. Au, "Intravesical treatments of bladder cancer," *Pharmaceutical research,* vol. 25, pp. 1500-1510, 2008.

[43] J.-W. Hsu and M. R. King, "Applications of nanotechnology in bladder cancer therapy," *Journal of Healthcare Engineering,* vol. 3, no. 4, pp. 535-550, 2012.

[44] E. P. Goldberg, A. R. Hadba, B. A. Almond, and J. S. Marotta, "Intratumoral cancer chemotherapy and immunotherapy: opportunities for nonsystemic preoperative drug delivery," *Journal of Pharmacy and Pharmacology,* vol. 54, no. 2, pp. 159-180, 2002.

[45] U. K. Udensi and P. B. Tchounwou, "Potassium homeostasis, oxidative stress, and human disease," *International journal of clinical and experimental physiology,* vol. 4, no. 3, p. 111, 2017.

[46] S. P. Yu, L. M. Canzoniero, and D. W. Choi, "Ion homeostasis and apoptosis," *Current opinion in cell biology,* vol. 13, no. 4, pp. 405-411, 2001.

[47] J. I. G. Solari *et al.*, "Damage-associated molecular patterns (DAMPs) related to immunogenic cell death are differentially triggered by clinically relevant

chemotherapeutics in lung adenocarcinoma cells," *BMC cancer,* vol. 20, no. 1, pp. 1-14, 2020.

[48] H. Inoue and K. Tani, "Multimodal immunogenic cancer cell death as a consequence of anticancer cytotoxic treatments," *Cell Death & Differentiation,* vol. 21, no. 1, pp. 39-49, 2014.

[49] Y. Fan, R. Kuai, Y. Xu, L. J. Ochyl, D. J. Irvine, and J. J. Moon, "Immunogenic cell death amplified by co-localized adjuvant delivery for cancer immunotherapy," *Nano letters,* vol. 17, no. 12, pp. 7387-7393, 2017.

[50] R. L. Siegel, K. D. Miller, H. E. Fuchs, and A. Jemal, "Cancer statistics, 2021," *Ca Cancer J Clin,* vol. 71, no. 1, pp. 7-33, 2021.

[51] D. E. Johnson, B. Burtness, C. R. Leemans, V. W. Y. Lui, J. E. Bauman, and J. R. Grandis, "Author Correction: Head and neck squamous cell carcinoma (Nature Reviews Disease Primers,(2020), 6, 1,(92), 10.1038/s41572-020-00224-3)," *Nature Reviews Disease Primers,* vol. 9, no. 1, p. 4, 2023.

[52] L. Q. Chow, "Head and neck cancer," *New England Journal of Medicine,* vol. 382, no. 1, pp. 60-72, 2020.

[53] S. Marur and A. A. Forastiere, "Head and neck squamous cell carcinoma: update on epidemiology, diagnosis, and treatment," in *Mayo Clinic Proceedings,* 2016, vol. 91, no. 3: Elsevier, pp. 386-396.

[54] K. Bjordal, S. Kaasa, and A. Mastekaasa, "Quality of life in patients treated for head and neck cancer: a follow-up study 7 to 11 years after radiotherapy," *International Journal of Radiation Oncology* Biology* Physics,* vol. 28, no. 4, pp. 847-856, 1994.

[55] E. Hammerlid and C. Taft, "Health-related quality of life in long-term head and neck cancer survivors: a comparison with general population norms," *British journal of cancer,* vol. 84, no. 2, pp. 149-156, 2001.

[56] S. Furness *et al.*, "Interventions for the treatment of oral cavity and oropharyngeal cancer: chemotherapy," *Cochrane Database of Systematic Reviews,* no. 4, 2011.

[57] R. M. Logan, "Advances in understanding of toxicities of treatment for head and neck cancer," *Oral oncology,* vol. 45, no. 10, pp. 844-848, 2009.

[58] P.-J. Lou, L. Jones, and C. Hopper, "Clinical outcomes of photodynamic therapy for head-and-neck cancer," *Technology in cancer research & treatment,* vol. 2, no. 4, pp. 311-317, 2003.

[59] H. Shibata, S. Saito, and R. Uppaluri, "Immunotherapy for head and neck cancer: a paradigm shift from induction chemotherapy to neoadjuvant immunotherapy," *Frontiers in Oncology,* vol. 11, p. 727433, 2021.

[60] J. Shen *et al.*, "Assessment of folate receptor alpha and beta expression in selection of lung and pancreatic cancer patients for receptor targeted therapies," *Oncotarget,* vol. 9, no. 4, p. 4485, 2018.

[61] N. F. Saba *et al.*, "Examining expression of folate receptor in squamous cell carcinoma of the head and neck as a target for a novel nanotherapeutic drug," *Head & neck,* vol. 31, no. 4, pp. 475-481, 2009.

[62] M. Scaranti, E. Cojocaru, S. Banerjee, and U. Banerji, "Exploiting the folate receptor α in oncology," *Nature reviews clinical oncology,* vol. 17, no. 6, pp. 349-359, 2020.

[63] M. Xie *et al.,* "Expression of folate receptors in nasopharyngeal and laryngeal carcinoma and folate receptor-mediated endocytosis by molecular targeted nanomedicine," *International journal of nanomedicine,* pp. 2443-2451, 2013.

[64] A. Omelchenko *et al.,* "Dynamin and reverse-mode sodium calcium exchanger blockade confers neuroprotection from diffuse axonal injury," *Cell death & disease,* vol. 10, no. 10, p. 727, 2019.

[65] D. Criddle *et al.,* "Calcium signalling and pancreatic cell death: apoptosis or necrosis?," *Cell Death & Differentiation,* vol. 14, no. 7, pp. 1285-1294, 2007.

[66] Y. Chen, M. Azad, and S. Gibson, "Superoxide is the major reactive oxygen species regulating autophagy," *Cell Death & Differentiation,* vol. 16, no. 7, pp. 1040-1052, 2009.

[67] D. H. Kwon *et al.,* "Protective effect of glutathione against oxidative stress-induced cytotoxicity in RAW 264.7 macrophages through activating the nuclear factor erythroid 2-related factor-2/heme oxygenase-1 pathway," *Antioxidants,* vol. 8, no. 4, p. 82, 2019.

[68] J. Armstrong *et al.,* "Role of glutathione depletion and reactive oxygen species generation in apoptotic signaling in a human B lymphoma cell line," *Cell Death & Differentiation,* vol. 9, no. 3, pp. 252-263, 2002.

[69] G. Pizzino *et al.,* "Oxidative stress: harms and benefits for human health," *Oxidative medicine and cellular longevity,* vol. 2017, 2017.

[70] D. V. Krysko, A. D. Garg, A. Kaczmarek, O. Krysko, P. Agostinis, and P. Vandenabeele, "Immunogenic cell death and DAMPs in cancer therapy," *Nature Reviews Cancer,* vol. 12, no. 12, pp. 860-875, 2012.

[71] L. Galluzzi, A. Buqué, O. Kepp, L. Zitvogel, and G. Kroemer, "Immunogenic cell death in cancer and infectious disease," *Nature Reviews Immunology,* vol. 17, no. 2, pp. 97-111, 2017.

[72] S. Di Blasio *et al.*, "Human CD1c+ DCs are critical cellular mediators of immune responses induced by immunogenic cell death," *Oncoimmunology,* vol. 5, no. 8, p. e1192739, 2016.

[73] J. Zhou, G. Wang, Y. Chen, H. Wang, Y. Hua, and Z. Cai, "Immunogenic cell death in cancer therapy: Present and emerging inducers," *Journal of cellular and molecular medicine,* vol. 23, no. 8, pp. 4854-4865, 2019.

[74] Z. Huang, Y. Wang, D. Yao, J. Wu, Y. Hu, and A. Yuan, "Nanoscale coordination polymers induce immunogenic cell death by amplifying radiation therapy mediated oxidative stress," *Nature Communications,* vol. 12, no. 1, p. 145, 2021.

[75] C. He *et al.*, "Core-shell nanoscale coordination polymers combine chemotherapy and photodynamic therapy to potentiate checkpoint blockade cancer immunotherapy," *Nature communications,* vol. 7, no. 1, p. 12499, 2016.

[76] E. Vacchelli *et al.*, "Trial Watch: Toll-like receptor agonists for cancer therapy," *Oncoimmunology,* vol. 2, no. 8, p. e25238, 2013.

[77] T. A. Wynn, A. Chawla, and J. W. Pollard, "Macrophage biology in development, homeostasis and disease," *Nature,* vol. 496, no. 7446, pp. 445-455, 2013.

[78] F. Corsi, F. Carotenuto, P. Di Nardo, and L. Teodori, "Harnessing inorganic nanoparticles to direct macrophage polarization for skeletal muscle regeneration," *Nanomaterials,* vol. 10, no. 10, p. 1963, 2020.

[79] M. Saeed, J. Gao, Y. Shi, T. Lammers, and H. Yu, "Engineering nanoparticles to reprogram the tumor immune microenvironment for improved cancer immunotherapy," *Theranostics,* vol. 9, no. 26, p. 7981, 2019.

[80] S. Zanganeh *et al.*, "Iron oxide nanoparticles inhibit tumour growth by inducing pro-inflammatory macrophage polarization in tumour tissues," *Nature nanotechnology,* vol. 11, no. 11, pp. 986-994, 2016.

[81] X. Cui *et al.*, "Carbon nanomaterials stimulate HMGB1 release from macrophages and induce cell migration and invasion," *Toxicological Sciences,* vol. 172, no. 2, pp. 398-410, 2019.

[82] J. Liu, X. Geng, J. Hou, and G. Wu, "New insights into M1/M2 macrophages: key modulators in cancer progression," *Cancer Cell International,* vol. 21, no. 1, pp. 1-7, 2021.

[83] F. R. Bertani *et al.*, "Classification of M1/M2-polarized human macrophages by label-free hyperspectral reflectance confocal microscopy and multivariate analysis," *Scientific reports,* vol. 7, no. 1, p. 8965, 2017.

[84] Q. Xue, Y. Yan, R. Zhang, and H. Xiong, "Regulation of iNOS on immune cells and its role in diseases," *International journal of molecular sciences,* vol. 19, no. 12, p. 3805, 2018.

[85] D. Sun *et al.*, "CD86+/CD206+ tumor-associated macrophages predict prognosis of patients with intrahepatic cholangiocarcinoma," *PeerJ,* vol. 8, p. e8458, 2020.

[86] C. Yunna, H. Mengru, W. Lei, and C. Weidong, "Macrophage M1/M2 polarization," *European journal of pharmacology,* vol. 877, p. 173090, 2020.

APPENDICES

A Supporting information for Chapter 2

Synthesis of sodium chloride nanoparticles (SCNPs). Typically, at room temperature, 213 mg of sodium acetate (anhydrous, 99%, Sigma-Aldrich) was first completely dissolved in 65 mL of ethanol (PURE 200 PROOF, KOPTEC). 20 mL of oleylamine (70%, Sigma-Aldrich), which serves as a surfactant, and 10 mL of hexane (99.9%, Fisher) were then added to the mixture. Using magnetic stirring, 8 mL of hexane containing 160 μL of acetyl chloride (99.0%, Sigma-Aldrich) was added dropwise over 1.5 minutes using a 1 mL pipette. After the last drop, the SCNPs were immediately collected by centrifugation at 10000 rpm for 3 min and washed with 20 mL of hexanes to remove unreacted precursors. Finally, the nanoparticles were redispersed in hexanes, transferred to two glass vials, and dried by rotary evaporation (Buchi R II Rotavapor). The SCNPs were sealed with parafilm and carefully stored in a desiccator to avoid humidity.

Phospholipid-coated sodium chloride nanoparticles (PSCNPs). 40 mg of the above-synthesized SCNPs were redispersed in 2 mL isopropanol and sonicated for 2 min, then 400 μL phospholipid solution (5 mg/mL) DSPE-PEG (2000) Amine, (1,2-distearoyl-sn-glycero-3-phosphoethanolamine-N-[amino(polyethylene glycol)-2000] (ammonium salt), Avanti) was added and the mixture was sonicated for another 30 s. The final product was dried by rotary evaporation. For rhodamine B-labeled PSCNPs (RB-PSCNPs), 16:0 Liss Rhod PE (1,2-

dipalmitoyl-sn-glycero-3-phosphoethanolamine-N-(lissamine-rhodamine B sulfonyl) (ammonium salt), Avanti) was added during sonication, and other steps remained the same.

Characterizations of NPs. Transmission electron microscopy (TEM) images were captured on a STEM - Hitachi SU9000EA which operated at 30 kV, 1 μA. Energy dispersive X-ray spectra (EDS) elemental mapping images were obtained using the TEM-compatible Oxford EDS system. The crystallinity of NPs was confirmed using Bruker D8-Advance X-ray diffraction (XRD) diffractometer with Cu Kα radiation (λ = 1.5418 Å). The hydrodynamic sizes and zeta potentials of the nanoparticles were determined using a Malvern Zetasizer Nano ZS system. Fourier transform infrared (FT-IR) spectra were recorded using a Thermo Scientific™ Nicolet™ FT-IR spectrometer equipped with OMNIC spectroscopy software.

Stability and release experiments. PSCNPs were dispersed in 1 mL of D.I. water. At different time points (5 min, 1, 6, 24 h), took 10 μL to prepare the TEM sample and take the TEM images. As for the release study, PSCNPs were dispersed in 400 μL Na^+-free ammonium acetate buffers (pH=5 or pH=7) and added into a dialysis unit (Slide-A-Lyzer® MINI Dialysis Device, MWCO = 3500). Samples were kept in tubes containing 4.5 mL ammonium acetate buffers on an incubating shaker at 37 ℃. At different time points (10 min, 0.5, 1, 2, 4, 6, 8, 12, 24 h), took 400 μL solution from lower tubes to measure the concentration of Na^+ (LAQUAtwin Sodium Ion Meter, HORIBA).

Cell culture. BBN963 (murine bladder carcinoma) and NIH/3T3 (embryo fibroblast) were cultured in DMEM (ATCC, 30-2002). UPPL-1541, MB49 (murine bladder carcinoma),

UMUC2, T-24 (human bladder carcinoma), and RAW 264.7 (murine macrophage) were cultured in RPMI-1640 (Corning, 10-040-CV). The complete medium was supplemented with 10% fetal bovine serum (FBS, Atlanta Biologicals, S11150) and 1% penicillin/streptomycin (Gibco, 15140-122). Human primary prostate epithelial cells (HPrECs, ATCC, PCS-440-010) were cultivated in prostate epithelial cell basal media (ATCC, PCS-420-032) supplemented with prostate epithelial cell growth kit (ATCC, PCS-420-042). Primary bladder epithelial cells (BdECs, ATCC, PCS-420-010) were maintained in bladder epithelial cell basal medium (ATCC, PCS-420-032) supplemented with bladder epithelial growth kit (ATCC, PCS-420-042). Ki1970 (primary bladder epithelial cells, a gift from UNC) was cultured in complete DMEM with additional components. In particular, bone-marrow-derived dendritic cells were generated from the femurs and tibias of 6-week-old mice and cultured ex vivo in complete RPMI supplemented with rmGM-CSF (PeproTech). All cells were maintained in a humidified, 5% CO2, 37℃ atmosphere (HERA cell 150, Thermo Scientific).

Cytotoxicity study by MTT assay. Cells were seeded into a 96-well transparent plate (Corning, 3599) at a density of 8000 cells per well and incubated overnight. The cells with PSCNPs were dispersed in an FBS-free medium for two hours, then FBS was supplemented, and cells were maintained for another 22 hours. MTT (3-(4,5-dimethylthiazol-2-yl)-2,5-diphenyl tetrazolium bromide, Sigma) was introduced to form purple formazan crystals in viable cells. The absorbance of MTT in dimethyl sulfoxide (DMSO, 99%, Thermo Scientific) solution was measured by a microplate reader at 570 nm (Synergy Mx, BioTeK).

Cell internalization study using flow cytometry. BBN963 cells were seeded in 6-well plates (Corning, 3516) at a density of 5×10^5 cells per well and incubated overnight. To investigate the cellular uptake pathway, cells were treated with four chemical endocytosis inhibitors including sodium azide (50 mM, Sigma, S2002), dynasore (80 μM, Abcam, ab120192), nystatin (25 μM, Sigma, N6261), and chlorpromazine (100 μM, Sigma, C8138) for 1 hour prior to the addition of RB-PSCNPs. The cells were then incubated with RB-PSCNPs for an additional 4 hours. Cells were collected with cell lifters, washed once with PBS, stained with DAPI (Thermo Fisher Scientific), and fixed with a 1:1 mixture of IC fixation buffer (eBioscience, 00-8222-49)/staining buffer (eBioscience, 00-4222-57) for 30 minutes. The cells were then resuspended in the staining buffer and transferred to a 96-well U-shaped plate. To quench fluorescence from nanoparticles not specifically bound to the cell membrane, trypan blue solution (0.4%, Gibco™) was added at a final concentration of 20 μg/mL. Signals from intercellular RB-SCNPs were detected by flow cytometry (NovoCyte Quanteon Flow Cytometer Systems 4 Lasers) and analyzed to obtain mean fluorescence intensity (MFI) results.

The intracellular concentration of Na+, Cl-, and Ca^{2+}. BBN963 cells were seeded in a black 96-well plate (Costar, 3610) at a density of 8000 cells per well and incubated overnight. Prior to the addition of PSCNPs, the cells were loaded with 10 μM SBFI-AM (sodium binding benzofuran isophthalate acetoxymethyl ester, cell-permeant, Setareh Biotech, 6212), 10 mM MQAE (1-(ethoxycarbonylmethyl)-6-methoxyquinolinium bromide, cell-permeant, Setareh Biotech, 6270), or 10 μM Fluo-3 AM (Invitrogen™, F1241) in serum-free medium (serum may contain esterase activity) containing 0. 02% Pluronic® F-127 (Sigma, P2443) for half an hour. After Na^+, Cl^- and Ca^{2+} staining, cells were treated with PSCNPs and the fluorescence signal was

recorded at different time points (0, 0.5, 1, 2, 4, 6 h) using a microplate reader (Synergy Mx, BioTeK). Ex339/Em565 for Na^+, Ex350/Em460 for Cl^-, Ex506/Em526 for Ca^{2+}. PBS and NaCl salt were used as controls.

LDH assay. BBN963 cells were seeded into a 96-well plate at a density of 8000 cells per well and incubated overnight. The cells were further incubated with PSCNPs for another 24 h. LDH contents in the supernatant were measured by LDH Assay Kit-WST (Dojindo, CK12-20). If an inhibition study was performed, the cells were pre-incubated with different inhibitors including dynamin inhibitor dynasore (Abcam, ab120192) and endocytosis inhibitor chlorpromazine (Sigma, C8138), ferroptosis inhibitor ferrostatin-1 (Cayman, 17729), apoptosis inhibitor Z-VAD-fmk (Selleckchem, S7023), autophagy inhibitor 3-Methyladenine (3-MA, Selleckchem, S2767), necrosis inhibitor glycine (Sigma, G8898), general NCX inhibitor diltiazem (TGI, D3662) and mitochondrial NCX inhibitor CGP37157 (Cayman, 15611-10) for 1 h, then incubated with PSCNPs.

Intracellular sodium concentration. A panel of cell lines, including BBN963, UPPL-1541, UMUC2, T-24, MB49, RAW264.7, BMDCs, HPrECs, BdECs, Ki1970, NIH/3T3, were cultured in 100 mm petri dishes. Once reached 90% confluency, the cells were collected and washed with 5 mL 10 mM Na^+-free HEPES buffer (Sigma, H0887) two times followed by cell numbers counting by using a hemocytometer. Cells were resuspended in 0.5 mL D.I. water and lysed by probe sonication. Sodium contents were measured by a sodium ion meter (HORIBA LAQUAtwin Na-11). The results were normalized to cell numbers (pg/cell).

ATP releasing from dying cancer cells. ATPliteTM 1step (PerkinElmer, 6016731) luminescence assay system based on firefly luciferase was used to determine the extracellular ATP contents. Cells were seeded into a 96-well transparent plate (Corning, 3599) at a density of 8000 cells per well and incubated overnight. Cells were then treated with PSCNPs in an IC50 concentration for 2 hours. Supernatants were transferred to a 96-well black plate (Costar, 3610) followed by the addition of an equivalent volume of substrate solution. Luminescence signals were measured on a microplate reader (Synergy Mx, BioTeK).

CRT expression from dying cancer cells. Cells were seeded into 6-well plates (Corning, 3516) at a density of 5×10^5 cells per well. After overnight incubation, treated the cells with PSCNPs for 24 hours to induce ICD. The cells are collected with cell lifters, washed with PBS, stained with DAPI and Alexa Fluor® 647-conjugated anti-CRT antibody (ab196159, Abcam) for 30 min at 4 ℃, and sequentially fixed. The flow cytometer (NovoCyte Quanteon Flow Cytometer Systems 4 Lasers) was employed to assess the CRT signal. The data are presented in mean fluorescence intensity (MFI) compared to the PBS control.

HMGB1 secretion from dying cancer cells. BBN963 and MB49 Cells were seeded into 24-well plates at a density of 5×10^4 cells per well one day ahead and treated with PSCNPs for 48 hours. After incubation, supernatants were collected and centrifuged at 1000g for 10 min. Cellular release of high mobility group box 1 (HMGB1) was then tested by using Mouse HMG1 / HMGB1 (Sandwich ELISA) ELISA Kit (LSBio, LS-F23080) following the manufacturer's protocol.

Migration of BMDCs to dying cancer cells. The migration study was performed in the Transwell system (8.0 μm pore size, Corning, 3428). Briefly, 5×10^5 BBN963 cells were seeded into the lower chamber and cultured overnight for cell adherence. Cells were then treated with PSCNPs for 2 hours followed by seeding 1×10^6 CFSE-labeled BMDCs to the upper chamber and co-incubated for another 24 hours. All cells in the lower chamber were collected by cell lifters, stained with Ghost Dye Red 780 (Gred), and further fixed. Samples were read through flow cytometry, and $CFSE^+Gred^-$ BMDCs will be counted.

BMDCs maturation, activation, and antigen cross-presentation. 5×10^5 BBN963 cells were seeded into the 6-well plate and cultured overnight for cell adherence. Cells were treated with PSCNPs for 2 hours followed by the addition of 1×106 BMDCs and co-incubated for another 24 hours. Cells treated with PBS or LPS served as the negative and positive control respectively. After co-incubation, cells were collected and stained with DAPI, BV605-labeled anti-mouse CD86 (BD Biosciences, 563055), Alexa Fluor® 488 anti-mouse I-A/I-E (BioLegend, 107616), PerCP-Cy5.5-labeled anti-mouse CD80 (BD Biosciences, 560526), PE-labeled anti-mouse CD40 (Thermo Fisher Scientific, 5010351), PE-Cy7-labeled anti-mouse CD11c (BD Biosciences, 558079), APC-labeled anti-mouse CD205 (BioLegend, 138206). All samples were analyzed for the percentage of dye-positive signals within the $CD11c^+$ DCs population by flow cytometry.

Cytokines secretion from BMDCs. 5×10^5 BBN963 cells were seeded into the 6-well plate and cultured overnight for cell adherence. Cells were treated with PSCNPs for 2 hours followed by the addition of 1×10^6 BMDCs and co-incubated for another 24 hours. DCs alone and PBS-treated cancer cells were the negative control. Supernatants were collected and tested for pro-

inflammatory cytokines, including IL-12/23 p40, IL-1β, IL-6, TNF-α, and anti-inflammatory cytokine, IL-10 by ELISA kit (R&D Systems DY499, DY401, DY406, DY410, DY417, respectively).

***In vivo* cancer immunotherapy.** All animal studies were performed according to the Animal Use Protocol (AUP) approved by the Institutional Animal Care and Use Committee (IACUC) of the University of Georgia. 4-5 weeks-old female C57BL/6NHsd black mice were purchased from Envigo and maintained under pathogen-free conditions. BBN963 bladder tumor model was established by subcutaneously injecting 2×10^6 cells in 50 μL PBS into the right flank of the mice. When the tumor size reached 50-100 mm^3, PSCNPs (30 μL, 3.25 mg) were administered through direct intertumoral (i.t.) injections every other two days within one week for a total of 3 doses. For combination treatment, α-PD1 (10 mg/kg, Bio X Cell, BE0146) was intraperitoneal (i.p.) injected one day after the injection of PSCNPs. PBS at the same volume was injected for control. Degraded PSCNPs at the same concentration and α-PD1 alone were injected for comparison. After one week, 5 mice of each group were euthanized and the tumors, spleens, and lymph nodes of each mouse were collected for anti-tumor immunity analysis. Specifically, tumors were cut into small pieces with a scalpel blade and digested in the medium supplemented with collagenase V (1 mg/mL) and DNase I (50 U/mL) at 37 ℃. After 45 min, the solutions were gently pipetted and filtered through 250 μm cell strainers (Thermo Scientific, UB2685874A) to obtain the single-cell suspensions. Red blood cells in the mouse tumor samples were lysed with RBC Lysis buffer (eBioscience, 00-4333). After lysis, the Fc receptors of cells were blocked with anti-mouse CD16/32. As for spleens and lymph nodes, they were processed without the digestion and lysis steps, and minced and filtered with 70 μm cell strainers (Corning, 352235) to

obtain single-cell suspensions. All cells were then stained with various fluorophore-labeled antibodies of interest and analyzed by flow cytometry. DAPI, BV605-labeled anti-mouse CD86 (BD Biosciences, 563055), Alexa Fluor® 488 anti-mouse I-A/I-E (MHCII, BioLegend, 107616), PerCP-Cy5.5-labeled anti-mouse CD80 (BD Biosciences, 560526), PE-labeled anti-mouse CD40 (Thermo Fisher Scientific, 5010351), PE-Cy7-labeled anti-mouse CD11c (BD Biosciences, 558079) were exploited for DCs phenotyping. DAPI, BV510-labeled anti-mouse CD8a (BioLegend, 100752), BV605 anti-mouse CD4 (BD Life Sciences, 563151), Alexa Fluor® 488 anti-mouse CD3 (BioLegend, 100210), PerCP-Cy5.5-labeled anti-mouse CD25 (BioLegend, 102030), PE-labeled anti-mouse Foxp3 (BD Life Sciences, 563101), APC-labeled anti-mouse IFN-γ (BioLegend, 505810), APC-Cy7-labeled anti-mouse CD45 (BD Biosciences, 557659) were designed for T cells profiling. Note, for intracellular Foxp3 and IFN-γ staining, cells were permeabilized using a Permeabilization buffer (BD, 554714) before the antibody staining.

***In vivo* Therapy study.** All animal studies were performed according to the Animal Use Protocol (AUP) approved by the Institutional Animal Care and Use Committee (IACUC) of the University of Georgia. 0.5×10^6 MB49 bladder cancer cells in 50 μL PBS were subcutaneously injected into the right flank of the 4-5 weeks old female C57BL/6 mice to establish an MB49 bladder tumor model. When the tumor size reached 50-100 mm^3, initiated the treatments: (1) PBS; (2) degraded PSCNPs (30 μL, 3.25 mg); (3) PSCNPs (30 μL, 3.25 mg); (4) α-PD1 (10 mg/kg); (5) PSCNPs w/α-PD1; (6) PSCNPs w/α-CD4 (10 mg/kg); (7) PSCNPs w/α-DC8 (10 mg/kg). PSCNPs were i.t. injected 3 doses apart followed by α-PD1, α-CD4, or α-CD8. Tumor growth and body weight was monitored and recorded every 2 days. Tumor volumes were calculated as the [length × width2 /2]. The mice were euthanized when they reached the human

endpoint, either if the length or width > 1.7 cm or abnormal weight loss was observed. At the end of the therapy study, the tumors and major organs such as the heart, liver, spleen, lung, and kidney were collected and sent to a pathology lab for histological examination including H&E and Ki-67 staining. BBN963 tumor model was established by subcutaneously injecting 2×10^6 cells in 50 μL PBS. The same treatments were administered. Rechallenge study. The mice that survived from MB49 tumor model therapy study was inoculated with half of the amount of MB49 cells (0.25×10^6) on the opposite flanks. Monitored the tumor growth.

Statistical analysis: For *in vitro* study, all experiments were performed in triplicate. All data were represented as mean ± S.D. unless otherwise specified. For *in vivo* study, growth curves were represented as mean ± SEM. One-tailed student's t-test was used to determine the statistical significance between groups with p-value <0.05 considered significantly different. *, $p < 0.05$; **, $p < 0.01$; ***, $p < 0.001$; ****, $p < 0.0001$; ns, no significant difference.

Supporting figures

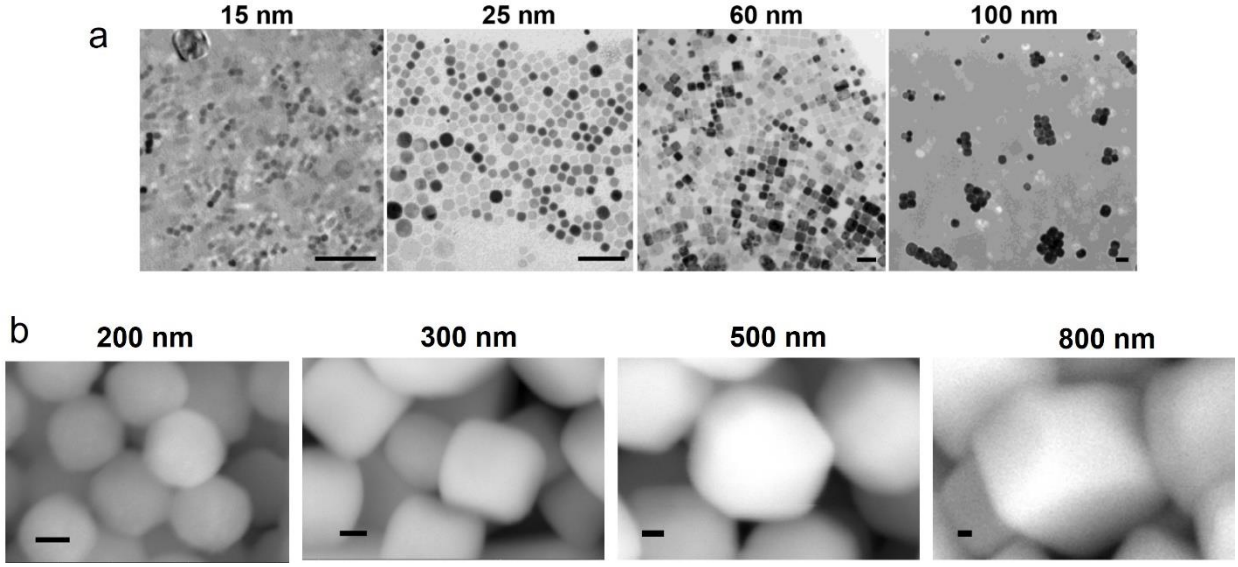

Figure S2.1. Representative a) TEM images and b) SEM images of SCNPs with different sizes. Scale bars, 100 nm.

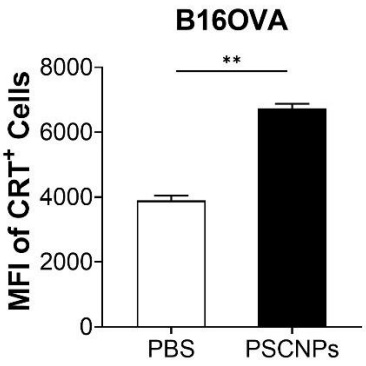

Figure S2.2. CRT expression on B16OVA cancer cells that were treated with PSCNPs for 24 h. MFI was analyzed by flow cytometry.

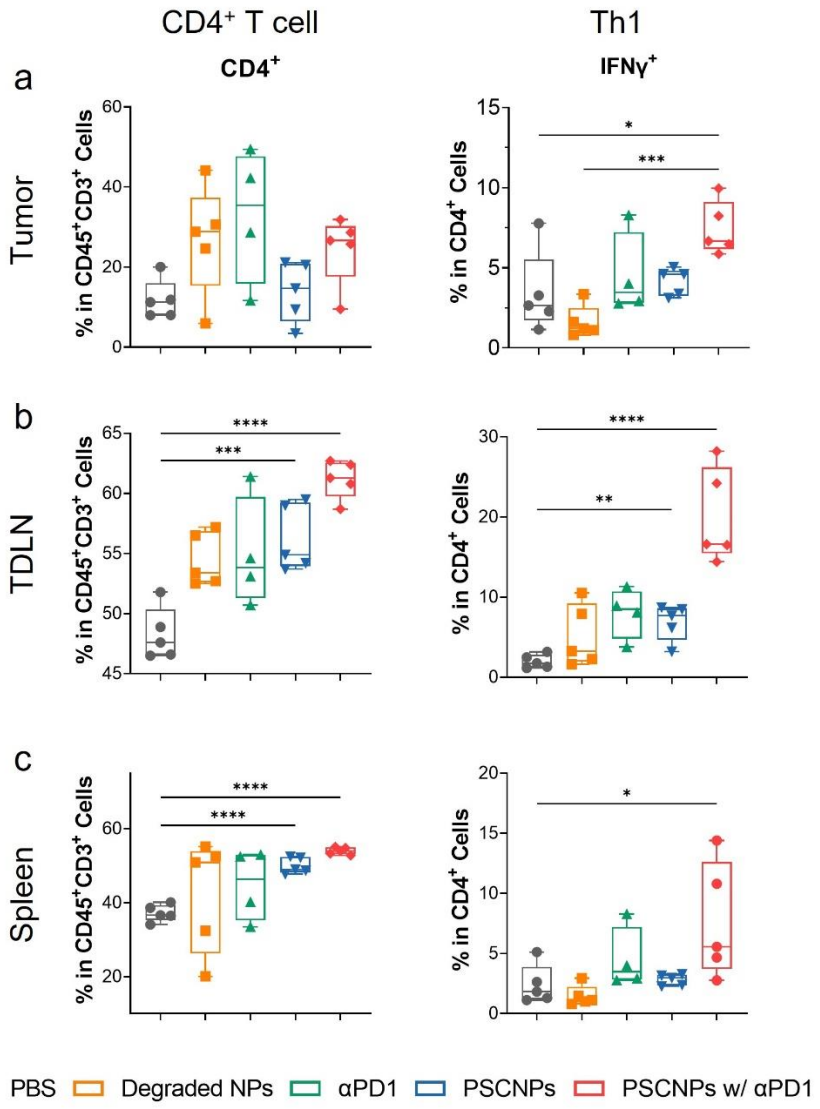

Figure S2.3. Impact of nanoparticles on TME. T-cell profiling related to Th1 cells in a) tumor, b) TDLN and c) spleen.

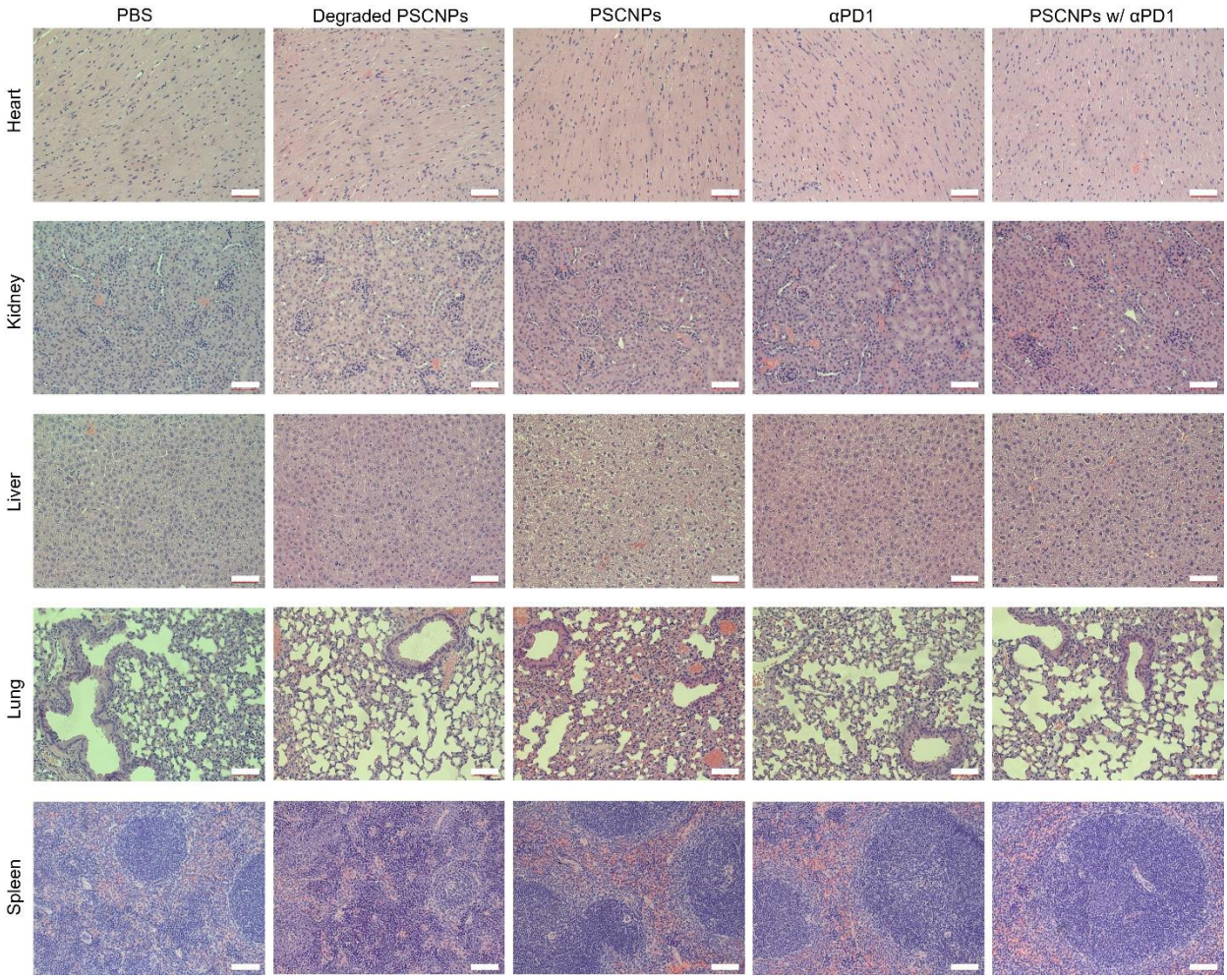

Figure S2.4. H&E staining of major organs.

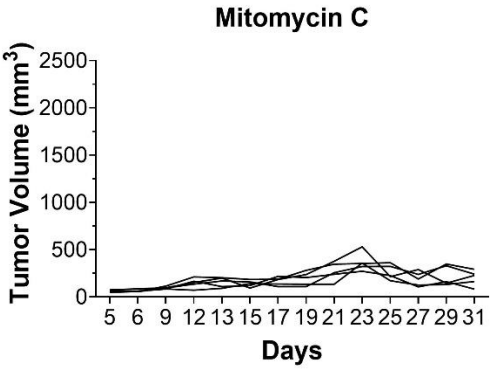

Figure S2.5. Individual tumor growth curve of Mitomycin C group.

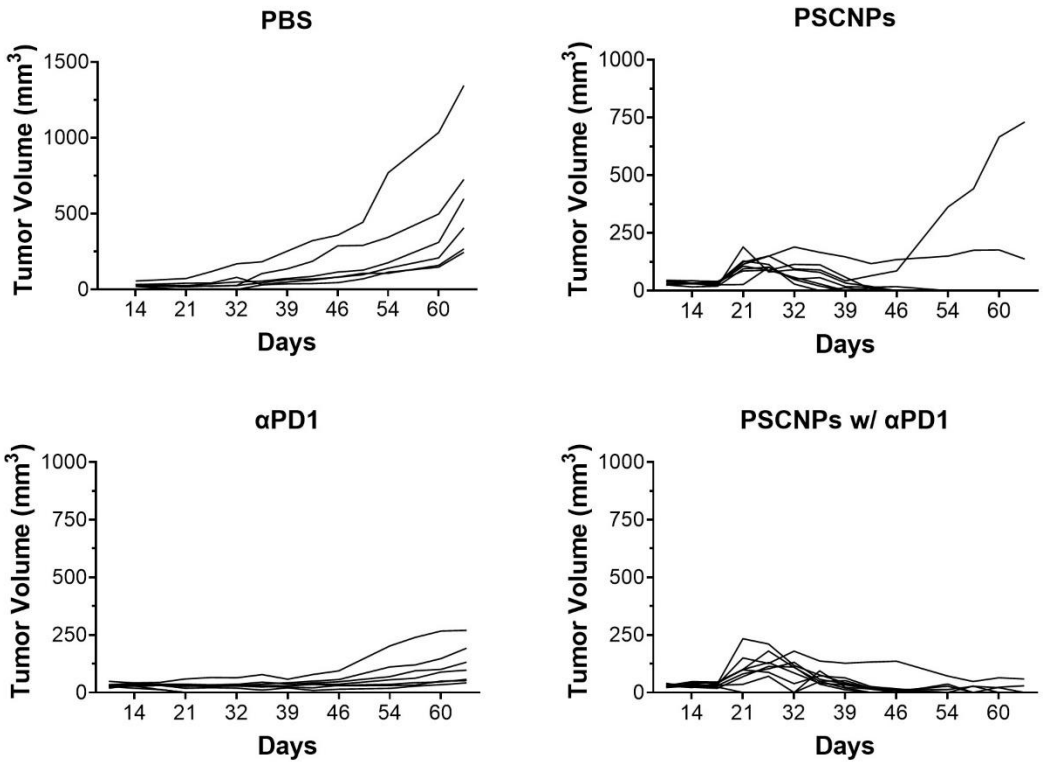

Figure S2.6. Individual tumor growth curve of BBN963 tumor model.

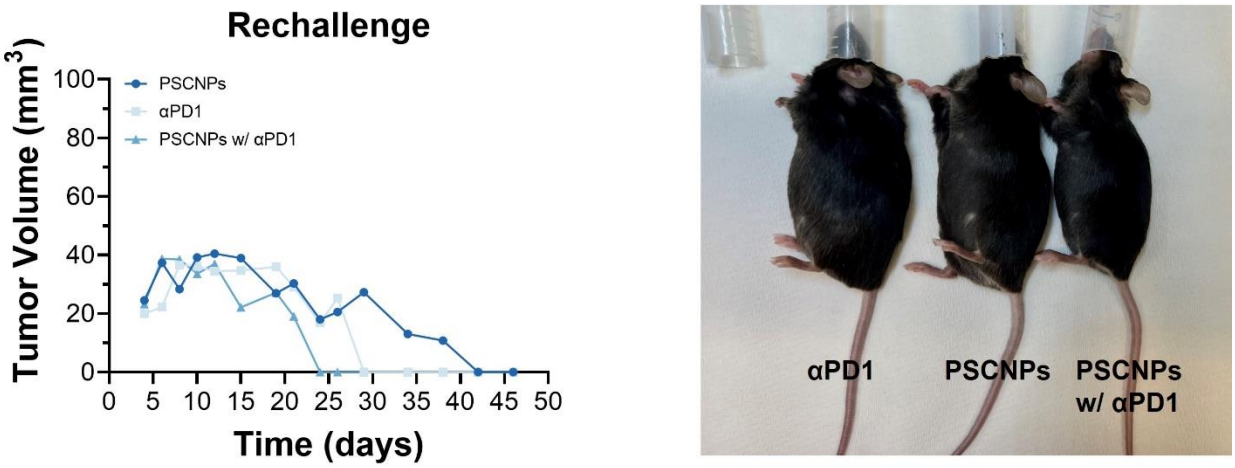

Figure S2.7. Rechallenge study. Three tumor-free mice were inoculated with 0.25M MB49 bladder cancer cells on the opposite flank. All groups refused tumor establishment.

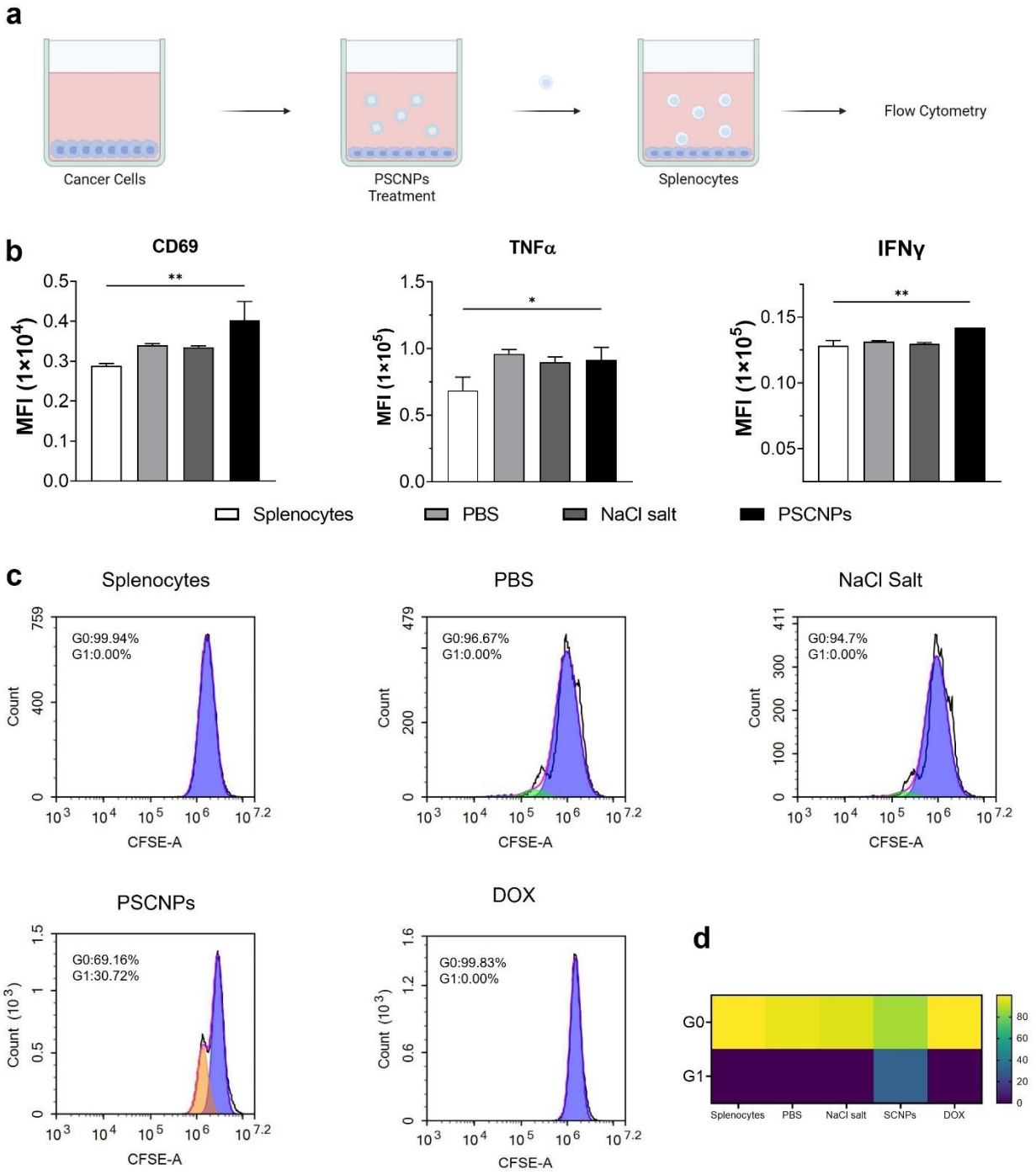

Figure S2.8. OT-1 activation and proliferation in vitro. a) Experiment design. Splenocytes extracted from a C57BL/6-Tg(TcraTcrb)1100Mjb/J (OT-1) mouse. Coincubation of splenocytes with PSCNPs treated cancer cells. b) T cell activation after 3 days of coincubation, MFI histogram of CD69, TNF-α, IFNγ. c) T cell proliferation after 5 days of coincubation.

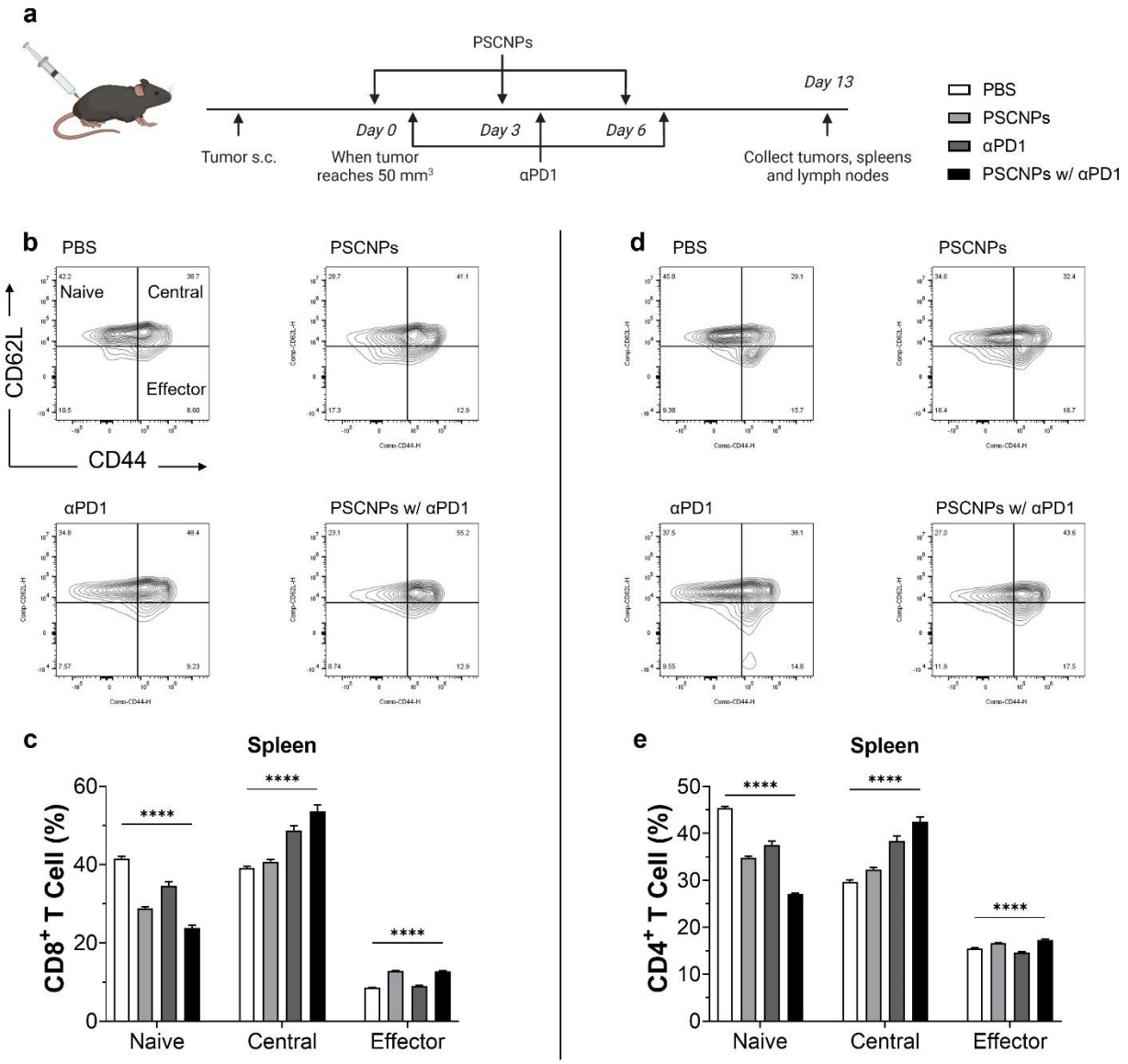

Figure S2.9. Memory T cells priming in spleen. a) Experiment design with treatment groups. b, d) Flow cytometry analysis. c) CD8+ T cells, e) CD4+ T cells, PSCNPs w/ αPD1 promoted the priming of OVA antigen-specific T cells and induced a shift in naïve T cells towards memory T cells.

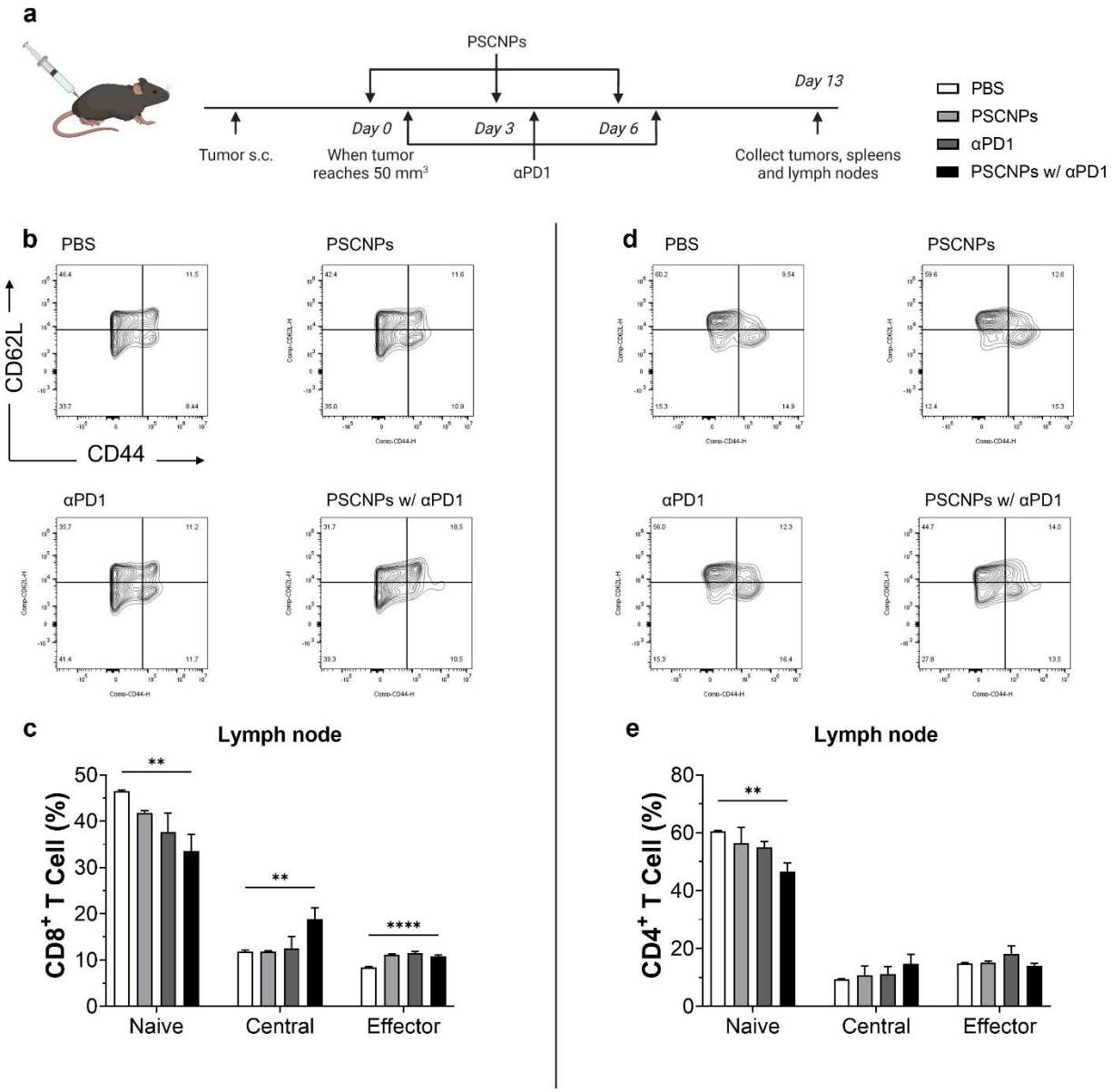

Figure S2.10. Memory T cells priming in lymph node. a) Experiment design with treatment groups. b, d) Flow cytometry analysis. c) CD8+ T cells, e) CD4+ T cells, PSCNPs w/ αPD1 promoted the priming of OVA antigen-specific T cells and induced a shift in naïve T cells towards memory T cells.

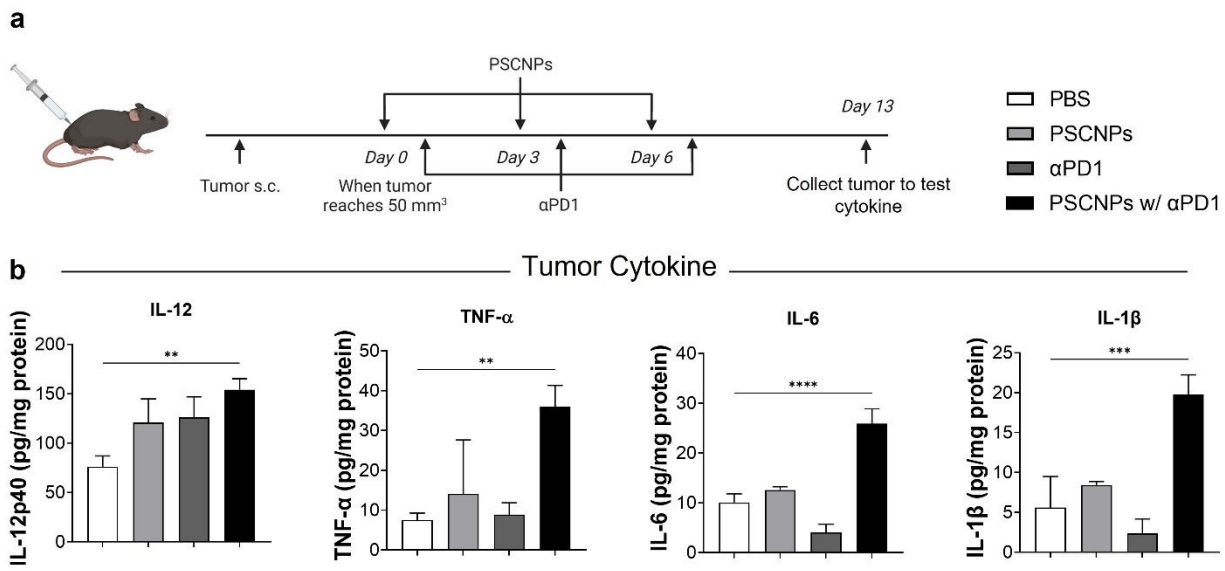

Figure S2.11. Cytokine in tumor. a) Experiment design with treatment groups. b) PSCNPs w/ αPD1 modulated the tumor microenvironment with increased pro-inflammatory cytokine level, including IL-12, TNF-α, IL-6, IL-1β.

	PBS	PSCNPs	αPD1	PSCNPs w/ αPD1	Ref.
WBC (10^3/μl)	12.0	10.6	8.2	8.0	0.8 – 10.6
Neu (10^3/μl)	3.91	4.56	2.42	1.42	0.23 – 3.60
Lym (10^3/μl)	7.18	6.29	5.19	6.19	0.60 – 8.90
Mon (10^3/μl)	0.63	0.4	0.23	0.18	0.04 – 1.40
Eos (10^3/μl)	0.19	0.17	0.34	0.23	0.00 – 0.51
Bas (10^3/μl)	0.01	0.02	0.01	0.01	0.00 – 0.12
Neu %	32.6	40.2	29.5	17.7	6.5 – 50.0
Lym %	60.6	54.7	63.4	77.0	40.0 – 92.0
Mon %	5.2	3.6	2.9	2.3	0.9 – 18.0
Eos %	1.6	1.5	4.0	2.8	0.0 – 7.5
Bas %	0.1	0.1	0.2	0.2	0.0 – 1.5
RBC (10^3/μl)	7.43	10.53	10.03	10.07	6.50 – 11.5
Hgb (g/dl)	12.2	16.4	15.7	15.6	11.0 – 16.5
Hct %	36.4	47.7	46.4	45.4	35.0 – 55.0
MCV (fl)	47.7	45.2	46.2	45.1	41.0 – 55.0
MCH (pg)	16.4	15.6	15.7	15.5	13.0 – 18.0
MCHC (g/dl)	34.5	34.4	33.9	34.4	30.0 – 36.0
RDW%	14.3	13.2	13.0	13.5	12.0 – 19.0
Platelet (10^3/μl)	641	1027	939	1008	400 – 1600
MPV (fl)	5.9	5.9	5.8	5.8	4.0 – 6.2

Figure S2.12. Toxicity of PSCNPs.

B Supporting information for Chapter 3

Synthesis of sodium chloride nanoparticles (SCNPs). Typically, at room temperature, 213 mg of sodium acetate (anhydrous, 99%, Sigma-Aldrich) was first completely dissolved in 65 mL of ethanol (PURE 200 PROOF, KOPTEC). 20 mL of oleylamine (70%, Sigma-Aldrich), which serves as a surfactant, and 10 mL of hexane (99.9%, Fisher) were then added to the mixture. Using magnetic stirring, 8 mL of hexane containing 160 μL of acetyl chloride (99.0%, Sigma-Aldrich) was added dropwise over 1.5 minutes using a 1 mL pipette. After the last drop, the SCNPs were immediately collected by centrifugation at 10000 rpm for 3 min and washed with 20 mL of isopropanol to remove unreacted precursors. Finally, the nanoparticles were redispersed in isopropanol, transferred to two glass vials, and dried by rotary evaporation (Buchi R II Rotavapor). The SCNPs were sealed with parafilm and carefully stored in a desiccator to avoid humidity.

DSPE-PEG (2000) folate-coated sodium chloride nanoparticles (SCNPs@folate). 10 mg as-synthesized nanoparticles were dispersed in 1.5 mL isopropanol and sonicated for two minutes, 0.45 mg phospholipid DSPE-PEG (2000) amine (1,2-distearoyl-sn-glycero-3-phosphoethanolamine-N-[amino(polyethylene glycol)-2000] (ammonium salt), Avanti) and 0.05 mg DSPE-PEG (2000) folate (1,2-distearoyl-sn-glycero-3-phosphoethanolamine-N-[folate(polyethylene glycol)-2000] (ammonium salt), Avanti) were added and the mixture was sonicated for another 30 s. The final product was dried by rotary evaporation. For rhodamine B-

labeled SCNPs@folate (RB-SCNPs@folate), 16:0 Liss Rhod PE (1,2-dipalmitoyl-sn-glycero-3-phosphoethanolamine-N-(lissamine-rhodamine B sulfonyl) (ammonium salt), Avanti) was added during sonication, and other steps remained the same.

Cell culture. SCC1-P (human head and neck squamous cell carcinoma), MOC1 (mouse oral cavity squamous cell carcinoma, less aggressive), and MOC2 (mouse oral cavity squamous cell carcinoma) were cultured in DMEM (ATCC, 30-2002) medium supplemented with 10% fetal bovine serum (FBS, Atlanta Biologicals, S11150) and 1% penicillin/streptomycin (Gibco, 1140-122). All cells were maintained in a 5% CO2, 37℃, humidified atmosphere (HERA cell 150, Thermo Scientific).

Cell uptake. SCC1-P or MOC1 cells were seeded in 6-well plates (Corning, 3516) at a density of 5×10^5 cells per well and incubated overnight. Four chemical endocytosis inhibitors, including sodium azide (50 mM, Sigma, S2002), Dynasore (80 μM, Abcam, ab120192), nystatin (25 μM, Sigma, N6261), and chlorpromazine (100 μM, Sigma, C8138), were added prior to NPs treatment to investigate the cell uptake pathway. After 1 hour, RB-SCNPs@folate were added for further incubation for 4 hours. Cells were harvested by cell lift, washed with PBS, stained with DAPI and fixed with IC fixation buffer (eBioscience, 00-8222-49)/staining buffer (eBioscience, 00-4222-57). Trypan blue solution (0.4%, GibcoTM) was added to quench fluorescence from cell surface membrane-bound nanoparticles at a final concentration of 20 μg/mL. Intercellular RB-SCNPs@folate signals were detected by flow cytometry (NovoCyte Quanteon Flow Cytometer Systems 4 Lasers) and analyzed for mean fluorescence intensity (MFI).

Ion homeostasis. SCC1-P cells were seeded into a 96-well black plate (Costar, 3610) at a density of 6000 cells per well and incubated overnight. Cells were loaded with 10 μM SBFI-AM (sodium binding benzofuran isophthalate acetoxymethyl ester, cell-permeant, Setareh Biotech, 6212), 10 mM MQAE (1-(ethoxycarbonylmethyl)-6-methoxyquinolinium bromide, cell-permeant, Setareh Biotech, 6270), or 10 μM Fluo-3 AM (Invitrogen™, F1241) in serum-free medium (serum may contain esterase activity) containing 0.02% Pluronic® F-127 (Sigma, P2443) for half an hour before the addition of SCNPs@folate. Intracellular Na^+, Cl^-, and Ca^{2+} fluorescence signals were recorded at different time points (0, 0.5, 1, 2, 4, 6 h) using a microplate reader (Synergy Mx, BioTeK). Ex339/Em565 for Na^+, Ex350/Em460 for Cl^-, Ex506/Em526 for Ca^{2+}. PBS and NaCl salt were used as controls.

Reactive oxygen species (ROS) are chemically reactive molecules containing oxygen. The most common ROS include superoxide ($•O_2^-$), hydrogen peroxide (H_2O_2), and hydroxyl radical (•OH).

DHE assay. Superoxide ($•O_2^-$) generation was detected using a dihydroethidium assay kit (DHE, Cayman chemical, 601290) according to the manufacturer protocol. Briefly, SCC1-P or MOC1 cells were seeded in a black 96-well plate (Costar, 3610) at a density of 6000 cells per well and incubated overnight. Treated the cells with SCNPs@folate for 4 hours. Aspirated off the culture medium and added 150 μL of cell-based assay buffer to each well, then aspirated off the 140 μL buffer and added 130 μL of ROS staining buffer, incubated at 37℃ for 30 min. Following the incubation, aspirated ROS staining buffer and added 100 μL of cell-based assay buffer. Fluorescent was measured at Ex500/Em590 using a fluorescent plate reader. Compared the fluorescent signals before and after 5 Gy irradiation.

APF assay. Peroxyl (ROO•) and hydroxyl radicals (•OH) generation was detected using aminophenyl fluorescein (APF, Invitrogen, A36003) according to the manufacturer protocol. Briefly, SCC1-P or MOC1 cells were seeded in a black 96-well plate (Costar, 3610) at a density of 6000 cells per well and incubated overnight. Treated the cells with SCNPs@folate for 4 hours. Aspirated off the culture medium and incubated the cells with APF at final concentration of 10 μM in PBS for 30 minutes at 37 ℃. After incubation, replaced with fresh PBS to remove excess probe. Fluorescent was measured at Ex490/Em515 using a fluorescent plate reader. Compared the fluorescent signals before and after 5 Gy irradiation.

Superoxide dismutase assay. Total superoxide dismutase (SOD) activity (cytosolic and mitochondrial) was detected using a SOD assay kit (Cayman chemical, 706002) according to the manufacturer protocol. Briefly, SCC1-P cells were seeded in a 6-well plate (Costar, 3516) at a density of 0.5 M per well and incubated overnight. The cells were treated with SCNPs@folate for 4 hours and then irradiated with 5 Gy radiation if IR applied. After another 1 h incubation, cells were collected with a cell lifer and washed with PBS. Redispersed the cells in 100 μL HEPES buffer and lysed the cells using probe sonication for 10s (1s on, 1s off, 30% amplitude) in an ice bath. Supernatants were collected by centrifugation (1500g, 5 mins) for assay. 10 μL samples or standards were added in a 96-well plate (Costar, 3599) followed by the addition of 200 μL of radical detector and 20 μL of Xanthine Oxidase. After 30 mins incubation at room temperature, the absorbance at 450 nm was measured using plate reader.

Glutathione assay. Glutathione (GSH) depletion was quantified using a GSH assay kit (Cayman chemical, 703002) according to the manufacturer protocol. Briefly, Briefly, SCC1-P cells were

seeded in a 6-well plate (Costar, 3516) at a density of 0.5 M per well and incubated overnight. The cells were treated with SCNPs@folate for 4 hours and then irradiated with 5 Gy radiation if IR was applied. After another 1 h incubation, cells were collected with cell lifer and washed with PBS. Redispersed the cells in 1 mL PBS and lysed the cells using probe sonication for 30s (10s on, 5s off, 30% amplitude) at ice bath. Supernatants were collected by centrifugation (1500g, 5 mins) for assay. 50 μL samples or standards were added in a 96-well plate (Costar, 3599) followed by the addition of 150 μL freshly prepared assay cocktail. After 25 mins incubation, read the absorbance at 410 nm using plate reader.

When ROS levels become too high, they can cause oxidative stress, leading to damage of cellular structures such as DNA, lipids, and proteins.

γH2AX assay. The DNA damage was measured using an anti-γH2AX antibody (Biolegend, Alexa 488, 613405). SCC1-P or MOC1 cells were seeded in a 4-well cell culture chamber slide at a density of 0.1 M per well and incubated overnight. Cells were treated with SCNPs@folate for 4 hours and irradiated with 5 Gy radiation if IR was needed. Then cells were washed with PBS, stained with anti-γH2AX antibody, and covered with DAPI mount medium. Images were acquired by an all-in-one fluorescence microscope (KEYENCE BZ-X810).

TBARS assay. Malondialdehyde (MDA), a naturally occurring product of lipid peroxidation was measured using a TBARS assay kit (Cayman chemical, 10009055) according to manufacture protocol. Briefly, SCC1-P cells were seeded in a 6-well plate (Costar, 3516) at a density of 0.5 M per well and incubated overnight. The cells were treated with SCNPs@folate for 4 hours and then irradiated with 5 Gy radiation if IR was applied. After another 1 h

incubation, cells were collected with a cell lifer and washed with PBS. Redispersed the cells in 1 mL PBS and lysed the cells using probe sonication for 30s (10s on, 5s off, 30% amplitude) in an ice bath. Supernatants were collected by centrifugation (1500g, 5 mins) for assay. 100 μL samples or standards were added to 5 mL tubes followed by the addition of 100 μL SDS solution and 4 mL color reagent. Boiled the tube at boiling water for one hour, then put the tubes on ice for 10 mins to stop the reaction. After 10 mins, tubes were centrifugated at 1600 g and 150 μL aliquots were transferred to a 96-well plate (Costar, 3599). Absorbance at 535 nm was recorded using a plate reader.

BODIPY lipid probe assay. BODIPY™ 581/591 undecanoic acid (Invitrogen, BODIPY™ 581/591 C11, D3861) can be used to detect ROS in lipid environments. Upon oxidation, the probe shifts the excitation and emission from 581/591 to 488/510 nm. Briefly, SCC1-P or MOC1 cells were seeded in a black 96-well plate (Costar, 3610) at a density of 6000 cells per well and incubated overnight. Cells were treated with SCNPs@folate for 4 hours and then irradiated with 5 Gy radiation if IR was needed. After another 1 h incubation, C11-BODIPY was added for a further 1 h incubation. Fluorescent at 488/510 was measured and compared to the control group.

Cytotoxicity study. MTT (3-(4,5-dimethylthiazol-2-yl)-2,5-diphenyl tetrazolium bromide, Sigma) assay was performed to test NPs cytotoxicity. SCC1-P or MOC1 cells were seeded in a 96-well transparent plate (Corning, 3599) at a density of 6000 cells per well and incubated overnight. Cells were treated with SCNPs@folate in an FBS-free medium for 4 hours and maintained in a complete medium for another 20 hours. MTT was introduced to form purple formazan crystals in viable cells. The absorbance of MTT in dimethyl sulfoxide (DMSO, 99%,

Thermo Scientific) solution was measured by a microplate reader at 570 nm (Synergy Mx, BioTeK).

LDH release. SCC1-P or MOC1 cells were seeded in a 96-well plate (Costar, 3599) at a density of 6000 cells per well and incubated overnight. The cells were further incubated with SCNPs@folate in an FBS-free medium for 4 hours and maintained in a complete medium for another 20 hours. LDH contents in the supernatant were measured by LDH Assay Kit-WST (Dojindo, CK12-20).

Clonogenic assay. SCC1-P cells were seeded in a 6-well plate (Costar, 3516) at a density of 0.5 M per well and incubated overnight. Cells were treated with SCNPs@folate for 4 hours followed by 5 Gy irradiation if needed and maintained for another 24 hours. Then, the cells were collected and counted, reseeded in a 6-well plate at a density of 100-500 cells per well, and cultured for 14 days. The colonies were stained with crystal violet and counted.

In vivo **Therapy study.** All animal studies were performed under the instructions of the Animal Use Protocol (AUP) approved by the Institutional Animal Care and Use Committee (IACUC) of the University of Georgia. 2×10^6 MOC1 cells in 50 μL PBS were subcutaneously injected into the right flank of the 4-5 weeks old female C57BL/6 mice to establish a head and neck tumor model. When the tumor size reached 50-100 mm^3, SCNPs@folate (3.25 mg) in 30 μL PBS was intratumorally (i.t.) injected every other two days for 3 doses in total. 5 Gy irradiation was applied after 4 hours of NPs treatment. Tumor growth and body weight was monitored and recorded every other day. Tumor volumes were calculated as the [length × width2 /2]. The mice

were euthanized when they reached the human endpoint, either if the length or width > 1.7 cm or abnormal weight loss was observed. At the end of the therapy study, the tumors and major organs such as the heart, liver, spleen, lung, and kidney were collected and sent to a pathology lab for histological examination including H&E and Ki-67 staining.

Statistical analysis: For *in vitro* study, all experiments were performed in triplicate. All data were represented as mean ± S.D. unless otherwise specified. For *in vivo* study, growth curves were represented as mean ± SEM. One-tailed student's t-test was used to determine the statistical significance between groups with p-value <0.05 considered significantly different. *, $p < 0.05$; **, $p < 0.01$; ***, $p < 0.001$; ****, $p < 0.0001$; ns, no significant difference.

Supporting figures

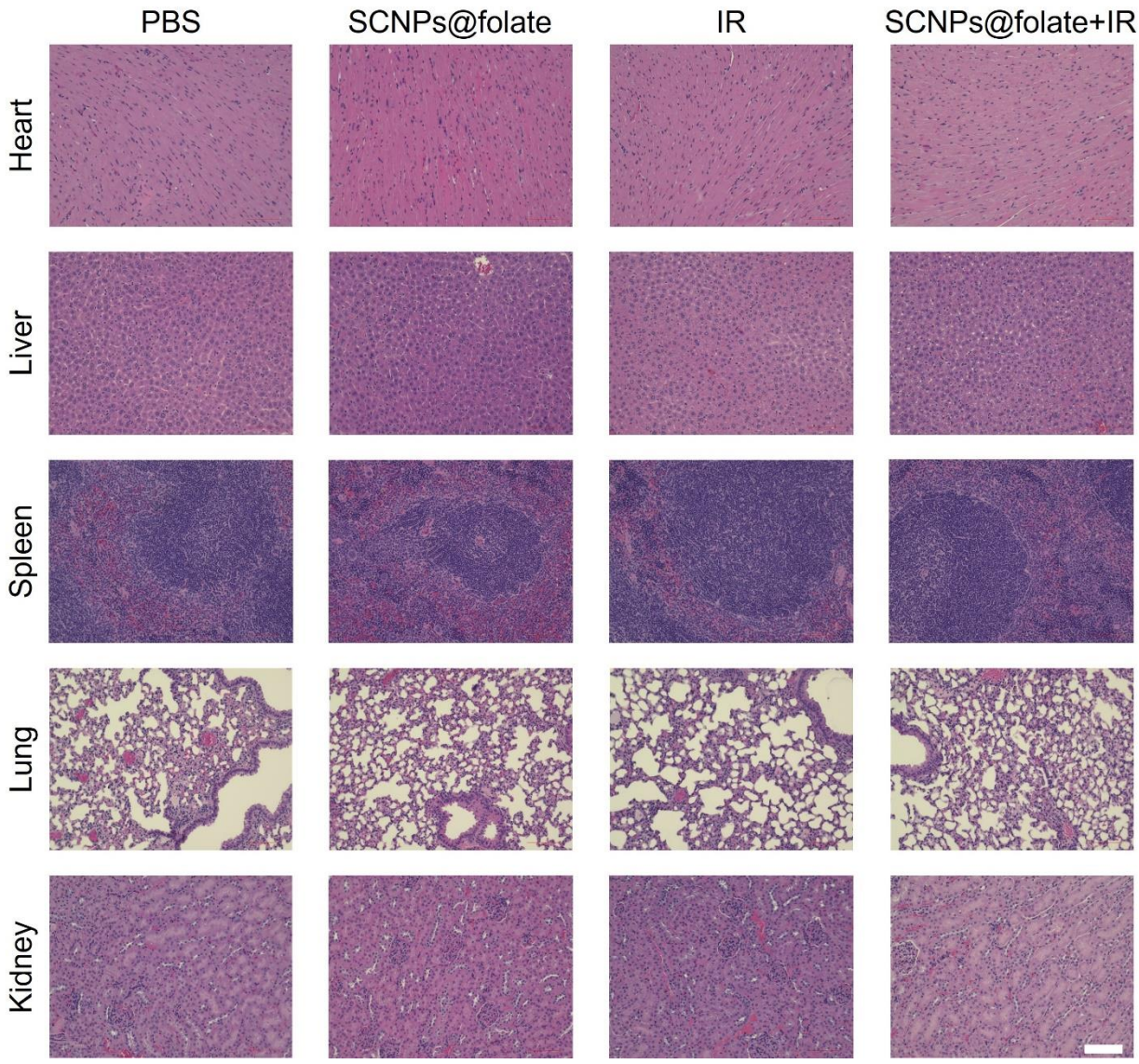

Figure S3.1. H&E staining of major organs.

C Supporting information for Chapter 4

Characterization of nanoparticles. The morphology, size distributions, and zeta potential of four commercially available nanoparticles: Fe_2O_3, iron oxide nanopowder (ION, 544884-Aldrich), Al_2O_3, aluminum oxide nanopowder (AON, 544833-Aldrich), ZnO, zinc oxide nanoparticles (ZON, 721077-Aldrich), multi-walled carbon nanotube (MWCNT, 659258-Aldrich), were characterized by transmission electron microscope (SEM, FEI Teneo), dynamic light scattering (DLS, Malvern Zetasizer Nano S90) and Zetasizer (Malvern Nano ZS).

Cell culture. Macrophages RAW264.7 and murine colorectal carcinoma cells CT26 were cultured in RPMI-1640 (Corning, 10-040-CV), melanoma cancer cells B16OVA expressing ovalbumin were grown in high glucose DMEM (ATCC, 30-2002). All culture media were supplemented with 10% fetal bovine serum and 1% penicillin/streptomycin. All cells were maintained at 37 ℃ with a humidified 5% CO_2 atmosphere.

Cytotoxicity of NPs on macrophages. RAW264.7 were seeded into 96-well plates overnight. After being treated with different NPs of series concentrations and co-incubation for 24 h, the cell viability was measured by 3-(4,5-dimethythiazon-2-yl)-2,5-diphenyl tetrazolium bromide (MTT) assay to determine the appropriate concentration range for the following test. Absorbance at 570 nm was read by a microplate reader (Synergy Mx, BioTeK).

Macrophage engineering. Macrophages were seeded in 100 mm Petri dishes overnight, then incubated with each NPs for 2 h within the safe concentration range, followed by medium replacement and another 24 h incubation to induce DAMPs secretion. NPs-laden macrophages were obtained.

ATP and HMGB-1 release. After 24 h incubation post 2 h NPs treatment, the cell supernatant was collected and measured by ATP 1step Luminescence Assay to quantify extracellular ATP. The luminescence was measured by a microplate reader. HMGB-1 secretion was quantified by Mouse HMG1 / HMGB1 Quant ELISA Kit (LS-F23080, LSBio) following the manufacturer's instructions.

CRT expression on macrophages. After 24 h incubation posts 2 h NPs treatment, the macrophages were collected with cell lifters and stained with Alexa Fluor 647-conjugated anti-CRT antibody (ab196159, Abcam). Surface CRT expression was then assessed by flow cytometry. The data were expressed and compared in mean fluorescence intensity (MFI). Macrophage phenotype characterization. M1-like markers (TNF-α, CD86, iNOS) and M2-like markers (CD206, IL-10) were assessed to characterize the phenotype change of macrophages. Specifically, after 2 h NPs treatment and a further 24 h incubation, macrophages were collected by cell lifters, stained with CD86, iNOS, and CD206 antibodies, then evaluated by flow cytometry. The signals of each group were presented in MFI compared to the control group. On the other hand, cell supernatants were collected at 24 h to quantify the concentrations of different cytokines, including TNF-α and IL-10 by enzyme-linked immunosorbent assay (ELISA).

Cytotoxicity of NP-laden MF on cancer cells. The cytotoxicity effect of MF or NP-laden MF on cancer cells was investigated through transwell plates. 4T1 breast cancer cells were seeded on the lower chamber of the plates overnight. On the following day, macrophages were treated with NPs for 2 h at first, then MF/eMFs were added to the upper chamber. The transwell membrane isolates cancer cells from direct contact with macrophages but enables soluble signal molecules secreted by macrophages to pass through. After 24 h co-incubation, cancer cell viability was assessed by MTT assay and the apoptosis or necrosis process of cancer cells was determined by Annexin V-FITC/PI assay through flow cytometry. H_2O_2-treatment of cancer cells could be served as a positive control.

CRT expression on cancer cells. To investigate whether MF-secreted CRT can bind to the surface of cancer cells, macrophages were treated with NPs and the supernatants were collected and used to incubate cancer cells. After 30 min, cancer cells were harvested to stain with anti-CRT antibody and evaluated by flow cytometry.

Migration and activation of bone marrow dendritic cells (BMDCs). Bone marrow dendritic cells were derived from bone marrow progenitor cells and prepared according to the previous papers. Transwell was adopted to study the migration and activation of BMDCs. Briefly, we first incubated RAW264.7 cells with either ION, ZON, or AON nanoparticles; we then collected the supernatant, and added it to the incubation medium of BMDCs. BMDCs were added to the upper chamber, while B16OVA cancer cells (irradiated or unirradiated) were seeded to the lower chamber of the transwell. After 24 h, cells in the lower chamber were collected and stained with

CD206, CD86, iNOS, and SIINEFKL. The positive population of each marker of DCs was analyzed by flow cytometry. Separately, CFSE-labeled DCs was analyzed for migration study.

***In vivo* immunotherapy study.** All animal studies were performed according to the guidelines from the University of Georgia Institutional Animal Care and Use Committee (IACUC). 20 female 4-week-old C57BL/5 mice were subcutaneously inoculated with 0.5 M B16OVA cells. After the tumor size reached 50 mm^3, the mice were randomly divided into four groups and given treatment as follows: (1) PBS, (2) RT (5 Gy), (3) RT/MF (4) RT/MF+ION. After 7 days, tumors and lymph nodes were collected, either digested or ground to make single-cell suspensions with cell strainers. Multiple antibodies were used to stain the cells to evaluate the activities of immune cells in the tumor microenvironment and tumor-draining lymph nodes. In a separate experiment, 2M splenocytes obtained from spleens of euthanized mice were co-incubated with 0.5M B16OVA cells in the presence of Golgi inhibitor. After 4 h, cells were collected, stained with CD8 and CD4, followed by fixation and permeabilization, further stained with IFN-γ. $CD8^+$, $CD4^+$ population of T cells and percentage of IFN-γ^+ among $CD8^+$ T cells were quantified by flow cytometry.

Therapy studies. CT26 colorectal carcinoma cells were subcutaneously inoculated on the right hind leg of Balb/c mice. Treatments started when tumor size reaches ~100 mm^3. 15 mice were randomly divided into 5 groups and were treated with Radiotherapy (RT) followed with i.t. injection of PBS, MF, MF+ION, MF+AON, MF+ZON. NP-laden macrophages were prepared and collected post 2 h incubation with NPs, ION-40 μg/mL, AON-80 μg/mL, ZON-5 μg/mL. Two separate treatments, ~250,000 cells in 100 μL PBS/mouse and ~500,000 cells in 100 μL

PBS/mouse were given 7 days apart. The tumor size and body weight were monitored every other day. The tumor volume was calculated by the following equation: tumor volume = length × (width)2 / 2, where length ≥ width. Mice were euthanized once the tumor volume was above 1,700 mm3.

In separate studies, murine B16OVA melanoma cancer cells (H2b) were subcutaneously inoculated on the right flank of C57BL/5 mice. Treatments started when tumor size reaches ~ 50 mm3. 20 mice were randomly divided into 4 groups and were i.t. injected with PBS, ION (0.1 mg), or applied RT (5 Gy) on tumor, RT followed with ION. Three treatments were given every other two days within one week. The tumor size and body weight were monitored every other day. Mice were euthanized once the tumor volume was above 1,700 mm3. All tumors and organs including heart, liver, spleen, lung, kidney were harvested for histopathology analysis, basically H&E and Ki-67 staining.

Statistical methods. Quantitative data were expressed as mean ± SEM. One-tailed Student's t-test test and One-way ANOVA were used for statistical comparison between experimental groups and control groups for different studies. GraphPad Prism 9 software (San Diego, CA) was used for data analysis. $P < 0.05$ was considered statistically significant.

Supporting figures.

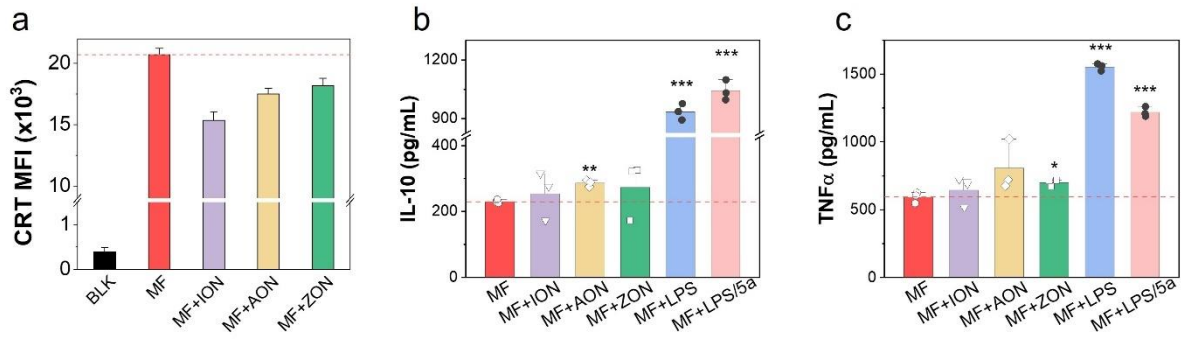

Figure S4.1. Impacts on macrophages post 2 h treatment of NPs. a) Expression of CRT. b) IL-10 release. c) TNF-α release.

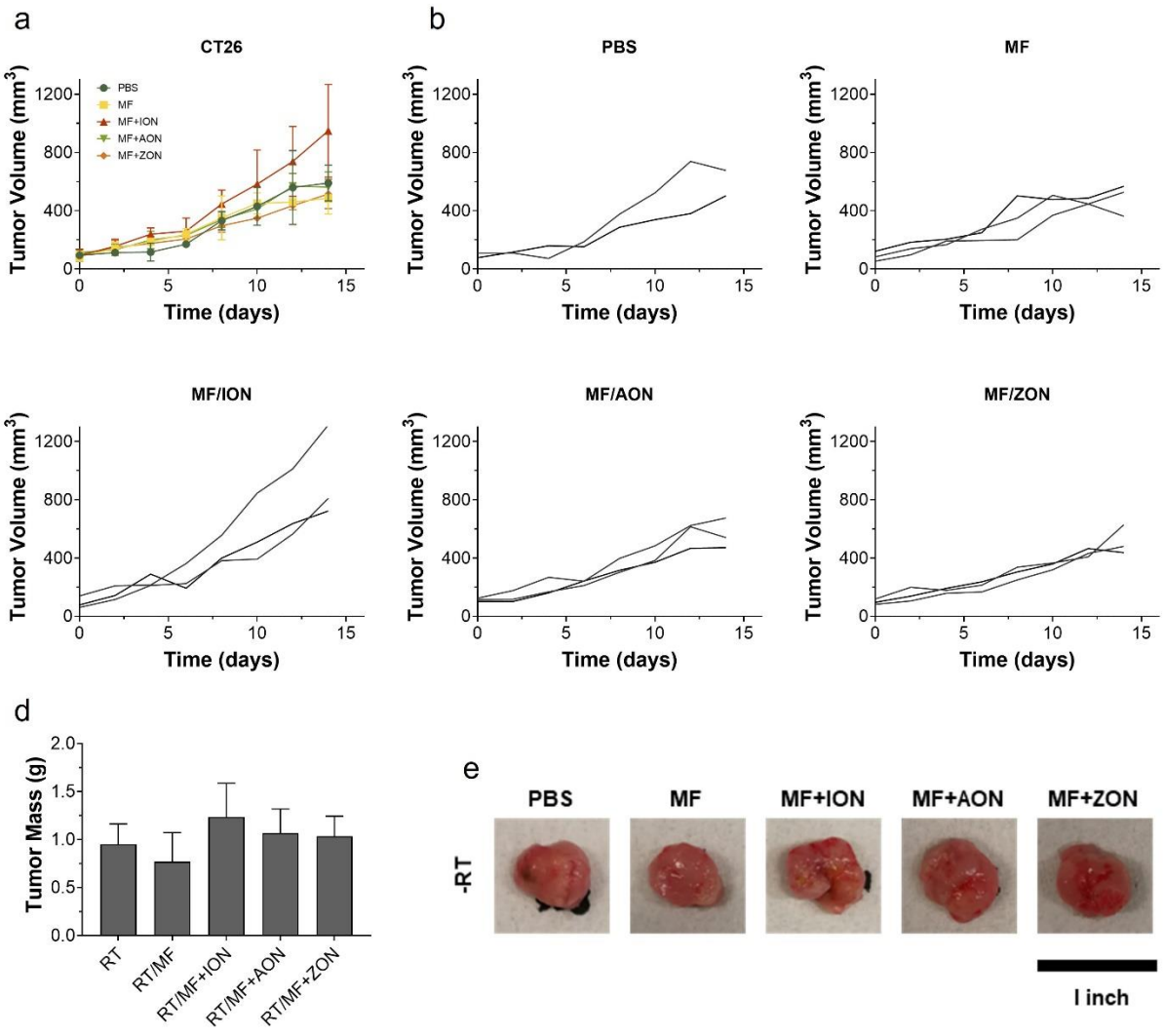

Figure S4.2. CT26 tumor model without RT. a) CT26 tumor growth curve. b) Individual tumor growth curve. d) Tumor mass. e) Representative images of tumors.